

Fakultät für Chemie – Lehrstuhl für Technische Chemie II

Name der promotionsführenden Einrichtung

Formation and Stabilization of Zeolite Frameworks

Titel der wissenschaftlichen Abhandlung

Sebastian Prodingler

Vorname und Name

Vollständiger Abdruck der von der promotionsführenden Einrichtung
der Fakultät für Chemie

der Technischen Universität München zur Erlangung des akademischen Grades
eines Doktors der Naturwissenschaften (Dr. rer. nat.)
genehmigten Dissertation.

Vorsitzende/-r: Univ.-Prof. Dr.-Ing. Kai-Olaf Hinrichsen

Prüfende/-r der Dissertation:

1. Univ.–Prof. Dr. Johannes A. Lercher

2. Prof. Dr. Mirosław A. Derewinski

Die Dissertation wurde am 11.05.2017 bei der Technischen Universität München
eingereicht und durch die promotionsführende Einrichtung
am 26.6.2017 angenommen.

Acknowledgements

First and foremost, I would like to express my sincere gratitude and appreciation to my advisor Professor Dr. Johannes A. Lercher. The guidance and patience you have had for me is immeasurable in value and I will always think kindly on the long and at times difficult discussions we have had. You gave me an opportunity to work at the Pacific Northwest National Laboratory (PNNL) and despite it not being in Seattle, I am incredibly lucky and appreciative to have been able to perform my doctoral research here.

In the same breath, I would also like to express my deep appreciation for my mentor Professor Dr. Mirosław A. Derewinski for showing me the ropes of zeolite science and sparking my interest in the world of scholarly research. Our endless, morning coffee discussions, at times about mundane subjects, will always be one of my most cherished memories during my time in the Pacific Northwest. You are one person I could always count on, whether it had to do with picking us up from an ill-planned boating trip or helping me out with my workload and making sure that I am involved in as many projects as possible. Your ability to allow me to learn from my own mistakes and put up with my stubbornness is greatly appreciated. I realize that I would not have managed to finish this piece of work without your and Johannes's guidance and patience and for that I am deeply grateful.

It goes without saying that there are many more people who have had their part in getting me to this point especially the people in our group at PNNL whose knowledge in the field of catalysis and characterization I highly value. Especially the help of Drs. Don Camaioni, Hui Shi, Aleksei Vjunov, John Fulton, Jianzhi Hu is appreciated. I'm also grateful to Drs. Radha Kishan Motkuri and Feng Gao for enabling me to extend my field of interest into CO₂ adsorption and exhaust gas treatment respectively.

I am also incredibly grateful to Dr. Wendy Shaw, who was my manager for most of my time at PNNL, as well as the PNNL administrative staff who all did their best to help me out when I spent an extended stay at TUM. My unexpected stay at TUM also allowed me to get to know the rest of Johannes's group and I think kindly on the times Peter Hintermeier, Matthias Steib, Ferdinand Vogelgsang, Felix Kirchberger accepted me into their office as the 'Bürobazille'.

A large part of my gratitude also goes to the friends I've made here at PNNL, which is such a short-lived place with many changing faces. I would like to point out Drs.

Acknowledgements

Marton Kollar and Zbynek Novotny for the priceless times we spent together, camping and adventuring, which often entailed lots of beers and sausages.

Finally, I would like to thank my partner Tara for her patience with me and helping me get to where and who I am today. My family also deserves thanks for their endless support during the course of my studies, which cannot have been easy being so far away from home.

Sebastian Prodingner

Richland, May 2017

Abstract

The hydrothermal formation and decomposition of zeolite frameworks have been explored, using advanced physicochemical methods to characterize elementary steps. For synthesis, the Na^+ induced speciation of silica entities was shown to critically determine crystal structure and morphology by directing Si-O-Si bond formation. The reverse reaction in aqueous phase starts by breaking Si-O-Si bonds with the help of water associated with hydronium ions. Broken Si-O bonds are the sites at which the dissolution of the framework begins. Reducing the concentration of defects and hydronium ions stabilizes zeolite lattices.

Kurzzusammenfassung

Die elementaren Schritte der hydrothermalen Bildung und Zerstörung von Zeolithgittern wurden mittels moderner physikalisch-chemischer Methoden beschrieben. Es konnte gezeigt werden, dass die Orientierung der Kieselsäure Einheiten induziert durch Na^+ , während der Synthese entscheidenden Einfluss auf die Ausbildung der Kristallstruktur und Morphologie nimmt. Die Umkehrreaktion in der wässrigen Phase beginnt mit der Spaltung der Si-O-Si Bindungen bedingt durch die Gegenwart von Wasser, das mit Hydronium Ionen assoziiert ist. Die Auflösung des Gerüstgitters beginnt an defekten Si-O Bindungen. Das Zeolithgitter kann durch die Reduzierung der Defekte und Hydronium Ionen Konzentration stabilisiert werden.

Table of Content

ACKNOWLEDGEMENTS	I
ABSTRACT	III
TABLE OF CONTENT	IV
CHAPTER 1	1
INTRODUCTION	1
1.1 A BRIEF HISTORY OF ZEOLITES	2
1.2 INDUSTRIAL APPLICATIONS AND MARKETS FOR ZEOLITES	3
1.3 HYDROTHERMAL SYNTHESIS	6
1.4 THE NATURE OF ZEOLITES	9
1.5 ACID-CATALYZED DEHYDRATION ON ZEOLITES	11
1.6 HYDROTHERMAL STABILITY	13
1.6.1 STABILITY IN THE GAS-PHASE	13
1.6.2 STABILITY IN THE CONDENSED PHASE	14
1.7 SCOPE OF THIS THESIS	16
REFERENCES	19
CHAPTER 2	24
FORMATION OF FAUJASITE FOLLOWED BY <i>IN SITU</i> SPECTROSCOPY	24
INTRODUCTION	25
EXPERIMENTAL PROCEDURE	27
SYNTHESIS PROCEDURE	27
CLASSICAL SYNTHESIS	27
FAUJASITE SYNTHESIS FOLLOWED <i>IN SITU</i> VIA AL K-EDGE XAFS	27
<i>IN SITU</i> SYNTHESIS – NMR	28
<i>EX SITU</i> CHARACTERIZATION	29
RESULTS & DISCUSSION	31
<i>EX SITU</i> XRD	31
<i>IN SITU</i> AL XAFS ANALYSIS	32
<i>IN SITU</i> ²⁷ AL MAS NMR	34
<i>IN SITU</i> ²³ NA MAS NMR	38
ZEOLITE FORMATION	44
CONCLUSION	48
ACKNOWLEDGMENT	49
APPENDIX	50
X-RAY DIFFRACTION	50
HE ION MICROSCOPY	52
X-RAY ABSORPTION FINE STRUCTURE (XAFS)	53
NUCLEAR MAGNETIC RESONANCE	54
<i>IN SITU</i> ²⁷ AL MAS NMR	54
<i>EX SITU</i> CHARACTERIZATION	56

Table of Content

<i>IN SITU</i> ²³ Na MAS NMR	57
<i>EX SITU</i> CHARACTERIZATION	60
SPINNING SIDE BANDS	62
ABBREVIATIONS	65
REFERENCES	65
CHAPTER 3	68
IMPROVING STABILITY OF ZEOLITES IN AQUEOUS PHASE VIA SELECTIVE REMOVAL OF STRUCTURAL DEFECTS	68
INTRODUCTION	69
EXPERIMENTAL SECTION	70
SAMPLE PREPARATION	70
CHARACTERIZATION METHODS	71
RESULTS AND DISCUSSION	73
MODEL SYSTEM	73
STRATEGIES TO REMOVE STRUCTURAL DEFECTS VIA Si-REINCORPORATION	75
IMPACT OF SILANE	76
INCREASING TIME ON STREAM	77
INCREASING RESIDENCE TIME	78
METHOD REPRODUCIBILITY	78
HYDROTHERMAL STABILITY OF MODIFIED ZEOLITES	79
CONCLUSIONS	86
ACKNOWLEDGMENT	87
APPENDIX	88
SILYLATION PARAMETERS	88
HELIUM ION MICROSCOPY	89
THERMOGRAVIMETRIC ANALYSIS	90
INFRARED SPECTROSCOPY	91
N ₂ -PHYSISORPTION	92
X-RAY DIFFRACTION	95
²⁹ Si-CP-MAS NMR	96
TRANSMISSION ELECTRON MICROSCOPY	98
REFERENCES	99
CHAPTER 4	102
STABILITY OF ZEOLITES IN AQUEOUS PHASE REACTIONS	102
INTRODUCTION	103
EXPERIMENTAL SECTION	105
RESULTS AND DISCUSSION	110
CHARACTERIZATION OF PARENT AL-BEA	110
CHARACTERIZATION OF SILYLATED AL-BEA	113
STABILITY OF ZEOLITES IN PURE WATER	115
STABILITY OF ZEOLITES DURING CATALYSIS	116
CONCLUSION	122
ACKNOWLEDGMENT	123
APPENDIX	124

Table of Content

X-RAY DIFFRACTION	124
N ₂ PHYSISORPTION	126
HELIUM ION MICROSCOPY	130
²⁷ AL MAS NMR AND PY-IR QUANTIFICATION	132
CATALYSIS – CONVERSION PLOTS	134
APPENDIX NOTE 1 – ZEOLITE DEGRADATION	137
DISSOLUTION RATE IN PURE HOT LIQUID WATER	137
DEACTIVATION DURING CATALYSIS	137
CARBON BALANCE	137
DISSOLUTION OF THE CATALYST	137
APPENDIX NOTE 2 – LIQUID PHASE ADSORPTION	140
APPENDIX NOTE 3 – DETERMINING THE ROLE OF DEFECTS	143
REFERENCES	146
<u>CHAPTER 5</u>	<u>149</u>
<u>SUMMARY AND CONCLUSION</u>	<u>149</u>
<u>CURRICULUM VITAE</u>	<u>153</u>
<u>PUBLICATIONS</u>	<u>154</u>
<u>CONFERENCE PRESENTATIONS</u>	<u>155</u>

Chapter 1

Introduction

A zeolite is a crystalline aluminosilicate with a three-dimensional network of uniform, molecular sized pores. Based on the connectivity of the pores and the resulting three-dimensional network, different framework types can be differentiated, such as those shown in Figure 1.¹⁻²

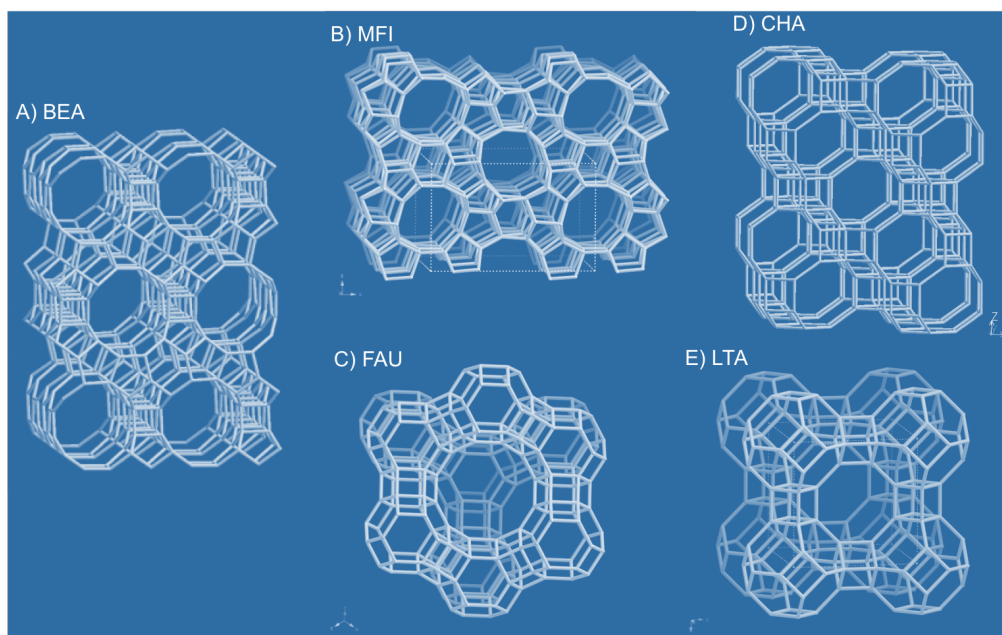


Figure 1. A select number of zeolite framework types chosen based on their importance in this thesis as well as in industrial applications and historical context. A – BEA, B – MFI (e.g. ZSM-5), C – FAU (Zeolite X and Y), D – CHA (see also SSZ-13), E – LTA (Zeolite A). Adapted from Baerlocher, C.; McCusker, L. B. Database of Zeolite Structures. <http://www.iza-structure.org/databases/>

Amongst the displayed framework types, denoted by their three-letter code,² special focus is given to BEA and FAU structures as the main zeolite structures under investigation in this thesis. This chapter is focused first on introducing the history and classical application area of zeolites followed by a general overview of the hydrothermal zeolite formation process and the resulting chemical and physical properties of zeolites. As an example of a zeolite-catalyzed chemical reaction, the dehydration reaction on zeolites is described in detail. Finally, a short overview of the

hydrothermal stability of zeolites is given, relevant to the set goal of finding ways to stabilize and improve zeolite hydrothermal stability in aqueous phase.

1.1 A brief history of zeolites

The word zeolite originates in the Greek combining ‘zeo’ and ‘lithos’ meaning ‘to boil’ and ‘stone’ respectively, and can be traced back to the discovery of the mineral stilbite by Axel Frederik Cronstedt in 1756.³ The term was coined when the hydrated aluminosilicate was exposed to a blowtorch and exhibited swelling. It wasn’t until 1862 when Sainte-Claire Deville first reported the successful man-made synthesis of levynite.⁴ The porous nature of this newly discovered mineral wasn’t clear until the early 20th century when first Friedel⁵ proposed a porous sponge-like network followed by the description of the molecular sieving process in zeolites, in this case chabazite⁶, in preferentially adsorbing molecules while leaving others behind. While the structural and molecular sieve properties of these naturally occurring minerals had been described quite well, the lab-made synthesis and discovery of new synthetic zeolites was hampered by reproducibility issues and incomplete characterization.⁷ Thus the history of synthetic zeolites, so widely used in today’s technological and industrial applications, did not take off until the mid 1930s when Richard Barrer started investigating the sorption behavior and synthesis of zeolites. His work on the transformation of mineral phases under action of strong salt solutions at temperatures above 150 °C led to the discovery of the first synthetic zeolite P and Q which were later shown to be part of the KFI framework⁸⁻¹⁰. Inspired by his work, Robert Milton at the Linde division of Union Carbide then used precipitated aluminosilicate gels as starting point for the hydrothermal synthesis, reducing the harsh conditions employed by Barrer and discovered zeolites A, B (now known as Na-P), C (hydroxy-sodalite) as well as X and synthetic chabazite (CHA) by the end of 1950.¹¹

Whereas it took roughly 200 years to come from the discovery of stilbite to the first successful synthesis of man-made zeolites by Barrer and Milton, the following growth in zeolite chemistry was astonishing. Initiated by Barrer’s and Denny’s visionary use of quaternary ammonium cations,¹² organic templating molecules eventually led to the discovery of the first high-silica zeolites, zeolite beta (BEA)¹³ by Wadlinger in 1967 followed by ZSM-5 (MFI)¹⁴, patented in 1972 by the Mobil corporation. Natural

zeolites as well as zeolites first discovered by Barrer and Milton (A, B, C and X) typically have very low Si/Al ratios, highlighting the accomplishment of discovering these high-silica counterparts. This then led to an increased number of discoveries and patenting of novel zeolitic material in the 1970s, followed by the successful generation of zeolite-like materials containing atoms other than the typically used Si and Al, such as the alumino-(AlPO) and gallophosphates (GaPO) in the 1980s.¹⁵ Up until this point, no zeolites with pore apertures consisting of more than 12-T atoms was obtained, which prevented the adsorption of molecules larger than 7.4 Å (i.e. diameter of a 12-membered ring in FAU). However, the incorporation of elements other than Al and Si led to more flexible bond angles and lengths eventually leading to the discovery of >12-T ring zeolite structures (e.g. P-substituted VPI-5¹⁶⁻¹⁷ and Ga-substituted CLO¹⁸). The 1990s then saw the discovery of amorphous mesoporous materials, typically synthesized in the presence of surfactants, such as MCM-41¹⁹⁻²⁰ and SBA-15²¹. Starting in the 1990s and gaining increasing popularity, the synthesis of hybrid materials such as metal organic frameworks (MOFs) was reported.²² The new millennium also saw the development and use of new technologies for the synthesis of zeolites highlighting this age of high technology. This involves themes such as charge-density mismatch²³, microwave heating, nano-sized zeolites²⁴, zeolite membranes and thin-films²⁵ as well as germanosilicates²⁶. In the last few years, a new concept – Assembly-Disassembly-Organization-Reassembly (ADOR) – was developed by the Morris and Cejka groups, for the first time allowing the top-down synthesis of zeolites with a controlled pore size.²⁷

Research interest in zeolites has been unabated over the last 70-80 years mainly due to the pioneering work of Barrer and Milton establishing the basics of zeolite synthesis in reasonable time-spans as well as the fast commercialization of synthetic zeolites owing to the large interest of industry. Some of the technologies employing zeolites will be discussed briefly in the next part.

1.2 Industrial applications and markets for zeolites

After the initial success by Barrer and Milton, Union Carbide was amongst the first to commercialize zeolites as efficient adsorbents for the separation and purification of

gases.⁷ Nowadays the market for zeolites can be split into several application fields, shown in Figure 2.

Annual Zeolite Consumption by Volume

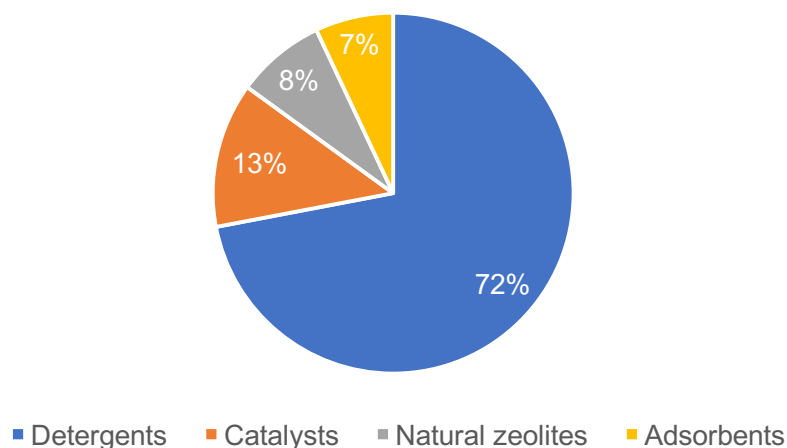


Figure 2. Annual consumption of zeolites by volume in 2005 (1.8 million metric tons), excluding China's use of natural zeolites (> 2.4 million tons), mainly as cement additives.²⁸

The largest market share of zeolites has consistently been made up of additives in detergents where their superior ion-exchange capacities and environmentally harmless nature come to play. Especially LTA with a Si/Al = 1 is the preferred zeolite for detergent applications. It represents the maximum number of Al that can be incorporated into a zeolite without violating the Lowenstein rule²⁹ that forbids the formation of Al-O-Al bonds. Consequently, it allows for the maximum density of exchangeable cations in these synthetic zeolites capable of replacing the hard calcium and magnesium cations in water with soft sodium cations from the zeolite. This prevents the precipitation of surfactant salts leading to a soiled or unclean load.³⁰ A large concentration of cations is also beneficial for the implementation of zeolites in adsorption processes increasing the adsorbate-adsorbent interactions for polar molecules.

Natural zeolites have been primarily used as additives in cement (China and Cuba).²⁸ In the rest of the world application of natural zeolites accounts only for a minor fraction, reserved mostly to wastewater treatment and removal of harmful NH_4^+ cations.³¹ They are also applied to odor control, nutrient release, pet litter or soil conditioner.²⁸

Despite taking up only 13-18% of the market by volume, the use of zeolites as catalysts has the highest market value. The majority of the catalysis market (>95%) is reserved for the use of inexpensive zeolite Y (FAU) in fluid catalytic cracking (FCC).³⁰ The FCC process is considered as one of the most important processes in oil refining, enabling the production of primarily gasoline and high-value olefins from the high-molecular weight fraction of crude oil (heavy gas oil – HVGGO). The process is described briefly. The main components of the FCC process are the riser and regenerator. The pre-heated feedstock is first injected into the riser at high temperatures where it encounters the powdered zeolite catalysts with the long-chain alkane molecules being cracked into shorter chains and olefins within a few seconds. The fluidized bed is then directed into the stripper where the deactivated, coked catalyst is separated into the regenerator and the product gas is further distilled. The spent catalyst is regenerated by burning off the coke, and the hot catalyst is reinserted into the riser where the heat from the regeneration process is used for the endothermic cracking reaction in the riser. Thus, large amounts of catalysts are continuously circulating between riser and regenerator justifying the large demand for this process. To withstand the high temperatures of the FCC process the Al-rich zeolite Y (FAU) needs to be stabilized by dealumination which generates a siliceous framework with separated acid sites of maximum strength³² (Ultra-stable zeolite Y – USY). Additionally, MFI additives are sometimes used to tailor the yield and selectivity of certain products in the cracking tower.

The remaining catalyst market for zeolites is attributed to their application in hydrocracking as well as organic syntheses where the choice of zeolite depends primarily on its compatibility with the organic reactions with the focus shifting from high conversions to high selectivities.³³ This is the main driving force in continued zeolite synthesis research.

It is important to note that out of the currently known 232 zeolite framework types less than 10% of them are of industrial interest. In the coming years, the number of newly discovered zeolites will increase, aided by post-synthetic modifications, however from a historical context, the number of discovered zeolites to be implemented in industrial processes is likely to be small.⁷ The number of applications for zeolites, however, will increase, also reflected by the steadily growing market.²⁸ This is driven by an increase in Asia for detergent and cat-cracking as well as increasingly tightened environmental

restrictions leading to the application of environmentally friendly zeolites in applications such VOC adsorption and exhaust gas treatments.⁷

1.3 Hydrothermal synthesis

The following chapter gives a general overview on the steps involved in zeolite synthesis. For a more detailed analysis of zeolite formation mechanisms the reader is referred to the extensive review by Cundy and Cox.³⁴

In order to obtain a synthetic zeolite, hydrothermal conditions must be employed in most cases. The synthesis typically occurs in an autoclave containing amorphous silica and alumina reactants along with a cation source in a highly basic aqueous medium. These are the starting ingredients for a successful synthesis. The aqueous solution is then heated beyond the boiling point of water (hydrothermal conditions) and after a certain induction period the initially amorphous aluminosilicate gel is transformed into a crystalline product. Classically, this crystallization process can be described with a S-curve, with a rapid growth period eventually slowing down as nutrients are consumed. Crystallization or zeolitisation is defined by kinetic control, as the breaking of bonds in the alumina and silica oxide precursors and formation of Si-O-Al bonds is enthalpically similar.³⁵ Zeolites are metastable species that convert to a more dense and stable phase such as cristobalite or quartz over time. It was shown that in comparison to quartz, zeolites are destabilized by only 6-14 kJ/mol and very similar to amorphous silica (0-7 kJ/mol).³⁶⁻³⁷ As a consequence zeolite synthesis is very sensitive to the gel composition, temperature and time. Precise control of these parameters is paramount to obtaining zeolites of high purity.

Gel Aging. Inherent to all zeolite formation mechanisms are several steps shown in Figure 2. It starts with the mixing of the reactants (e.g. SiO₂, Al(OH)₃, NaOH, H₂O) and subsequent formation of a dense hydrogel, also known as the primary amorphous phase (see (a) in Figure 3). The gel is then aged at room temperature during which the mineralizer anions (OH⁻) depolymerize the silica particles thus increasing their concentration in the liquid part of the gel. With time these monomeric silica species come into equilibrium with negatively charged oligomers (different from the initial polymerized SiO₂), catalyzed by the mineralizer ions. At this stage, the tetrahedrally coordinated aluminate anions (Al(OH)₄⁻) condense with silicate anions, preferentially

with the largest dissolved silicate species owing to their higher nucleophilicity (increasing degree of connectivity in the oligomers corresponds to increasing nucleophilicity). This condensation reaction also leads to an effective charge separation as the distributed negative charge on large silicate anions is small. The aluminosilicate precursor species formed during this aging period tend to arrange themselves into aluminosilicate polyanions also known as secondary building units (SBUs), e.g. 4, 6-membered rings, representing a more ordered, secondary amorphous phase (see (b) in Figure 3). The cations present under these conditions play a structure directing role.

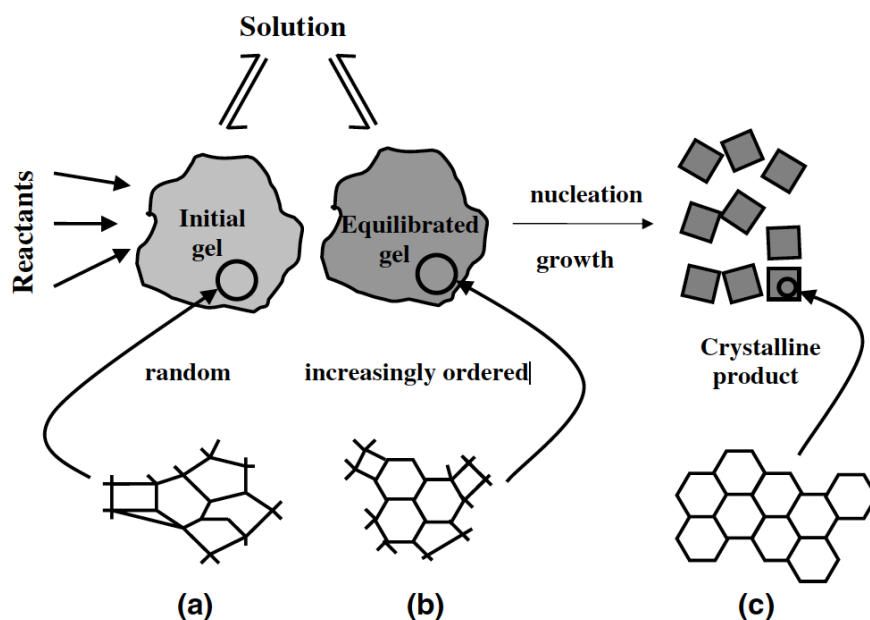


Figure 3. A simplified scheme showing the transformation of the initial reactants to the final zeolitic product. Initially, mixing of the reactants results in a disordered gel (a), which upon continuous depolymerization and repolymerization, catalyzed with mineralizer ions, results in the equilibrated aluminosilicate gel (b). Upon reaching supersaturation crystal growth is observed yielding the crystalline product (c). Reprinted from Cundy, C. S.; Cox, P. A. *Microporous Mesoporous Mater.* 2005, 82 (1–2), 1-78.

Supersaturation. The equilibrated aluminosilicate gel is typically obtained at the end of the aging period. While aging is commonly conducted at room temperature, the aged gel is placed in an autoclave and heated to elevated temperatures, typically above the

boiling point of water, to induce the nucleation and crystallization of the final product (see (c) in Figure 3). To initiate nucleation, supersaturation of the solution has to be reached.³⁸ A solution can be differentiated between stable, metastable and labile state depending on the solute concentration and a specific temperature. In a stable solution, the temperature determines the saturation concentration of the solute, whereas in metastable and labile solutions the solute concentration at a given temperature can be higher than the saturation concentration, denoted as supersaturation. Only in the labile state, nucleation and crystal growth can occur. As was described above, the aging period and elevated temperatures led to a continued increase in dissolved aluminosilicate species which transforms the stable gel solution into a labile solution. Nucleation can then occur.

Nucleation. The nucleation process is initiated by the aggregation of SBUs present in the aged and labile gel forming germ nuclei.³⁸ They then rapidly disappear through depolymerization. Over time they grow until they reach a critical size generating a viable nucleus on which crystal growth can now occur. Viable nuclei preferentially form at the boundary layer between the amorphous secondary phase and the solution as the concentration of dissolved aluminosilicate species is the highest. The activated process of nucleation depends on several factors such as the degree of supersaturation, the density and the surface energy of the nucleus. Increasing the temperature enhances the nucleation rate as well as the degree of supersaturation. Once a viable nucleus is formed it can attach additional building units resulting in the growth of crystallites. Nucleation and crystal growth occur concurrently with a rapid autocatalytic growth period followed by an inflection point as the nutrients are consumed. As crystals and nuclei consume the same precursors, the nucleation rate can be determined by a crystal size analysis. Larger crystals indicate a slower nucleation rate.

Crystal growth. Zeolite growth during crystallization can be described by a layer-by-layer model.³⁴ On the surface of a growing crystal a new building block is adsorbed from the solution. This adsorbed species then migrates to the thermodynamically favored position such as a kink site. This step is repeated until a complete layer is formed. Surface nucleation then allows the generation of a monolayer island on top of the completed layer and continuation of the layer-by-layer growth.

Templating. Another important key factor in zeolite formation is the role of the structure directing agent or template. In Al-rich zeolites such as FAU the structure

directing role is carried out by the Na⁺ cations. It is understood that Na⁺ cations also order water molecules, being a structure-making cation generating cage-like structures in the zeolite.³⁸ In various high-silica zeolites an organic template is used instead, such as tetraethylammonium hydroxide (TEA-OH) for zeolite beta (BEA). These organic compounds act as a base providing hydroxyl anions as well structure directing agents organizing the aluminosilicate precursors around them during the aging step. As the size of an organic template is significantly larger than that of a small inorganic cation the charge density is much lower, resulting in a higher Si/Al ratio in the final product.

1.4 The nature of zeolites

Beyond understanding the formation of zeolites, this thesis also takes aim at following and preventing the degradation of zeolites in aqueous media. It is believed to be important to first understand the physicochemical properties zeolites before discussing their hydrothermal stability. A zeolite is a microporous aluminosilicate made up of tetrahedral building units.¹ The center of the tetrahedron is occupied by an inorganic T-atom, such as a Si and Al and connected to other tetrahedra via the oxygen atoms sitting in the vertices of the tetrahedron. This generates a three-dimensional network of uniform pores. Classically, one can differentiate between small, medium and large pore zeolites with 8, 10 and 12 membered rings (i.e. 12-T-atoms) making up the channel apertures respectively. Depending on the synthesis procedure different framework types, as denoted by the three-letter code,³⁹ can be obtained consisting of their own specific pore network.

In the course of the presented thesis two framework types will be discussed extensively, the FAU and BEA structures. The FAU framework consists of sodalite units connected to one another via double-six membered rings. The pore aperture is a 12-membered ring, leading to the classification as a large-pore zeolite, with a 7.4 Å pore diameter. The arrangement of sodalite and double-six membered rings leads to the creation of a cage with a diameter of roughly 12 Å surrounded by 10 sodalite units. Furthermore, the FAU can be differentiated between zeolite Y and zeolite X depending on the Si/Al ratio. Synthesis of FAU typically requires the use of Na cations as structure directing agent. High-silica FAU is obtained via the use of crown ethers as template.⁴⁰

The BEA framework on the other hand, is classically considered to be a high-silica zeolite. An Al-rich version of this framework exists in the form of the natural zeolite Tschernichite.⁴¹ The BEA structure is a medium-pore zeolite with a pore aperture of 6.7 Å at the entrance of a 12-membered ring.² A variety of 4-,5- and 6-membered rings lead to a highly connected three-dimension pore network. The pore diameters are slightly larger at the intersections of these channels. Furthermore, the BEA structure is a polymorph of type A (BEA) and type B (BEB).⁴² In some cases, also polymorph C (BEC) is observed. As a consequence, the diffraction pattern consists of broad and sharp reflections. Both the FAU and BEA framework have a low framework density which is the number of T-atoms per unit cell.

Inherent to all zeolites is their porosity, which is one of their defining characteristics, leading to a molecular sieving effect, useful for the separation of gases. The porosity is also intricately linked to the second defining characteristic of zeolites which is the surface acidity. It is generated by the substitution of T-atoms in the silica framework with foreign atoms such as Al in the case of zeolites. A consequence of the substitution effect is the negative framework charge (AlO_4^- connected to SiO_4). The negative framework charge needs to be compensated which is typically achieved by alkali and earth-alkali cations. However, it is possible to exchange these cations with protons which leads to the formation of a proton compensating the negative framework charge, i.e. a Brønsted acid site. Importantly, as the external surface contribution on zeolites tend to be small, the majority of Brønsted acid sites are found within the micropores of the zeolite.

In general, acidity in zeolites can be differentiated between Brønsted and Lewis acidity. In the former, a proton (i.e. the H^+ charge balancing the framework) is exchanged between the acid and the corresponding base, whereas an electron pair is accepted in the case of Lewis acidity.⁴³ Lewis acidity is typically associated with extra-framework Al^{3+} species in the micropores.

To probe the nature of the solid acid one typically allows for the interaction between the acid and a corresponding base. A volatile base such as NH_3 or pyridine is adsorbed onto the zeolite and allowed to equilibrate.⁴⁴ The physisorbed base is then removed via evacuation, with only the chemisorbed base remaining. The latter can be removed by increasing temperatures allowing one to differentiate between different acid strengths. The setup can be coupled to a mass spectrometer and a gravimetric balance allowing

plotting of base released against the temperature. When a differentiation between acid type is favored, the vacuum system is coupled to an infrared (IR) spectrometer instead.⁴⁵⁻⁴⁷ Brønsted and Lewis acidic sites have bands at different wavenumbers. Pyridine gives a discrete IR band between at 1540 cm^{-1} for the pyridinium ion (Brønsted acid sites) and at 1450 cm^{-1} for the hydrogen bonded pyridine (Lewis acid sites). Knowing the extinction factors of these bands their integral areas can be correlated to the mass of pyridine adsorbed per mass giving a quantitative tool.⁴⁸ Additionally, IR spectroscopy enables the differentiation between acidic (e.g. bridging hydroxyls Si-O(H)-Al) and non-acidic (e.g. SiOH) hydroxyls by comparing the spectra before and after adsorption of pyridine. Additional bases include the weak base CO which allows for a more specific differentiation of weak acid sites.⁴⁹

Another criterion of a solid acid catalyst is the strength of acid sites. It can be assessed by the temperature required for desorption of the base. The acid strength varies as a function of the number of Al atoms as next nearest neighbors.³²

It now becomes clear how the microporosity and generated surface acidity led to the creation of this highly valued solid acid catalyst. As most acid sites are present in the micropores, the differing apertures allow for a screening of the feedstock only allowing select reactants to diffuse into the zeolite pores, where they are then converted to the desired products. This introduces a shape selectivity.⁵⁰ Furthermore, the repulsive interactions between the delocalized electrons of the framework and the reactant molecule affects the electronic transition state.⁵¹ Thus, the choice and modification of a zeolite can have a profound effect on the obtained selectivity for a specific reaction.

1.5 Acid-catalyzed dehydration on zeolites

Recently, it was shown that the conversion of lignin-derived molecules can be effectively managed by zeolites in aqueous phase.⁵² Due to the highly-oxygenated nature of the feedstock, significant efforts are directed at reducing the oxygen content such as hydrodeoxygenation of phenolic compounds.⁵³ As part of this process the cyclo-alcohols need to be dehydrated which was significantly slower than the accompanying hydrogenation reaction making it the rate-limiting step.⁵² Hence, the dehydration reaction, is used as an effective gauge of the catalyst performance. It is an elimination reaction that can occur either unimolecular via the E1 mechanism or bimolecular via the E2 mechanism. The E1 mechanism occurs primarily for strong

acids and weak bases and involves the formation of a carbocation as an intermediate as OH_2^+ is removed in the rate limiting step. An alkene is formed after deprotonation of the carbocation. In contrast, the E2 mechanism involves the concerted elimination of the hydroxyl group and the proton on the beta-carbon without the isolation of an intermediate.

In the classical application of zeolites in the gas-phase this type of reaction occurs primarily via the E1-mechanism,⁵⁴⁻⁵⁵ however, in the condensed aqueous phase alcohol dehydration was less defined.⁵⁶⁻⁵⁷ The relevance of condensed phase reactions on zeolites has increased over the last decade when it was found that zeolites are extremely effective catalysts for the hydrodeoxygenation of ligno-cellulosic derived phenolic compounds.⁵⁸⁻⁶⁰ The feedstock, owing to the large oxygen content, is readily soluble in water necessitating the conversion of molecules on zeolites in the presence of water.⁶¹ Zeolite chemistry in the presence of water required a reassessment of several topics such as differing degrees of acid strengths (in aqueous phase reactions all acid sites are present as hydronium ions of equal strength).⁶² In addition, the mechanism for dehydration had to be revisited. The dehydration of cyclohexanol is an important intermediate in the overall conversion scheme of ligno-cellulosic derived feedstocks as it is rate-limiting.⁵² *In situ* ^{13}C MAS NMR experiments of cyclohexanol dehydration in the aqueous phase over BEA zeolite showed that the E1-mechanism is the preferred mechanism seen in Figure 4.⁶³

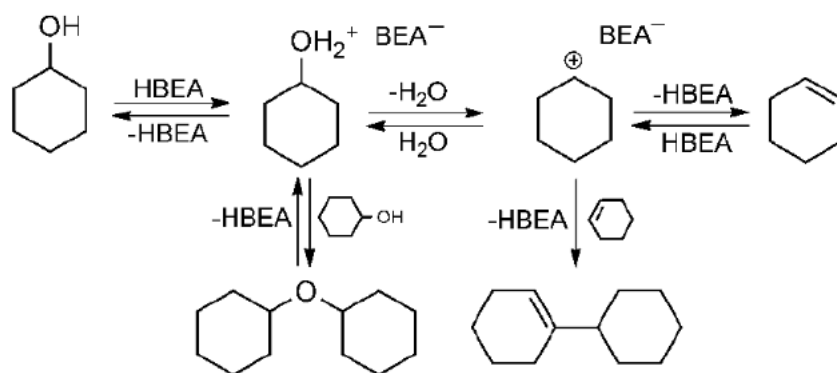


Figure 4. Proposed reaction mechanism for cyclohexanol dehydration over zeolite BEA. *In situ* ^{13}C MAS NMR helped elucidate the mechanism to be E1.⁶³

As was mentioned above, the confinement of reactants in zeolite pores can have a significant impact on reaction rates. In the aqueous phase this theory is still valid as was recently shown by Lercher et al.⁶⁴

In comparison to a homogeneous acid, H_3PO_4 , the reaction, hindered by high enthalpic and entropic barriers, proceeds at significantly higher rates in the micropores of the zeolite as the entropic barrier of activation is lowered. This was caused by the stronger association between the alcohol and the hydronium ions due to the confined environments.

Another field that warranted revisiting when turning towards zeolite applications in aqueous phase reactions was their hydrothermal stability. This will be discussed in the following chapter.

1.6 Hydrothermal stability

With the advent of zeolitic applications conducted in the liquid phase, another concept that needed revisiting is zeolite stability. Traditionally, their stability towards steaming (hydrothermal) as well as against high temperatures (thermal) is an important characteristic for gas-phase reaction. In the liquid phase, however, temperatures are typically lower and two scenarios can be differentiated; When the temperature is above the boiling point of water and when it is below.⁶⁵

1.6.1 Stability in the gas-phase

As was mentioned above, an aluminosilicate framework consists of connected Al and Si tetrahedrons which generates a framework charge, compensated by protons resulting in Brønsted acidity. The behavior of zeolites in gas-phase reactions (e.g. acid catalyzed cracking) is primarily affected by their hydrothermal stability as well as resistance to coking. Both present challenges to the design of suitable zeolite. As most industrial processes are not entirely free of moisture, the presence of water/steam in the feed can lead to dealumination and thus loss of the active sites. This is accepted to proceed via the breaking of the Si-O-Al bond and subsequent formation of extra-framework Al and possibly SiOH nests in the framework.⁶⁶ The integrity of the framework is maintained while the Al T-atoms are selectively removed. A consequence of this dealumination is the generation of very strong Brønsted acid sites as the acid strength depends on the

number of Al atoms as next nearest neighbors.³² This is seen in the superior cracking activity of steamed zeolite Y (USY), the active catalyst in the FCC process, compared to the Al-rich zeolite Y, which presented a low hydrothermal stability and cracking activity.⁶⁷

Hydrothermal stability of zeolites was also found to be a crucial element in exhaust gas treatments such as NH₃-SCR reactions. The catalyst in this reaction are Cu ions situated on the exchange positions of zeolite SSZ-13.⁶⁸⁻⁶⁹ A low Si/Al is preferred to facilitate a high loading of active Cu sites, however, depending on the Al-siting this leads to a lower hydrothermal stability. Cu²⁺ charge balancing a paired Al is hydrothermally more stable than Cu(OH)⁺ on isolated Al sites. Because of the latter, the zeolite is dealuminated and the Cu ions become inactive CuO_x clusters. Synthesis of SSZ-13 with a higher concentration of paired Al resulted in a stabilization against dealumination of the material after exchange with Cu ions.⁷⁰

Despite the good hydrothermal stability of high-silica cracking catalysts these zeolites still deactivate over time due to the formation of coke layers blocking the active sites.⁷¹ This requires the regeneration as seen in the FCC process via decomposition of coke at high temperatures. In order to alleviate the formation of coke hierarchical zeolites can be designed.

1.6.2 Stability in the condensed phase

As the conversion of oxygenates derived from biomass feedstocks occurs in the presence of ubiquitous amounts of water at elevated temperatures the stability of zeolites in hot liquid water environments experienced a significant increase in interest.⁶⁵ In contrast to alkaline conditions where extensive desilication is observed, which incidentally is used to generate a hierarchical micro- and mesoporous environment, the conditions relevant to biomass conversion reactions typically involve neutral pH water. At elevated temperatures, the water becomes more dissociated generating a large concentration of protons and hydroxyls making the zeolite material more susceptible to attack. This was shown at the example of zeolite Y which when partially dealuminated exhibits good hydrothermal stability in the gas-phase, however deteriorates rapidly when exposed to hot liquid water (>150 °C).⁷² The transformation from a crystalline and microporous material into an amorphous and consequently

inactive material was more severe for zeolite Y of higher Si/Al. Even though both, dealumination and desilication are possible pathways via the hydrolysis of the Si-O-Al and Si-O-Si bonds respectively, it was concluded that desilication is the main pathway in the condensed phase. This contrasts with the gas-phase, again highlighting the counter-intuitive behavior of zeolite Y in the gas (more stable at high Si/Al, dealumination) and liquid phase (less stable at high Si/Al, desilication). Interestingly the Al T-atoms retained their tetrahedral coordination in the amorphous material. This was later also observed in BEA through the combined use of Al K-edge X-ray absorption spectroscopy and high-field ^{27}Al MAS NMR showing that prolonged exposure to hot liquid water did not affect the Al T-site, instead suggesting that Al protects the surrounding Si. At the same time the overall framework disintegrated, shown schematically in Figure 5.

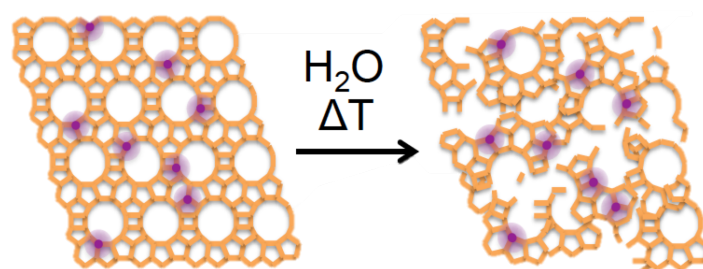


Figure 5. Schematic representation of framework decay due to hot liquid water. The Al T-sites, marked in purple, are not affected by the crumbling framework.⁷³

The degradation pathway was elucidated for the BEA framework to involve the selective leaching of Si in T1 and T2 sites found in the four-membered rings of the BEA structure.⁷³

Interestingly, this poor behavior seems restricted to zeolites with a low framework density such as BEA⁷³ and FAU⁷², whereas MFI is more resistant to framework decay.⁷⁴ A common characteristic for both BEA and high-silica FAU zeolites is their significant SiOH concentration. Resasco et al. extensively investigated the behavior of dealuminated zeolite Y (FAU) in the presence of hot liquid water,⁷⁵⁻⁷⁷ building on the observations made by Sievers et al.⁷² Their work showed that primarily the presence of SiOH groups on the zeolite surfaces facilitates framework decay.⁷⁵ The lower stability of high silica Y was correlated to the higher defect concentration generated via the

dealumination procedure. Functionalization of the zeolite surfaces, essentially capping the defect SiOH they were successful at stabilizing zeolite Y against desilication.⁷⁷

Simultaneously, Sels et al. investigated USY in hot liquid water and found that the presence of extra-framework Al had a beneficial effect on the zeolite's stability presumably correlated to the lower solubility of the extra-framework species in water as well as the likely capping of SiOH with extra-framework species.⁷⁸

1.7 Scope of this thesis

The complexity of zeolite science has been highlighted by the previous chapters. Over the last 60-70 years the number of synthetic zeolites has skyrocketed. Only several of them have found use in industrial applications at the large scale. With the anticipated implementation of zeolites in aqueous phase reactions new challenges and interests abound. The reaction networks of zeolite-catalyzed conversion reactions in the aqueous phase have been investigated extensively by others. However, a closer look at the material science of microporous zeolitic compounds is also warranted. For this purpose the thesis is split into several chapters.

FAU constitutes one of the most commonly used zeolite structure in many industrial application, as described above. Whereas in the gas-phase dealuminated FAU is highly stable, the same material experiences extensive framework decay in the liquid phase. Understanding the formation of FAU is believed to be beneficial to understanding the zeolite's paradoxical stability behavior. The FAU structure was one of the earliest structures discovered leading to a various number of proposed formation mechanisms. In the past, the crystallization was followed by characterization techniques operating under *ex situ* conditions. Only a small number of reports describe the use of *in situ* techniques. With recent advances in the MAS-NMR techniques we are able to observe changes in the Al and Na environments of the aluminosilicate gel used for the synthesis of FAU. Furthermore, a specific cell design allows us to investigate the crystallization of FAU *in situ* with the help of Al K-edge X-ray absorption spectroscopy (XAS). The combination of both methods enabled us to closely follow zeolite growth in highly alkaline conditions necessary for FAU synthesis, presented in Chapter 2 of this thesis. While these techniques match the typical S-growth curve obtained *ex situ* with X-ray

diffraction, they provide new insights into the local Na environments. This allows us to make an assignment for the various Na species present in the zeolite.

We then extended our focus to zeolite BEA another low framework-density zeolite suffering from appreciable crystallinity loss when exposed to hot liquid water. In Chapter 3 we first describe the generation and modelling of a zeolite system enriched in internal defects, i.e. SiOH. These were believed to be crucial to initiating framework hydrolysis of nearby Si-O-Si bonds. SiOH groups can be differentiated between isolated and hydrogen-bonded as well as terminal. The focus of other groups has been primarily on surfaces, thus looking more closely at the behavior of isolated and terminal SiOH. However, a consequence of the steaming procedure, used to obtain USY zeolites, prone to hydrolysis in hot liquid water, is the removal of lattice atoms which generates a hydrogen-bonded SiOH nest. Consequently, we simulated a model system enriched in SiOH nests and showed the removal of these defect nests via selective titration with a chloroalkylsilane. The stabilization procedure was followed with ^{29}Si MAS NMR and IR spectroscopy. Prolonged exposure to hot liquid water clearly presented two different behaviors depending on the defect nature and concentration in the investigated BEA zeolite.

This work is followed up by a closer look at zeolite stability under reaction conditions in Chapter 4. Previous work, including the work presented in Chapter 3 focuses primarily on the degradation of zeolites in hot liquid water. Under these conditions, it is seen unequivocally that the concentration of defects determines the zeolite lifetime. In Chapter 4 we synthesize and characterize a range of catalytically relevant BEA zeolites spanning Si/Al from 12-110. The number of defects was determined qualitatively using ^{29}Si CP MAS NMR as well as IR spectroscopy. In addition we develop a trickle-bed reactor able to unambiguously measure the dissolution rate of the zeolite, establishing a higher rate for Si-leaching compared to Al-leaching, confirming desilication as the main pathway. The measured rate at which Si is lost, is higher for materials of higher defect concentrations, agreeing with the loss of crystallinity.

Testing materials of higher defect concentrations for their performance in cyclohexanol dehydration, however, led to an unprecedented and unexpected results largely independent of the defect concentration. Measuring the uptake of cyclohexanol from an aqueous solution allowed us to determine the concentration of water in the micropores. Synthesizing a defect-free and defect-rich BEA zeolite at comparable

Chapter 1 – Introduction

Brønsted acid site concentration allowed us to deconvolute the role of defects and Brønsted acid sites, which have been mostly ignored in the literature, on framework decay.

Chapter 5 finally summarizes the various findings arriving at a conclusion considered to target the design of robust zeolites for the aqueous phase conversion of oxygenates.

REFERENCES

1. McCusker, L. B.; Baerlocher, C., Zeolite structures. In *Stud. Surf. Sci. Catal.*, Čejka, J.; Bekkum, H. v., Eds. Elsevier: 2005; Vol. 157, pp 41-64.
2. Baerlocher, C.; McCusker, L. B. Database of Zeolite Structures. <http://www.iza-structure.org/databases/> (accessed October 2016).
3. Cronstedt, A. F., Rön och beskrifning om en obekant bärg art, som kallas Zeolites. 1756; Vol. 18, pp 120-130.
4. de St Claire Deville, H., In *Comptes Rendus Acad. Sci.*, 1862; Vol. 54, p 324.
5. Friedel, G., New experiments on zeolites. In *Bull. Soc. Fr. Mineral. Cristallogr.*, 1896; Vol. 19, pp 363-390.
6. Weigel, O.; Steinhoff, E. *Z. Kristallogr* 1925, *61*, 125-154.
7. Flanigen, E. M.; Broach, R. W.; Wilson, S. T., Introduction. In *Zeolites in Industrial Separation and Catalysis*, Wiley-VCH Verlag GmbH & Co. KGaA: 2010; pp 1-26.
8. Barrer, R. M.; Hinds, L.; White, E. A. *Journal of the Chemical Society (Resumed)* 1953, (0), 1466-1475.
9. Barrer, R. M., *Zeolite and Clay Minerals*. Academic Press: New York, 1978.
10. Barrer, R. M. *Journal of the Chemical Society (Resumed)* 1948, (0), 127-132.
11. Milton, R. M., Molecular Sieve Science and Technology. In *Zeolite Synthesis*, American Chemical Society: 1989; Vol. 398, pp 1-10.
12. Barrer, R.; Denny, P. *Journal of the Chemical Society (Resumed)* 1961, 971-982.
13. Wadlinger, R. L.; Kerr, G. T.; Rosinski, E. J., Catalytic composition of a crystalline zeolite. Google Patents: 1967.
14. Argauer, R. J.; Landolt, G. R., Crystalline zeolite zsm-5 and method of preparing the same. Google Patents: 1972.
15. Cundy, C. S.; Cox, P. A. *Chem. Rev.* 2003, *103* (3), 663-702.
16. Davis, M. E.; Saldarriaga, C.; Montes, C.; Garces, J.; Crowder, C. *Nature* 1988, *331* (6158), 698-699.
17. Davis, M. E.; Saldarriaga, C.; Montes, C.; Garces, J.; Crowder, C. *Zeolites* 1988, *8* (5), 362-366.
18. Estermann, M.; McCusker, L. B.; Baerlocher, C.; Merrouche, A.; Kessler, H. *Nature* 1991, *352* (6333), 320-323.

19. Beck, J. S.; Vartuli, J. C.; Roth, W. J.; Leonowicz, M. E.; Kresge, C. T.; Schmitt, K. D.; Chu, C. T. W.; Olson, D. H.; Sheppard, E. W.; McCullen, S. B.; Higgins, J. B.; Schlenker, J. L. *J. Am. Chem. Soc.* 1992, *114* (27), 10834-10843.
20. Kresge, C. T.; Leonowicz, M. E.; Roth, W. J.; Vartuli, J. C.; Beck, J. S. *Nature* 1992, *359* (6397), 710-712.
21. Zhao, D.; Feng, J.; Huo, Q.; Melosh, N.; Fredrickson, G. H.; Chmelka, B. F.; Stucky, G. D. *Science* 1998, *279* (5350), 548-552.
22. Li, H.; Eddaoudi, M.; O'Keeffe, M.; Yaghi, O. M. *Nature* 1999, *402* (6759), 276-279.
23. Lewis, G. J.; Miller, M. A.; Moscoso, J. G.; Wilson, B. A., Process for preparing crystalline aluminosilicate compositions using charge density matching. Google Patents: 2009.
24. Mintova, S.; Gilson, J.-P.; Valtchev, V. *Nanoscale* 2013, *5* (15), 6693-6703.
25. Li, Q.; Hedlund, J.; Sterte, J.; Creaser, D.; Bons, A.-J. *Microporous Mesoporous Mater.* 2002, *56* (3), 291-302.
26. Jiang, J.; Jorda, J. L.; Diaz-Cabanas, M. J.; Yu, J.; Corma, A. *Angew. Chem. Int. Ed.* 2010, *49* (29), 4986-4988.
27. Roth, W. J.; Nachtigall, P.; Morris, R. E.; Wheatley, P. S.; Seymour, V. R.; Ashbrook, S. E.; Chlubná, P.; Grajciar, L.; Položij, M.; Zukal, A.; Shvets, O.; Čejka, J. *Nat Chem* 2013, *5* (7), 628-633.
28. Lauriente, D. H.; Inoguchi, Y., *The Chemical Economics Handbook*. SRI Consulting: 2005.
29. Lowenstein, W. *Am. Mineral.* 1954, *39*, 92.
30. Čejka, J.; van Bekkum, H.; Corma, A.; Schueth, F., *Introduction to Zeolite Molecular Sieves*. Elsevier Science: 2007.
31. Kalló, D. *Reviews in Mineralogy and Geochemistry* 2001, *45* (1), 519-550.
32. Pine, L. A.; Maher, P. J.; Wachter, W. A. *J. Catal.* 1984, *85* (2), 466-476.
33. Yilmaz, B.; Müller, U. *Top. Catal.* 2009, *52* (6), 888-895.
34. Cundy, C. S.; Cox, P. A. *Microporous Mesoporous Mater.* 2005, *82* (1-2), 1-78.
35. Corma, A.; Davis, M. E. *ChemPhysChem* 2004, *5* (3), 304-313.
36. Petrovic, I.; Navrotsky, A.; Davis, M. E.; Zones, S. I. *Chem. Mater.* 1993, *5* (12), 1805-1813.

37. Piccione, P. M.; Laberty, C.; Yang, S.; Cambor, M. A.; Navrotsky, A.; Davis, M. E. *J. Phys. Chem. B* 2000, *104* (43), 10001-10011.
38. Feijen, E. J. P.; Martens, J. A.; Jacobs, P. A., Hydrothermal Zeolite Synthesis. In *Preparation of Solid Catalysts*, G. Ertl; H. Knözinger; Weitkamp, J., Eds. Wiley-VCH Verlag GmbH: 2008; pp 262-284.
39. McCusker, L. B.; Liebau, F.; Engelhardt, G. *Pure Appl. Chem.* 2001, *73* (2), 381-394.
40. Dougnier, F.; Patarin, J.; Guth, J. L.; Anglerot, D. *Zeolites* 1992, *12* (2), 160-166.
41. Alberti, A.; Cruciani, G.; Galli, E.; Merlino, S.; Millini, R.; Quartieri, S.; Vezzalini, G.; Zanardi, S. *J. Phys. Chem. B* 2002, *106* (39), 10277-10284.
42. Newsam, J. M.; Treacy, M. M. J.; Koetsier, W. T.; Gruyter, C. B. D. *Proc. R. Soc. London, Ser. A* 1988, *420* (1859), 375-405.
43. Weitkamp, J.; Hunger, M., Chapter 22 - Acid and Base Catalysis on Zeolites. In *Stud. Surf. Sci. Catal.*, Jiří Čejka, H. v. B. A. C.; Ferdi, S., Eds. Elsevier: 2007; Vol. Volume 168, pp 787-835.
44. Corma, A. *Chem. Rev.* 1995, *95* (3), 559-614.
45. Parry, E. P. *J. Catal.* 1963, *2* (5), 371-379.
46. Hughes, T. R.; White, H. M. *J. Phys. Chem.* 1967, *71* (7), 2192-2201.
47. Lercher, J. A.; Jentys, A., Chapter 13 - Infrared and Raman Spectroscopy for Characterizing Zeolites. In *Stud. Surf. Sci. Catal.*, Jiří Čejka, H. v. B. A. C.; Ferdi, S., Eds. Elsevier: 2007; Vol. Volume 168, pp 435-476.
48. Emeis, C. A. *J. Catal.* 1993, *141* (2), 347-354.
49. Busca, G.; Lorenzelli, V. *Materials Chemistry* 1982, *7* (1), 89-126.
50. Derouane, E. G. *J. Catal.* 1986, *100* (2), 541-544.
51. Zicovich-Wilson, C. M.; Corma, A.; Viruela, P. *J. Phys. Chem.* 1994, *98* (42), 10863-10870.
52. Zhao, C.; He, J.; Lemonidou, A. A.; Li, X.; Lercher, J. A. *J. Catal.* 2011, *280* (1), 8-16.
53. Serrano-Ruiz, J. C.; Luque, R.; Sepulveda-Escribano, A. *Chem. Soc. Rev.* 2011, *40* (11), 5266-5281.
54. Gentry, S. J.; Rudham, R. *J. Chem. Soc., Faraday Trans. 1* 1974, *70*, 1685-1692.
55. Jacobs, P. A.; Tielen, M.; Uytterhoeven, J. B. *J. Catal.* 1977, *50* (1), 98-108.
56. Akiya, N.; Savage, P. E. *Ind. Eng. Chem. Res.* 2001, *40* (8), 1822-1831.

57. Carey, F. A.; Sundberg, R. J., *Advanced Organic Chemistry: Part A: Structure and Mechanisms*. Springer Science & Business Media: 2007; p 473.
58. Zhao, C.; Camaioni, D. M.; Lercher, J. A. *J. Catal.* 2012, 288, 92-103.
59. Zhao, C.; Lercher, J. A. *Angew. Chem.* 2012, 124 (24), 6037-6042.
60. Song, W.; Liu, Y.; Baráth, E.; Wang, L. L.; Zhao, C.; Mei, D.; Lercher, J. A. *ACS Catal.* 2016, 6 (2), 878-889.
61. Zhao, C.; Lercher, J. A. *Angew. Chem.* 2012, 124 (24), 6037-6042.
62. Vjunov, A.; Derewinski, M. A.; Fulton, J. L.; Camaioni, D. M.; Lercher, J. A. *J. Am. Chem. Soc.* 2015, 137 (32), 10374-10382.
63. Vjunov, A.; Hu, M. Y.; Feng, J.; Camaioni, D. M.; Mei, D.; Hu, J. Z.; Zhao, C.; Lercher, J. A. *Angew. Chem. Int. Ed.* 2014, 53 (2), 479-482.
64. Liu, Y.; Vjunov, A.; Shi, H.; Eckstein, S.; Camaioni, D. M.; Mei, D.; Barath, E.; Lercher, J. A. *Nat. Commun.* 2017, (8), 14113.
65. Ennaert, T.; Van Aelst, J.; Dijkmans, J.; De Clercq, R.; Schutyser, W.; Dusselier, M.; Verboekend, D.; Sels, B. F. *Chem. Soc. Rev.* 2016, 45 (3), 584-611.
66. Maier, S. M.; Jentys, A.; Lercher, J. A. *J. Phys. Chem. C* 2011, 115 (16), 8005-8013.
67. Katada, N.; Kageyama, Y.; Takahara, K.; Kanai, T.; Ara Begum, H.; Niwa, M. *J. Mol. Catal. A: Chem.* 2004, 211 (1-2), 119-130.
68. Paolucci, C.; Parekh, A. A.; Khurana, I.; Di Iorio, J. R.; Li, H.; Albarracin Caballero, J. D.; Shih, A. J.; Anggara, T.; Delgass, W. N.; Miller, J. T.; Ribeiro, F. H.; Gounder, R.; Schneider, W. F. *J. Am. Chem. Soc.* 2016, 138 (18), 6028-6048.
69. Beale, A. M.; Gao, F.; Lezcano-Gonzalez, I.; Peden, C. H. F.; Szanyi, J. *Chem. Soc. Rev.* 2015, 44 (20), 7371-7405.
70. Prodinge, S.; Derewinski, M. A.; Wang, Y.; Washton, N. M.; Walter, E. D.; Szanyi, J.; Gao, F.; Wang, Y.; Peden, C. H. F. *Applied Catalysis B: Environmental*.
71. Devaraj, A.; Vijayakumar, M.; Bao, J.; Guo, M. F.; Derewinski, M. A.; Xu, Z.; Gray, M. J.; Prodinge, S.; Ramasamy, K. K. *Scientific Reports* 2016, 6, 37586.
72. Ravenelle, R. M.; Schüßler, F.; D'Amico, A.; Danilina, N.; van Bokhoven, J. A.; Lercher, J. A.; Jones, C. W.; Sievers, C. *J. Phys. Chem. C* 2010, 114 (46), 19582-19595.
73. Vjunov, A.; Fulton, J. L.; Camaioni, D. M.; Hu, J. Z.; Burton, S. D.; Arslan, I.; Lercher, J. A. *Chem. Mater.* 2015, 27 (9), 3533-3545.
74. Gounder, R. *Catalysis Science & Technology* 2014, 4 (9), 2877-2886.

Chapter 1 – Introduction

75. Zhang, L.; Chen, K.; Chen, B.; White, J. L.; Resasco, D. E. *J. Am. Chem. Soc.* 2015, *137* (36), 11810-11819.
76. Zapata, P. A.; Faria, J.; Ruiz, M. P.; Jentoft, R. E.; Resasco, D. E. *J. Am. Chem. Soc.* 2012, *134* (20), 8570-8578.
77. Zapata, P. A.; Huang, Y.; Gonzalez-Borja, M. A.; Resasco, D. E. *J. Catal.* 2013, *308*, 82-97.
78. Ennaert, T.; Geboers, J.; Gobechiya, E.; Courtin, C. M.; Kurttepli, M.; Houthoofd, K.; Kirschhock, C. E. A.; Magusin, P. C. M. M.; Bals, S.; Jacobs, P. A.; Sels, B. F. *ACS Catal.* 2015, *5* (2), 754-768.

Chapter 2

Formation of Faujasite Followed by *in situ* Spectroscopy

Advanced *in situ* spectroscopic techniques in combination with a classical *ex situ* approach was employed to identify and track the atomistic changes during the formation process of the Faujasite (FAU) zeolite. Prior to crystallization, X-ray absorption near the edge (XANES) could observe the rearrangement of the gel into a more equilibrated state, while the extended X-ray absorption fine spectra (EXAFS) inferred a steady Al coordination throughout the synthesis. Using solid-state NMR the autocatalytic transformation from an amorphous gel into crystalline material was then observed. With the help of sodium-23 different environments in the growing zeolite crystal could be identified and allowed for the postulation of a mechanism involving the stepwise formation of the zeolite. This highlights the enhanced capabilities of the combinatorial use of these *in situ* techniques.

INTRODUCTION

60 years after Barrer and co-workers first published the formation of zeolites^{1,2}, an understanding of the formation mechanism of these aluminosilicates is still highly sought after.³ The reviews by Cundy and Cox highlight the numerous proposed formation mechanisms postulated over the last 6 decades.^{3,4} Barrer initially proposed the formation of zeolites via the fusing of secondary building units (SBU), consisting of tetrahedral and polyhedral linked in ring shape, into the frameworks.⁵ This solution-mediated process was later supported by Kerr as well as Zhdanov.⁶⁻⁷ At the same time Flanigan and Breck proposed crystal growth via transformation of the solid hydrogel.^{4,8-9} These and several other mechanisms were later generalized by Guth et al.^{3,10} While experimental limitations in the past led to *ex situ* characterization of the nucleation and crystallization steps of zeolite synthesis, newly developed capabilities allow *in operando* measurements during the synthesis.¹¹

In order to accurately describe the formation mechanism of zeolites it is important to continuously observe changes within the reactive solution. Typically used high temperatures and autogenous pressures, as well as highly alkaline reaction conditions complicate matters. *Ex situ* characterization is usually done either by continuous sampling of a gel fraction or by preparing a series of gels in separate reaction vessels that are periodically stopped for analysis. Ensuring reproducibility for each vessel and avoiding chemical alteration during sampling (e.g. pressure or temperature drops) as well as having to separate the solid product from the liquid reactants and subsequent drying are considered to be major drawbacks of this classical approach to the investigation of reaction mechanisms.¹¹

Therefore, developing methods for *in situ* characterization has become crucial for understanding zeolite formation. Amongst a plethora of *in situ* methods, it is essential to choose a method that allows a rapid gathering of data without disturbing the sample. X-ray Diffraction (XRD)¹¹ and microscopy¹² have both been applied as *in situ* methods; however, they suffer from inadequate measurement speeds and/or sensitivity. Other measurement techniques such as IR, light scattering, NMR or pH measurements also have their own advantages and disadvantages.¹³ Navrotsky et al. demonstrated the applicability of *in situ* calorimetry to follow the crystallization processes for FAU.¹³

Chapter 2 – Formation of Faujasite Followed by *in situ* Spectroscopy

The ordered structure of FAU consists of sodalite cages connected to one another via double six membered rings (D6R).¹⁴ As a result large cavities are formed – the so-called supercages. Depending on the Al content, which populates only one type of T-site, one either defines these materials as zeolite X (Si/Al < 1.5) or zeolite Y (Si/Al > 1.5). This differentiation is characterized by the possible exchange positions of Na cations.¹⁵ At such low Si/Al ratios, ordering of the Si and Al atoms in the framework becomes important as investigated by several groups.¹⁶⁻¹⁹ Using ²⁹Si MAS NMR Melchior et al. proposed the formation of FAU to depend on the necessary ordering of sub-units such as sodalite units¹⁹ and D6R.²⁰ This was based on the deconvolution of the spectra and limiting the number of possible orientations of the sub-units by excluding Al-O-Al bonds (Lowenstein rule) and minimization of Al-Al next nearest neighbors (Al-pairs: Al-O-Si-O-Al).¹⁹

In our work we use a powerful combination of both *in situ* and *ex situ* characterization techniques to accurately follow the mechanism of the faujasite (FAU) zeolite formation. The relatively high abundance of both Na and Al metals in this zeolite provides convenient probe atoms to follow the subtle changes during the crystallization process. Recent developments in *in situ* MAS-NMR allow us to employ both ²⁷Al and ²³Na MAS NMR at high spinning rates.²¹ In contrast to liquid phase NMR spectroscopy, the MAS-NMR approach allows us to obtain high resolution spectra on both liquid and solid species because the various nuclear interactions, e.g. chemical shift anisotropy and magnetic susceptibility variations across the sample, are averaged out by the technique of magic angle spinning (MAS). This technique also takes advantage of the fast relaxation times and high natural abundance of the NMR-active isotopes ²⁷Al and ²³Na. In addition *in situ* Al-XAFS measurements enables insights into the first few coordination spheres surrounding Al during synthesis. Finally, *ex situ* characterization using XRD supplemented the information gained from these *in situ* measurements. It is important to understand that no single method enables the accurate description of zeolite formation; a combination of techniques is needed to understand this complex chemistry.

Chapter 2 – Formation of Faujasite Followed by *in situ* Spectroscopy

EXPERIMENTAL PROCEDURE

SYNTHESIS PROCEDURE

Classical synthesis

Faujasite was synthesized using the procedure described by Navrotsky et al.¹³ 2.2 g of the silica source (Ludox HS-40, Sigma Aldrich) and 1.38 g of NaOH (Sigma Aldrich) were dissolved in 5.14 g H₂O (MilliQ). Separately, an Al solution was prepared by dissolving 0.81 g of NaAlO₂ (Sigma Aldrich) in 6.17 g H₂O (MilliQ). The Si and Al solutions were then mixed and aged under stirring at room temperature for 30 min. The gel composition is as follows: 55 Na₂O: 10 Al₂O₃: 35 SiO₂: 1750 H₂O. Once ageing was complete, the gel was placed inside Teflon lined autoclaves, put inside an oven and heated to 70 °C at a rate of 0.25 °C/min and kept at this temperature for 25 hours. At set intervals autoclaves were removed from the oven, cooled to room temperature and the synthesized material separated from the liquid phase via centrifugation. The solid residue was washed several times with distilled water and then dried at 70 °C overnight before undergoing further characterization.

Faujasite synthesis followed *in situ* via Al K-edge XAFS

The Al K-edge XAFS experiments were performed at the Phoenix II, elliptical undulator beamline at the Swiss Light Source (SLS) at the Paul Scherrer Institute (PSI), Switzerland. Energy calibration was achieved by setting the inflection point of an Al foil spectrum to 1559.6 eV. The double-crystal monochromator employed a set of KTiOPO₄ (011) crystals to provide an energy resolution of ~ 0.6 eV over a scan range for the Al K-edge from 1500 to 2150 eV. Two Ni-coated mirrors were set at an angle of 1.45° to provide cutoff of higher harmonics. An unfocused 1.0 × 1.0-mm beam having a flux of ~ 10⁹ photons/sec was used. Measurements were performed in fluorescence mode. I_0 was measured as total electron yield signal taken from a 0.5 μm thin polyester foil, which was coated with 50 nm of Ni. This I_0 detector was held in a miniaturized vacuum chamber (2.9×10⁻⁶ mbar), which is separated by a thin Kapton foil from the measurement chamber itself. The X-ray fluorescence was detected using a 4-element Vortex Si-drift diode detector. ATHENA²²⁻²³ software package was used for background processing necessary to extract the $\chi(k)$ data from the background function. A Fourier filter cutoff distance, R_{bkg} , of 1.0 Å was used. The XAFS data were

Chapter 2 – Formation of Faujasite Followed by *in situ* Spectroscopy

weighted by k^2 , and truncated using a Hanning window with $dk = 1.0 \text{ \AA}^{-1}$ in the range of $1.5 < k < 8.0 \text{ \AA}^{-1}$.

The faujasite synthesis gel was prepared following exactly the same recipe as described above and was then aged for 30 min under stirring conditions. The gel was loaded in the EXAFS cell (see Appendix Figure A3). The cell was loaded in the vacuum chamber and the synthesis was followed *in situ* from 25 to 70 °C. The temperature ramp was set to 0.1 °C/min. Once the set point temperature was reached the gel was allowed an additional hour to react in order to achieve maximum crystallinity. Upon completion the product was filtered and washed several times with distilled H₂O.

In situ synthesis – NMR

Typically, 300 mg gel of the same composition as described for the classical synthesis was loaded in the high temperature and high pressure MAS rotor for *in situ* MAS NMR experiments. The temperature was raised by 0.25 °C/min to 70 °C and kept at this temperature for 15 h. *In situ* ²³Na and ²⁷Al MAS NMR measurements were carried out on a Varian 500 MHz NMR spectrometer using a 7.5 mm HX MAS probe with a spinning rate of 3 kHz at resonance frequencies of 132.3, 130.3 MHz respectively. ²³Na MAS NMR was additionally measured on a Varian 300 MHz spectrometer with a 7.5 mm HX MAS probe, spinning at 2 kHz and 81.8 MHz resonance frequency. Variable temperature experiments were conducted with the commercially available heating stack provided by Varian company, and the real temperature in the rotor was calibrated with ethylene glycol. ²³Na MAS NMR spectra were recorded using a pulse width 1.5 μs for a $\pi/4$ pulse, and 128 scans were accumulated with 1 s recycle delay. The chemical shifts were externally referenced to 1.0 M NaCl aqueous solution at 0 ppm. ²⁷Al MAS NMR experiments were acquired using a pulse width 1 μs for a $\pi/4$ pulse, 128 scans, and a 1 s recycle delay. The spectra were externally referenced to 1.0 M Al(NO₃)₃ aqueous solution. Over the course of the experiment, 400 spectra were obtained during the isothermal stage in addition to those measured at varying temperatures. The spectra were analyzed with MestreNova software. Initially, an exponential apodization function (100 Hz) was applied to the time domain free induction decay. In addition the 400 spectra obtained during the isothermal stage were averaged to 40 and 20 spectra for ²⁷Al and ²³Na respectively. The different Al and Na

Chapter 2 – Formation of Faujasite Followed by *in situ* Spectroscopy

species were assessed by deconvolution of the peaks with symmetric peaks of Lorentzian/Gaussian lineshape, which was kept constant for the individual species. All other parameters were optimized to obtain the smallest error. An example of a line-fitting can be seen in Figure A7.

Ex situ characterization

Samples obtained from classical and *in situ* syntheses were additionally characterized *ex situ* using the following methods.

X-ray diffraction (XRD). XRD patterns were typically collected with a Rigaku Mini Flex II bench top X-ray diffractometer using a Cu-K α radiation of 0.154056 nm (30 kV and 15 mA). The step size was 2°/min ranging from 5-65°.

Helium ion microscopy (HIM). HIM images were obtained using 30 keV He ions with 1.0 pA beam current at normal incidence. Secondary electrons were detected using an Everhart–Thornley detector. For HIM imaging, a very thin layer of carbon (<1 nm) was coated using a carbon sputter deposition system as the samples were completely insulating. The instrument resolution was 0.35 nm.

Atomic absorption spectroscopy (AAS). The elemental composition of the samples was determined by atomic absorption spectroscopy in a Unicam M Series Flame-AAS equipped with an FS 95 autosampler and a GF 95 graphite furnace.

²⁷Al MAS NMR. Hydrated spectra were collected on a Varian 500 MHz spectrometer using a 4 mm HX probe. ²⁷Al experiments were conducted using a 0.6 μ s pulse width for a $\pi/20$ pulse angle. Recycle delays of 1 s were applied to fully relax the spins. 5000 scans at a spinning rate of 16 kHz were collected and analyzed using MestreNova software. The peaks were referenced externally to a 1.0 M Al(NO₃)₃ solution set to 0 ppm. In order to fully hydrate all Al the samples were stored in a desiccator with Ca(NO₃)₂ solution for a minimum of 48h. Upon completion of a ²⁷Al experiment, the ²³Na spectrum was collected immediately. A pulse width of 1.4 μ s was used to simulate a $\pi/20$ pulse. 5000 scans with a pulse delay of 1 s were accumulated at a spinning rate of 16 kHz. The signal was referenced to 1.0 M NaCl solution at 0 ppm.

²³Na MAS NMR. In addition to the hydrated samples, the material obtained was also investigated with solid state NMR in a dehydrated state. Dehydration was achieved by heating the sample to 400 °C (5 °C/min) and keeping it at this temperature for 10h.

Chapter 2 – Formation of Faujasite Followed by in situ Spectroscopy

Experiments were conducted at different field strengths. i) A Bruker 500 MHz spectrometer with a triple-resonance wide-bore probe was used. The resonance frequency was set to 132.3 MHz and the sample was spun at 10 kHz. A pulse width of 1.4 μ s was used corresponding to a $\pi/20$ pulse. 5000 scans with a pulse delay of 1 s were accumulated at a spinning rate of 16 kHz. The signal was referenced to solid NaCl set to 0 ppm.

RESULTS & DISCUSSION

Ex situ XRD

FAU was synthesized for a classical kinetic approach as described in the experimental procedure with the synthesis being stopped and the product worked up at specific times. Analysis of the chemical composition (Si/Al 1.1) indicates that the final synthesized FAU structure consists of the X-type zeolite.

The relative crystallinity assessed with X-ray diffraction was plotted for each sample against time, shown in Figure 1. Three stages can be identified in the S-shape curve typical for zeolitisation. Initially, no crystallinity associated with FAU is observed for 3.75 hours. This stage is known as the induction period.^{24,25} During the induction period, viable nuclei continuously aggregate and dissolve, until a certain critical mass is reached.³ In order for crystallites to form, it has to be energetically favorable to add building units to viable nuclei, rather than for these viable nuclei to continue to dissolve. Passing this energetic barrier, X-ray detectable crystallites (> 50 nm) are formed, indicated by the onset of crystallinity, marking the end of the induction period. This initiates the second stage of the crystallization process involving a rapid formation of crystallites, yielding a relative crystallinity of 85% within 6 hours. An abundance of nutrients present in the gel aid the formation of the zeolite at this point. Consumption of nutrients eventually reduces the crystallization rate indicated by the third stage ranging from 6 hours until the end of the experiment.

In the diffractograms of the samples obtained during the initial 6 hours, diffraction peaks in addition to the broad hump associated with amorphous material ($2\theta = 29^\circ$) can be identified (Figure A1a). The peak positions agree well with those proposed for a variety of sodium silicates (Na_xSiO_y). The gradual disappearance of the peaks (Figure 1) in the course of the experiment suggests a possible transformation into the zeolite as the silicate combines with the available Al sources. However, as these samples were examined after interrupting the synthesis, followed by washing and drying at 70 °C, the sodium silicates could have been a consequence of this work up procedure. Indeed, no presence of these silicates were found when investigating the aged gel in a capillary without separation (Figure A1c). This uncertainty highlights the need for an *in situ* approach to zeolite formation.

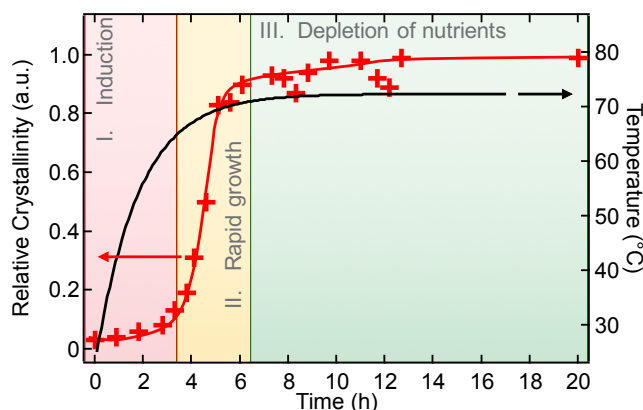


Figure 1. Crystallization curve for Faujasite determined by XRD measurements of samples characterized *ex situ*. The time resolved diffractograms can be found in the Appendix (Figure A1b). Color-coding is reported in the legend.

In situ Al XAFS analysis

The main drawback of XRD in addition to the reported *ex situ* approach is the minimum size requirement for crystallites (> 10 nm)²⁶⁻²⁷, to yield observable diffraction lines. This results in a time, i.e. the induction period, where subtle changes in the structure cannot be measured. To circumvent this, we performed *in situ* XAFS measurements probing the electronic and geometric structure of the Al species during FAU synthesis. Let us first turn to the Al K-edge XANES measurement results. The obtained temperature series of XANES spectra as well as the respective reaction times are shown in Figure 2a. The strong peak at ~ 1565.5 eV is assigned to tetrahedral Al.²⁸ There is a pre-edge peak at 1562.4 eV that is mostly responsive to bond-length and angle distortions of the Al-(O)₄ tetrahedron while the near-edge feature at 1563.8 eV is primarily due to variation in structure in the second and higher shells.²⁹ The Figure 2a provides an expanded view that covers both of these spectral transitions. For this region, most of the change occurs within the first three hours of heating and thereafter remains mostly constant. This suggests, in agreement with XRD, that a FAU precursor persists up to about 4 hours when it is then mostly consumed by formation and growth of the FAU crystallite. This precursor can be attributed to the reorganization of the amorphous aluminosilicate gel into a more equilibrated gel initiating the nucleation and crystallization step.

Chapter 2 – Formation of Faujasite Followed by *in situ* Spectroscopy

Figure 2b expands the region between 1568 and 1572 eV. There is a constant decrease in the intensity of this band over the course of the synthesis. Changes in this region are tentatively assigned to the alteration of the T-site in higher shells or the T-site proximity of Na⁺ or water in the forming FAU crystallite. Note that the region of this band spans only 4 eV around 1570 eV, that is consistent with a tetrahedral site and not octahedral species, whose band occur over a broader region between 1569 to 1577 eV.³⁰ Changes in this region suggest differing degrees of localization of the Na⁺ about the Al site.³¹ The band intensity decreases continuously over the entire period suggesting a changing Na⁺ association as the FAU crystallite size continues to grow. In the zeolite, the Na⁺ can span two or more Al T-sites because of their close proximity whereas in the small precursor, Na⁺ is more localized closer to each individual Al site. The higher intensity of this band suggests that the Al of the precursor must have Na⁺ association to the T-site that is more like that in sodium aluminate.³¹

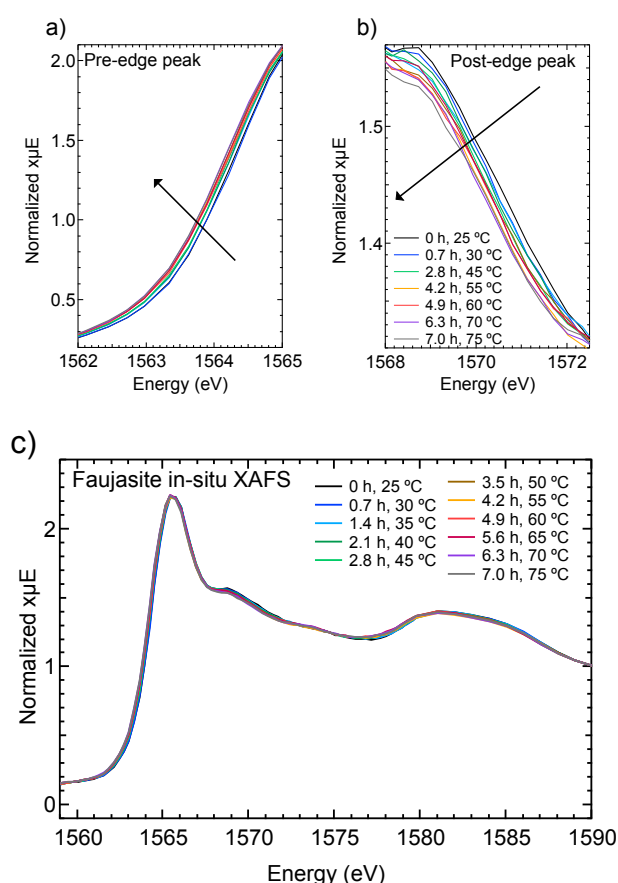


Figure 2. The normalized Al-XANES acquired at different temperatures during the FAU synthesis experiment followed *in situ*. a) and b) demonstrate the minor changes in the

Chapter 2 – Formation of Faujasite Followed by *in situ* Spectroscopy

spectral shape in the pre-edge region (1562-1564 eV) and in the ~ 1570 eV region, respectively. The temperature color-coding as well as the respective reaction times are reported in the legend.

The geometry of the Al-species during the synthesis reaction is monitored via Al EXAFS shown as a temperature series in Figure 3. We note that there is no significant change in the peak shape or position up to ~ 4.5 Å from the absorber Al atom in the course of the reaction. This suggests that the majority of primary building blocks, i.e. tetrahedral Al with a single shell of Si $[\text{Al}(\text{OSiOH})_4]^-$, are formed during the gel aging procedure. The continuous zeolite framework assembly during the synthesis reaction has little to no effect on the nature of Al. Incidentally, the material's crystallinity upon completion of the experiment assessed with XRD (diffractogram shown in Figure A1) is the same degree as observed for the classical approach.

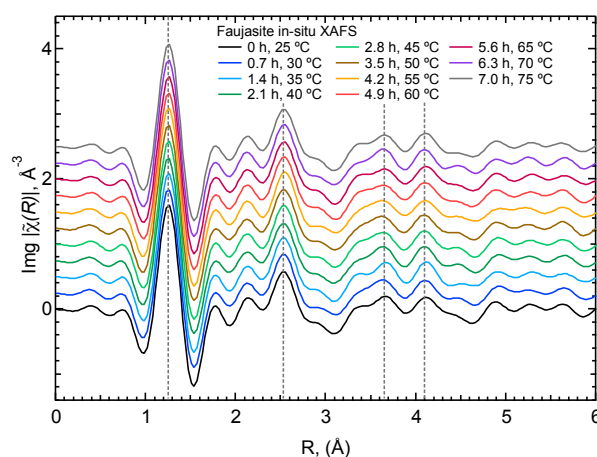


Figure 3. The k^2 -weighted Al-EXAFS $\text{Img}[\chi(R)]$ spectra acquired at different temperatures during the FAU synthesis experiment followed *in situ*. Vertical bars are added to simplify peak position comparison. The temperature color-coding as well as the respective reaction times are reported in the legend.

In situ ^{27}Al MAS NMR

While XAFS is sensitive to the first three or four shells (Al-O-Si-O-Al) surrounding an Al atom, hereafter known as short to medium range order, we now move to MAS-NMR techniques. FAU consists solely of silicon, aluminum, oxygen, and sodium. The low natural abundance and long relaxation time of ^{29}Si and ^{16}O isotopes exclude them as useful probe molecules in *in situ* NMR reaction studies. ^{27}Al and ^{23}Na on the other

Chapter 2 – Formation of Faujasite Followed by *in situ* Spectroscopy

hand, have a 100% natural abundance yielding high sensitivity and their fast relaxation times makes them well suited for following small changes during zeolite synthesis.³² A minor drawback, their quadrupolar nature, due to spins 3/2 (²³Na) and 5/2 (²⁷Al) respectively, can lead to line broadening at low magnetic fields.³³⁻³⁵

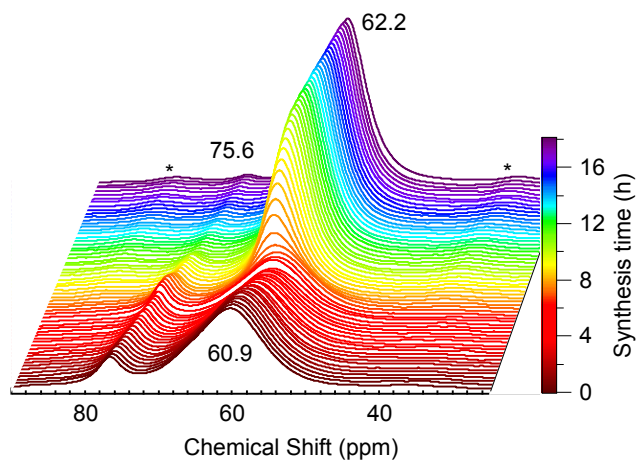
The *in situ* spectra for the Al environment during the FAU synthesis are shown in Figure 4. The spectra taken during the heating phase can be also found separately in the Appendix (Figure A4a). Clearly, two species can be observed in a region typically associated with tetrahedral Al. The significantly larger and broader species ($Al_{[Fr]}$) is attributed to tetrahedral Al in a solid environment, e.g. a portion of a zeolite framework. The smaller and narrower peak at 76 ppm was found to be linked to tetrahedral Al in the liquid phase, further corroborated by measuring only the clear liquid part of the gel after centrifugation (Figure A4b). $Al(OH)_4^-$ has a chemical shift of 80 ppm with the slight difference in chemical shift being attributed to the partial replacement of hydroxyl groups with a siloxy group, e.g. $(Al(OH)_3(OSi^-))^-$. For simplicity, this species will hereafter be known as $Al(OH)_x^-$. Increasing the temperature had a pronounced effect upon the broad tetrahedral Al, significantly reducing the respective peak area, as is clearly evident in Figure A4a. This is related to Curie's law that describes loss of spin magnetization and consequently signal intensity with increasing temperature.³⁶⁻³⁷ This reversible effect is less pronounced for the liquid $Al(OH)_x^-$ species, a consequence of the spins being in the more homogeneous environment of the liquid.

Deconvolution of both peaks, using Lorentzian/Gaussian line shapes (L/G = 1 and 0.6 kept constant, for $Al(OH)_x^-$ and $Al_{[Fr]}$, respectively), allowed for plotting the changes observed in the line width and relative peak area against the time and temperature, also shown in Figure 4 (b&c). The effect of crystallization on the chemical shift is reported in Figure A5a. At the end of the induction period one first observes the presence of XRD-crystalline material (Figure 1) due to the reorganization of the aluminosilicates germ nuclei leading to the energetically favorable formation of larger crystallites.³ We show here that the line width can also be considered an important parameter of zeolite crystallization describing the structural order of the probed Al (Figure 4b). The incorporation of Al into the framework, building consecutive shells of Al-O-Si leads to a minimization of the charge separation with the more homogeneously distributed charge leading to a narrower line width in the structurally more ordered network.¹¹ Within about eight hours of initiation the line width for the framework Al species has

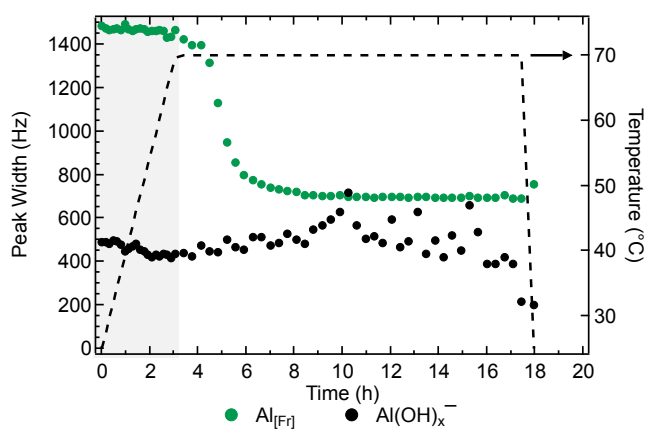
Chapter 2 – Formation of Faujasite Followed by in situ Spectroscopy

reached its minimum. Comparing the rate of crystallization via changes in the line-width and changes in the number of coherent planes (XRD Figure 1) shows the perfect agreement between both methods (Figure A5b).

a)



b)



c)

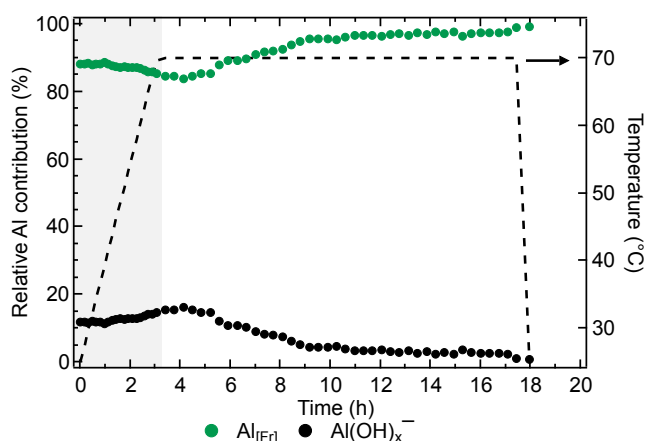


Figure 4. a) *In situ* ^{27}Al MAS NMR spectra showing the changes during the synthesis of FAU. The initial 3h also contains the heating period which is shown separately in Figure A4a. Spinning side bands are marked with an asterisk (*). De-convolution of the spectra (including the heating stage, shaded in grey) led to changes in the peak area (b) and line width (c) being observed for liquid $\text{Al}(\text{OH})_x^-$ and the solid tetrahedral Al ($\text{Al}_{[\text{Fri}]}$). Chemical shift changes are reported in Figure A5. Color-coding is reported in the legend.

At the same time, the liquid species experiences no significant changes in the line shape. Instead, its decreasing concentration shows the gradual consumption of the liquid species and incorporation into the framework (Figure 4c). This is in line with findings by Navrotsky et al. who observed a drop in the concentration of dissolved Al.¹³ Due to the reduced signal intensity, close to detection limit, the statistical error in assessing the line-width increases resulting in the spread of values observed at the later synthesis stage. Lastly, the change in the chemical shift (see Figure A5a) can also be attributed to the formation of a zeolite framework. Chemical shifts essentially contain information on the observed nuclei's electronegativity. A downfield shift to higher ppm indicates a more electronegative environment surrounding the nuclei, withdrawing electrons and thus decreasing the amount of shielding (the degree of which determines the observed chemical shift). This is the case for the tetrahedral framework Al, which experiences a shift from 60 ppm to 62 ppm (see Figure A5a), due to the increasing electronegativity of the growing Si-O framework.

Select samples obtained from the classical synthesis were also investigated with ^{27}Al MAS NMR, the plots shown in Figure A6. However, the solid particles first had to be separated from the liquid phase via centrifugation and were then washed with distilled water before being dried and characterized with the respective methods. As a result

Chapter 2 – Formation of Faujasite Followed by *in situ* Spectroscopy

only one species, the tetrahedral Al at 60 ppm, is observed, in agreement with the liquid species observed after centrifugation of the gel (Figure A4b). In line with *in situ* data, the line width and chemical shift change, reflecting a more ordered and crystalline product.

In situ ^{23}Na MAS NMR

Investigating the Al nucleus via XAFS showed that the Al environment is established during the aging period followed by a reorganization of the gel during the induction period (up to 3.75 h). ^{27}Al MAS NMR then showed the narrowing of the tetrahedral Al peak as the continuous attachment of aluminosilicate species resulted in the formation of the zeolite, as can be envisioned from a layer by layer growth model. As ^{27}Al MAS NMR was not sensitive enough to obtain information on a crystallization mechanism during the induction and rapid growth period, we investigated another element, namely ^{23}Na , with *in situ* MAS NMR spectroscopy. It is widely used in zeolite synthesis where it mainly terminates depolymerized Si-O⁻ chains in the gel, acts as a charge balance for the negative Al-O-Si framework, and in the case of FAU also behaves as the structure-directing agent.^{15, 38} Engelhardt et al. were able to distinguish the typical quadrupolar lineshapes of Na, observed in fully dehydrated samples, and attribute them to specific ion exchange sites (Figure 5).³⁵ In zeolite Y (Si/Al > 1.5), Na is typically located within the D6R (SI), close to the six-membered ring windows in the sodalite cage facing the D6R (SI') or the supercage (SII') as well as in the supercage (SII). In zeolite X (Si/Al < 1.5) additional cations can be found close to the 4-membered ring of the sodalite unit in the supercage (SIII).³⁵ Furthermore, the population density of Na in the various exchange sites depends on the chemical composition.³⁵ For example, the zeolite X investigated in this contribution (Si/Al 1.1) does not contain any Na in the D6R (SI).

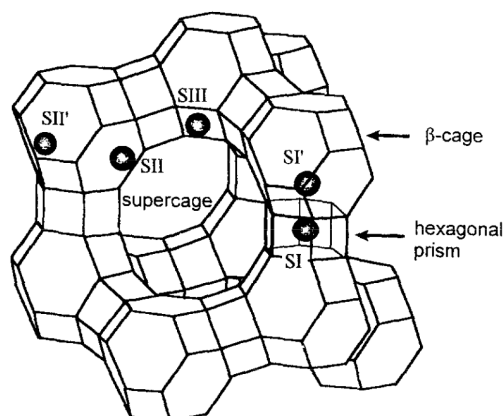
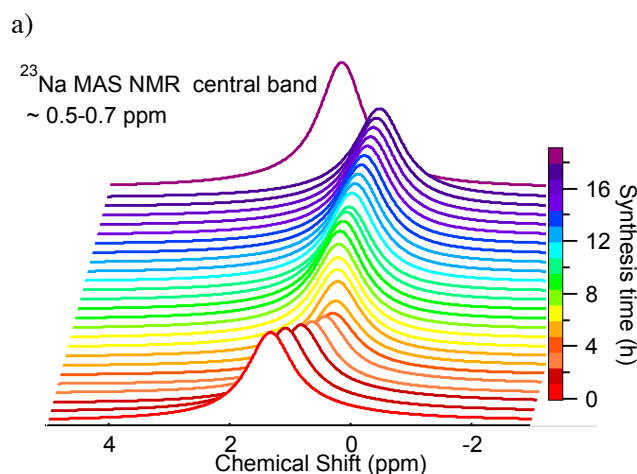


Figure 5. Identified cation positions occupied by Na⁺ in the fully crystalline FAU structure. Reprinted with permission from Feuerstein, M.; Hunger, M.; Engelhardt, G.; Amoureux, J. P. *Solid State Nucl. Magn. Reson.* **1996**, 7, 95-103.

With *in situ* ²³Na MAS NMR spectroscopy (Figure 6a), however, only one slightly asymmetric peak was observed (0.5 ppm). The hydration sphere surrounding Na in the case of aqueous systems or hydrated species results in a downfield shift of the peaks as well as narrowing of the peaks into a mostly symmetric Gaussian peak.³⁸⁻⁴⁰ The suppression of the typical quadrupolar line shapes by the hydration sphere results in a loss of information as individual exchange sites cannot be differentiated. Line fitting allowed us, however, to elucidate the presence of two peaks (Figure A7); The broad peak contributing to the asymmetry of the overall peak is indicative of a distorted species with higher quadrupolar coupling constant (QCC).^{34,38} We attribute it to Na



b)

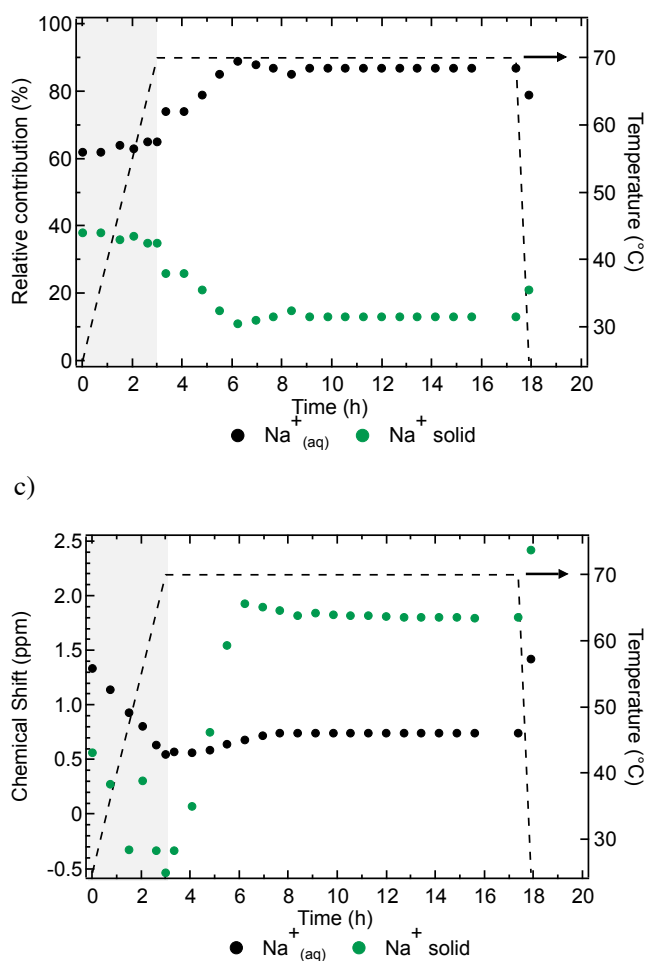


Figure 6. a) *In situ* ²³Na MAS NMR spectra collected during FAU synthesis. b) and c) show changes in the peak width and chemical shift for Na⁺_(aq) (black) and Na⁺ interacting with solids (green) during *in situ* ²³Na MAS NMR spectra respectively. Changes to the peak width are reported in Figure A10. The shaded area corresponds to the heating period.

interacting with the solid material in the gel. This would be the case for Na⁺ terminating Si-O⁻ in e.g. amorphous gel or Na⁺ within already formed pore structures. The narrow peak is assigned to octahedral-coordinated Na⁺ in aqueous phase resulting in the majority of the signal.³⁴ This assignment was confirmed by performing a varying pulse width experiment of the amorphous gel at room temperature which showed different maxima for the broad peak and narrow peak respectively. The longer pulse width required to maximize the narrow peak signal is due to its liquid nature, whereas solid materials typically have shorter pulse widths, as evident in Figure A8.

Chapter 2 – Formation of Faujasite Followed by *in situ* Spectroscopy

In line with the ^{27}Al MAS NMR experiment, the relative integrated areas and chemical shifts of the de-convoluted peaks were plotted against the synthesis time in Figure 6b & c. The changes in line width can be found in the Appendix (see Figure A10).

Heating the aged gel in the rotor reduced the signal intensity (Curie's law) and also had an impact on the chemical shift as the peaks shifted towards the negative edge of the spectrum (Figure A9). One can envision that increasing temperatures increase the mobility of the Na ions and thus affect their chemical environments relevant for the chemical shift. No further changes were detected until the end of the induction period (ca. 3.75h). As the crystallinity in the material increases (Figure 1) along with the narrowing of the Al line width (Figure 4b), the concentration of Na^+ in the aqueous phase increases whereas the Na^+ with a high QCC decreases (Figure 6b). Formation of the zeolite results in the formation of $-\text{Si}-\text{O}-\text{Al}-$ bonds from depolymerized Na^+ terminated $\text{Si}-\text{O}^-$ polyhedra. As a result, the concentration of this Na^+ species decreases, whereas $\text{Na}^+_{(\text{aq})}$ increases. Simultaneously to these changes, the broad peak experiences a downfield shift by several ppm, indicative of a more electronegative environment surrounding the ions, as is the case in a zeolite framework (Figure 6c). The line width of the broad peak also significantly narrows over the course of the synthesis, suggesting a more homogeneous environment of the Na cations (Figure A10). Note that the changing line-width and chemical shift are in line with changes observed via ^{27}Al MAS NMR, where it was attributed to crystallization and formation of the zeolite. We postulate the broad peak to be a superposition of several Na^+ species associated with solid material.

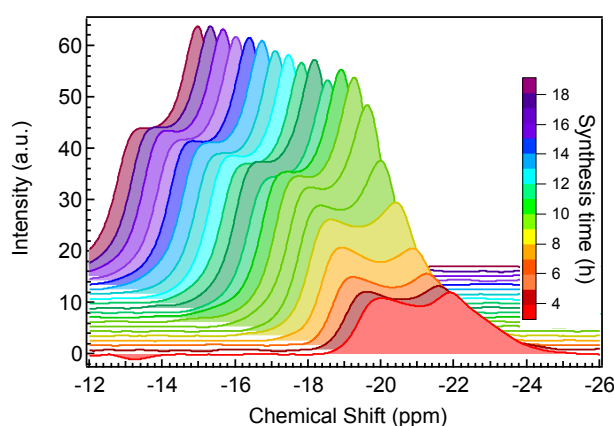
This is further corroborated when characterizing the hydrated, *ex situ* samples with ^{23}Na MAS NMR (Figure A11a). Only Na linked to solid material is observed. Clearly, Figure A11a shows the presence of at least 2 species, one at 5 ppm and the other at -7 ppm, with a shoulder at -15 ppm indicating the possible presence of another species. Additionally, select samples were also investigated in their dehydrated state presenting significantly broadened peaks (Figure A11b). Broadening is especially pronounced for zeolite X after 20 hours, whereas only one Gaussian line is observed in the hydrated spectrum (Figure A11a). The experimental ^{23}Na spectrum obtained for the final *ex situ* sample agrees well with that reported for zeolite X by Engelhardt et al. (Figure A12).³⁵ This led us to conclude that both materials have a similar exchange site distribution.³⁵

Chapter 2 – Formation of Faujasite Followed by *in situ* Spectroscopy

The spectra of the initial dried gel, on the other hand, shows only minor differences between hydrated and dehydrated states (Figure A11). This suggests that the Na species involved are more symmetric with a lower quadrupolar coupling constant. The narrow, symmetric peak at 5 ppm is gradually consumed and disappears after 6-7 hours. We attribute this peak to sodium silicate also observed with XRD, which disappears at a similar rate.

An advantage of the reported *in situ* MAS-NMR approach is spinning the rotor at high frequencies to significantly reduce quadrupolar line broadening. Typically, only rotating solids have spinning side bands, a consequence of the inhomogeneity of the material, in contrast to liquid samples where all spins are equally relaxed and distributed. Consequently, part of the signal is lost from the central isotropic band and moved equally up- and downfield by the spinning frequency. This differentiation between liquid and solid species allows us to more closely investigate the latter, present in the synthesis gel. In Figure 7 we now report the observation of a spinning side band resolved into two peaks for the ^{23}Na MAS NMR experiment at ca. -22 ppm. Correcting by the spinning frequency (3 kHz) puts these peaks close to 0 ppm. The marginal intensity is in agreement with the excess of $\text{Na}^+_{(\text{aq})}$ used in the gel. By the end of the synthesis the intensity more than doubled due to the increasing contribution of crystalline solid. The improved resolution of these peaks can be attributed to satellite transitions.⁴¹ They enable resolving the side band into two peaks, one at -22 ppm (high-field), the other at -20 ppm (low-field). Spectra of quadrupole nuclei are typically dominated by the central band of the central transition ($1/2$ to $-1/2$). However, it is also possible for spins from electronic states $\pm 1/2$ to be excited to $\pm 3/2$, known as

a)



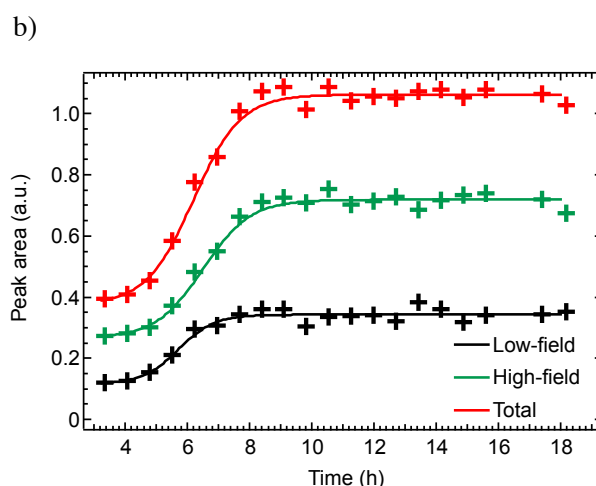


Figure 7. Showing the changes of the spinning side band associated with solid Na^+ material as a function of the synthesis time. The initial heating period is not reported (see Figure A13). Changes in the peak area were obtained by deconvolution of the peaks, see also Figure A14 for additional trends (chemical shift and peak width). A high-field and low-field peak were identified at -22 and -20 ppm respectively. Color-coding is reported in the legend.

a satellite transition. These transitions, besides being of lower intensity, can also have a significantly improved resolution, as well as an inverse lineshape.⁴¹ In the present experiment, the two peaks therefore represent at least two separate species of Na cations in solid environments. From fitting the peaks with Gaussian line shapes (Figure A13b) we can once more extract information on peak areas (seen in Figure 7b) as well as chemical environments, seen in Figure A14a & b. As can be seen, the overall intensity increases in the isothermal stage as the zeolite is formed.

However, the growth of the individual species proceeds at different rates. The low field peak reaches completion before the high-field peak, suggesting the preferential formation of the former species.

While we do not have any evidence for the discrete presence of these proposed species, we suggest, based on the work by Melchior, who suggested that FAU is formed via ordered sub-units,⁴² the following assignment; The peak at -20 ppm is attributed to Na^+ in sodalite cage type environment, e.g. in SI' and SII' sites. The peak at -22 ppm is then assigned to Na^+ in the FAU supercage, e.g. SII and SIII sites. Once a critical mass of sodalite cage-like structures are obtained, the FAU superstructure can be formed. Incidentally, the chemical composition of the final material excludes the

Chapter 2 – Formation of Faujasite Followed by *in situ* Spectroscopy

presence of Na⁺ in D6R, thus preventing us from observing a semblance of this species *in situ*. As the synthesis progresses and the structural order increases, the – 22 ppm peak significantly narrows. The peak at – 20 ppm, on the other hand does not change in line-width. Interestingly, the distribution between Na⁺ in the supercage (– 22 ppm) and Na⁺ in the sodalite cage (– 20 ppm) is ~70:30. This is in agreement with the population study conducted by Engelhardt et al. showing a combined population of 67 Na/u.c. in SII and SIII sites and 24 Na/u. c. in SI' respectively.³⁵ For the 96 atoms in the FAU unit cell this corresponds to a 70:30 ratio.

It should be mentioned that the dense synthesis gel can significantly hinder effective shimming, used to homogenize the spins, thus creating sidebands associated with the liquid species. To verify that the observed spinning side bands are due to rotational solids only, we performed an additional *in situ* experiment on a spectrometer of lower magnetic field strength, which allowed us to improve the shimming quality. The resulting presence and progression of the spinning side bands shown in Figure A15 clearly shows the trend to be independent of field strength thus confirming their solid nature.

An important caveat is the inadequacy of the employed techniques ability to assess the requirement of a fully formed sodalite cage prior to the growth of the FAU supercage. We tend to exclude this requirement as it would lead to a formation mechanism involving the clicking of several sodalite units into supercage structures which we consider to be entropically challenging. Instead the growth of the complex structure is merely structurally directed by the different Na⁺ environments.

Zeolite Formation

Zeolite crystallization mechanisms consist of several phases.³ The findings of the experiments described herein allow us to develop a reaction network and interpret the stages of zeolite formation. During the aging process, most SiO₂ particles in the Si-sol are depolymerized by the presence of hydroxide anions, leading to gelling upon mixing with the Al-sol. The Al-sol consists solely of Al(OH)₄⁻ which reacts rapidly with depolymerized SiO₂ forming a solid-like aluminosilicate gel. This amorphous solid phase is then continuously depolymerized and repolymerized by hydroxide ions.^{6,9} This aged and amorphous gel approaches a more equilibrated state with the liquid phase

Chapter 2 – Formation of Faujasite Followed by *in situ* Spectroscopy

by increasing the temperature and time and organized aluminosilicates precursor species are formed.^{3, 25} Navrotsky et al. observed associated this behavior with an endothermic dissolution process.¹³ This equilibration step is also highlighted by our findings with *in situ* Al XAFS experiments. The already aged gel was placed in the XAFS cell and was then heated up to reaction temperature. During this process, a slight distortion of the Al-O tetrahedron as seen by the pre-edge peak in the XANES (Figure 1a) signals the rearrangement of the amorphous aluminosilicates into a short-range ordered, equilibrated gel. At the same time the EXAFS part in Figure 3 shows that within 4.5 Å the Al coordination does not change. Neither, MAS-NMR nor X-ray diffraction show any changes during this induction period.

By continuous polymerization and depolymerization these aluminosilicates nuclei eventually reach a critical size at which point crystal growth and propagation of the nuclei is energetically feasible, ending the induction period.⁴³⁻⁴⁴ *In situ* MAS NMR experiments are very sensitive to subtle changes during this stage of the synthesis and their rates of change as assessed by ²⁷Al and ²³Na MAS NMR can be compared, as seen in Figure 8. It should be noted that only changes observed during the isothermal stage are reported in Figure 8, as the mostly reversible temperature-induced changes cannot be clearly quantified and are therefore assumed to be equal to zero (initial 3h). Furthermore, all changes, whether positive or negative, are translated into a conversion equivalent unit to easily compare individual species. Prior to crystallization, which can be followed by the narrowing line width of the Al peak at 60 ppm, Na⁺ interacting with solid, e.g. charge balancing amorphous aluminosilicate gel and SiO₂ polymer, is released (red line in Figure 8). This suggests that it is the availability of depolymerized (SiO)_x-SiO⁻ that limits the rate of crystallization. SiO⁻ units then condense with Al(OH)_x⁻ readily available, and are incorporated into the forming zeolite, as the concentration of Na⁺ in the aqueous phase is increased.

As the zeolite is formed and the crystallinity increases, the environment of the negative charge changes. Initially, the negative charge was localized on Al(OH)_x⁻ as well as terminating amorphous silica. In both cases Na⁺ acted as a charge balance. With the assembly of the zeolite framework and the geometric arrangement of the individual building units into sub-units (e.g. sodalite cages, D6R), the negative framework charge is distributed over several nearby atoms.

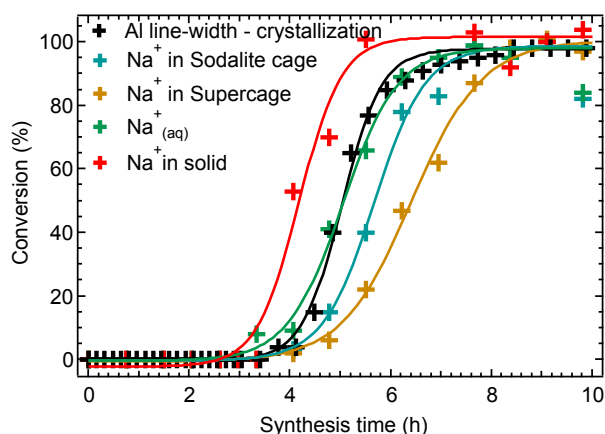


Figure 8. Plotting the changes in Al line width (black), Na exchange position (yellow and turquoise) as well as aqueous Na⁺ ions (green) against the synthesis time allows for a direct comparison of rates of structural change. In addition, the transformation of Na⁺ interacting with solid material (red) as evidenced by changing chemical shifts is plotted. Changes during the heating period were set to 0 as those are solely due to changes in temperature.

In order to balance the charge of the thus generated surfaces, the Na cations now need to occupy certain locations such as those in the sodalite units (SI' & SII') and supercages (SIII & SII) as well as D6R subunits (SI). Therefore we now see an increase in the contribution of first, Na⁺ in the sodalite cage type environments (i.e. SI' and SII' sites) and then after a certain number of sodalite units are formed, Na⁺ in the supercage (i.e. SII and SIII exchange sites) increases. Most of these changes are completed within 8 hours of initiation. At the same time, the long-range order as assessed *ex situ* by XRD is at 85% completion. This shows that *in situ* spectroscopy methods such MAS-NMR and XAFS are more sensitive to the changes directing the growth of the zeolite.

While the reported methods were not sensitive enough to distinctively observe D6R subunits (no Na⁺ occupies the D6R), the changes observed in the spinning side bands with ²³Na MAS NMR inferring the formation of the supercage after that of the sodalite cages, strongly supports the mechanism proposed by Melchior.⁴² However, it is also possible for the D6R units to be formed initially, with the subsequent formation of sodalite and supercage structures, as was proposed by Melchior in a later contribution that covered a wider range of synthesized FAU compositions.²⁰ In this instance, the delay between the onset of crystallinity (black line in Figure 8) and the changes occurring in the Na exchange site can be attributed to the formation of D6R, free of Na⁺ cations and thus invisible in ²³Na MAS NMR.

Chapter 2 – Formation of Faujasite Followed by in situ Spectroscopy

Macroscopically, the crystalline growth period can be described by a layer-by-layer growth model, where a viable nucleus is adsorbed onto the growing zeolite crystal consequently generating a kink site with high surface energy promoting addition of further growth units.^{24,45} At the same time the speciation of the Na⁺ charge directs the growth mechanism via the various sub units.

Chapter 2 – Formation of Faujasite Followed by *in situ* Spectroscopy

CONCLUSION

A combination of several *in situ* characterization techniques in addition to a classical *ex situ* analysis of the crystallization kinetics of faujasite has shown the necessity of cross-referencing across scales. XANES enabled the observation of gel equilibration during the induction period, while Al-EXAFS, sensitive over a few nanometers, implies a preordained Al geometry determined during the aging period. The increased structural order of forming zeolites can be observed at tens of nanometers (MAS-NMR) as well as *ex situ* with X-ray diffraction.

Thus, a mechanism was postulated based on the structure directing effect of Na⁺, where the speciation between different Na⁺ environments affects the formation of the zeolite as assessed by the varying formation rates of the Na⁺ environments (MAS-NMR). This is consistent with the idea of ordered sub-units directing the formation of the FAU zeolite.

Chapter 2 – Formation of Faujasite Followed by in situ Spectroscopy

ACKNOWLEDGMENT

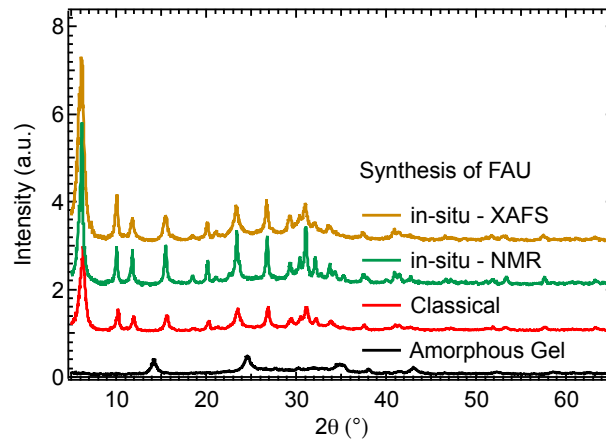
T. Huthwelker is acknowledged for assistance with XAFS experiment setup at the Swiss Light Source (PSI, Switzerland). Further, V. Shutthanandan and B.W. Arey are acknowledged for performing Helium ion microscopy as well as Z. Zhao, N.R. Jaeger, M. Weng, C. Wan and M. Hu for aiding in the NMR experimental procedure. T. Varga is acknowledged for his help with the capillary XRD. This work was supported by the US Department of Energy, Office of Science, Office of Basic Energy Sciences and by the Materials Synthesis and Simulation Across Scales (MS³ Initiative) conducted under Laboratory Directed Research & Development Program at PNNL. The *in situ* NMR experiments were supported by the U. S. Department of Energy (DOE), Office of Basic Energy Sciences, Division of Chemical Sciences, Biosciences and Geosciences. Part of the research described in this paper was performed in the Environmental Molecular Sciences Laboratory (EMSL), a national scientific user facility sponsored by the DOE's Office of Biological and Environmental Research and located at Pacific Northwest National Laboratory (PNNL). PNNL is operated for the US DOE by Battelle.

Chapter 2 – Formation of Faujasite Followed by in situ Spectroscopy

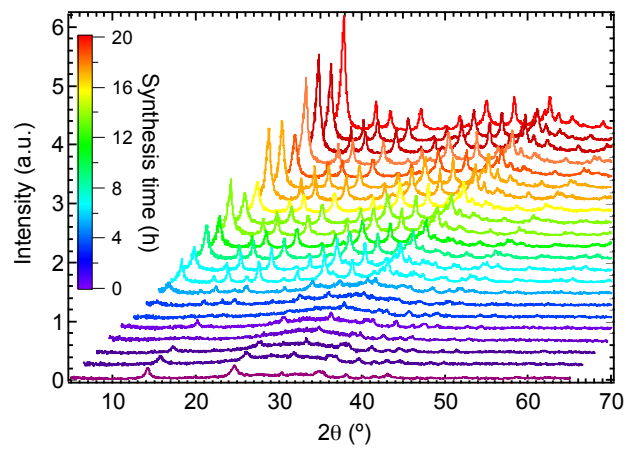
APPENDIX

X-ray diffraction

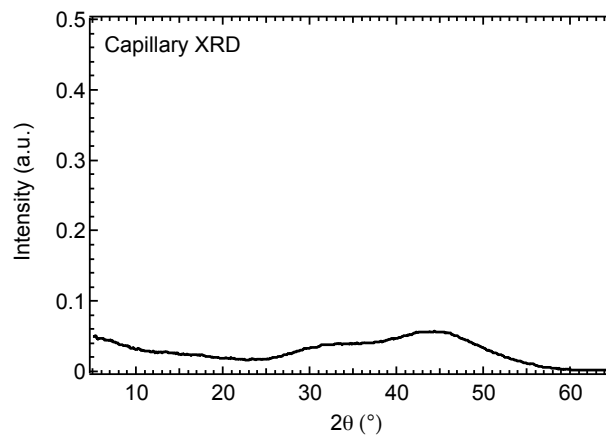
a)



b)



c)



Chapter 2 – Formation of Faujasite Followed by in situ Spectroscopy

Figure A1. a) X-ray diffraction patterns obtained for FAU synthesized in an NMR rotor, XAFS cell and with the classical approach. In comparison the pattern for the mostly amorphous gel is shown as well. b) On the right the gradual transformation into FAU can be seen, used to determine the kinetics of crystallization seen in Figure 1 of the main text. c) XRD pattern for the amorphous gel obtained in a capillary without any workup procedure. Only amorphous SiO₂ is present indicating that the diffraction pattern in the amorphous gel in Figure 1Sa is due to the workup procedure of the *ex situ* analysis.

He Ion Microscopy

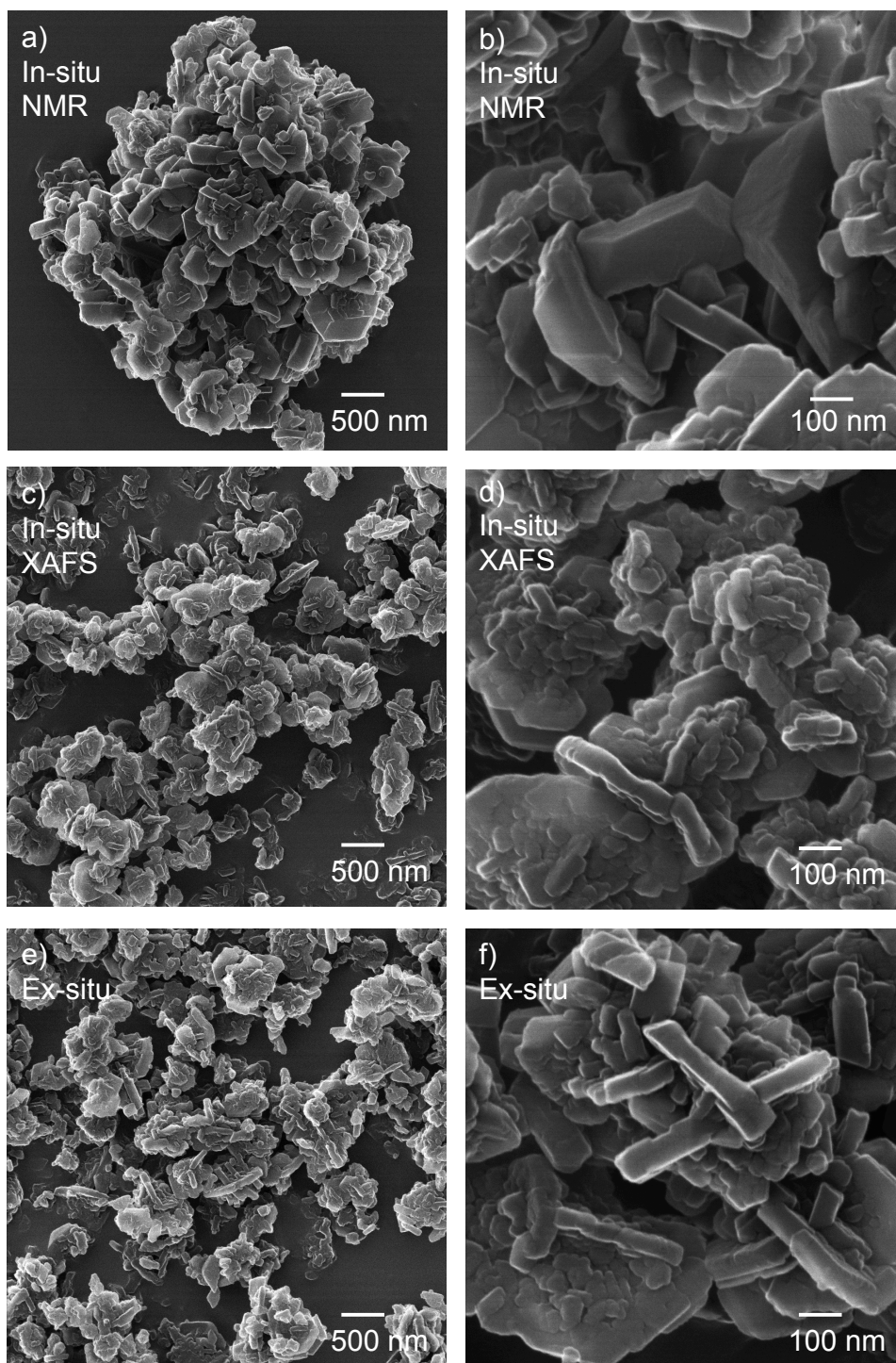


Figure A2. He ion micrographs of zeolite X obtained via the *in situ* NMR (a&b), *in situ* XAFS (c&d) as well as classical *ex situ* (e&f) synthesis.

Chapter 2 – Formation of Faujasite Followed by *in situ* Spectroscopy

X-ray absorption fine structure (XAFS)

Cell design

The Al K-edge XAFS measurements were performed in fluorescence mode as an operando measurement using a ramp rate of 0.1 °C/min. The maximum design temperature of the cell is 500 °C. The sample is initially loaded into the cell by injection of the gel precursor solution via a syringe. The x-ray window consisted of a 200 nm thick Si₃N₄ window having an aperture of 1.5 x 1.5 mm that was supported on a silicon frame (Norcada Inc.) These windows were affixed to the stainless-steel support using a high-temperature silicone-based adhesive (Vacseal) in an unsupported area-type seal design. The cell is shown in Figure A3.

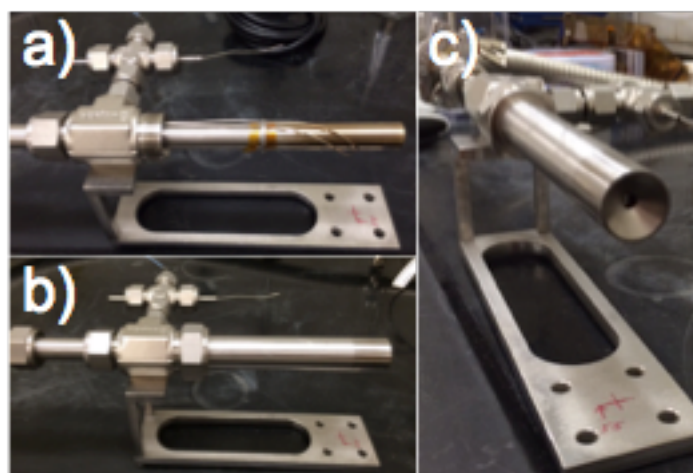


Figure A3. The *in situ* XAFS cell is shown: a) the setup with removed cover exposing the heated tip where the gel is injected as the gas inlet and outlet lines used to prevent over-pressurization; note that a rubber O-ring (not shown) is used to seal the compartment at the steel O-ring; b) the cell with the cover mounted; c) The aperture for the X-ray beam is shown with the window removed. The sample gel is placed on the heated element such that it completely fills the aperture.

Nuclear Magnetic Resonance

In situ ^{27}Al MAS NMR

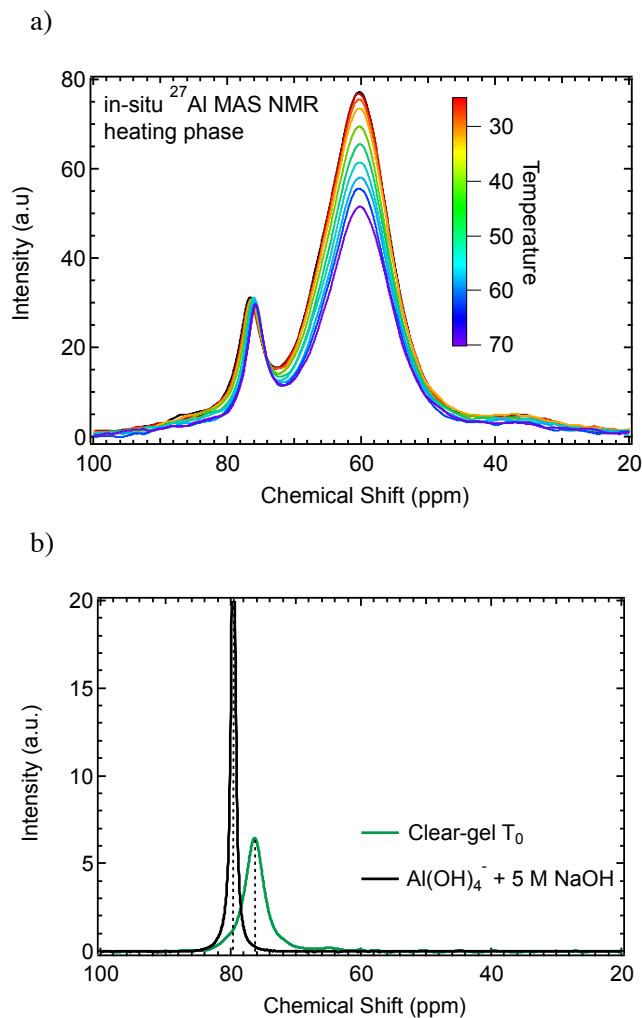


Figure A4. a) ^{27}Al MAS NMR spectra obtained during the heating phase of the *in situ* measurement. Decreasing intensity observed for the broad tetrahedral peak (60 ppm) as the temperature increases. b) To identify the nature of the peak 76 ppm several samples were investigated. Al(OH) $_4^-$ in a 5 M NaOH solution representing the alkaline conditions of the experiment appears at 80 ppm (black). Separation of the gel at T $_0$ with a centrifuge and subsequent analysis of the supernatant solution gives a peak at 76 ppm (green).

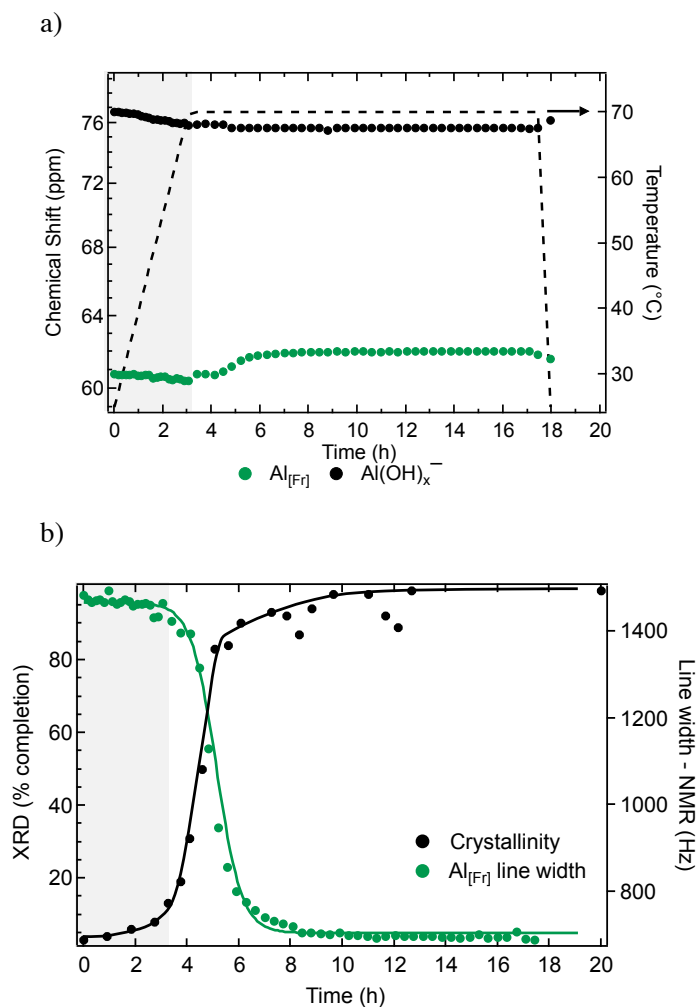


Figure A5. (a) Changes observed in the chemical shift of the dissolved $\text{Al}(\text{OH})_4^-$ species as well as the solid tetrahedral Al ($\text{Al}_{[\text{Fv}]}$) species. (b) Comparing the rate of formation, assessed by XRD as well as changing line-width of the solid $\text{Al}_{[\text{Fv}]}$ peak shows the relation between *ex situ* and *in situ* approaches. The changing line-width is a measure of the structural order in the forming zeolite.

Ex situ characterization

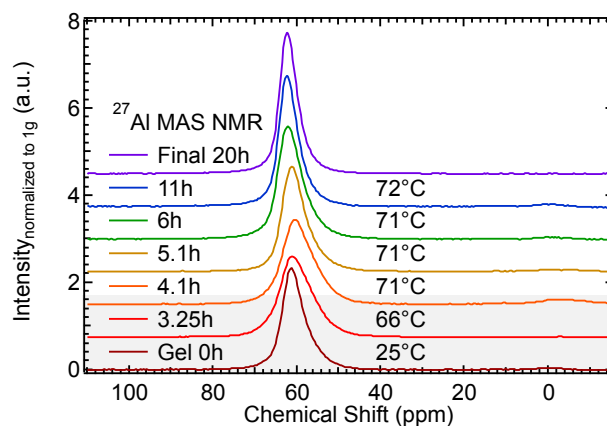
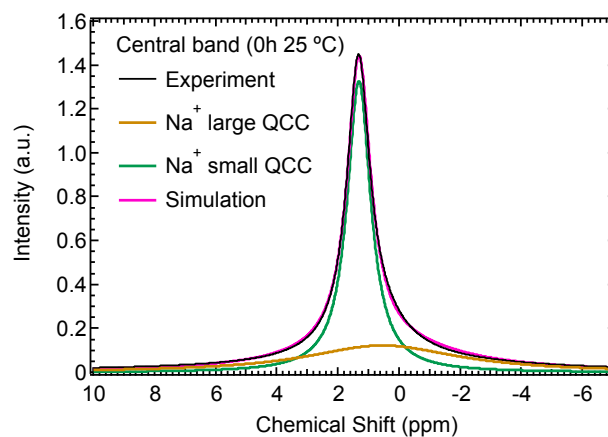


Figure A6. ^{27}Al MAS NMR spectra taken *ex situ* in hydrated conditions for materials obtained at specific times during the classical synthesis as well as the final product. Color-coding is explained in the legend. Highlighted in gray are the measurements performed on samples that had yet to reach the final synthesis temperature of 70 °C.

Chapter 2 – Formation of Faujasite Followed by *in situ* Spectroscopy

In situ ^{23}Na MAS NMR

a)



b)

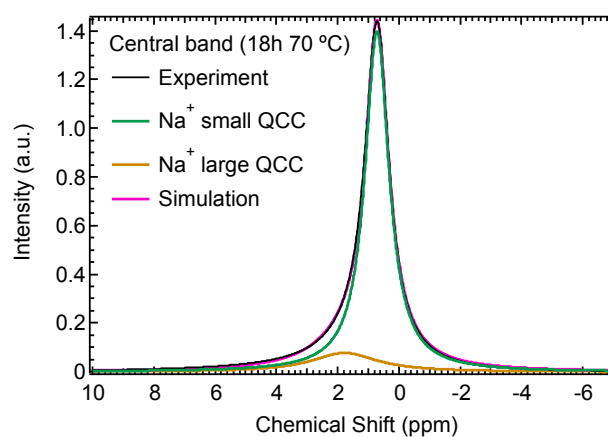


Figure A7. The central band can be simulated with Lorentzian/Gaussian (L/G \sim 0.5) lineshapes, once shown for the initial spectra at the start of synthesis (a) and the final spectra obtained (b). The quadrupolar line shapes typically observed in dehydrated states are suppressed by the aqueous environment.

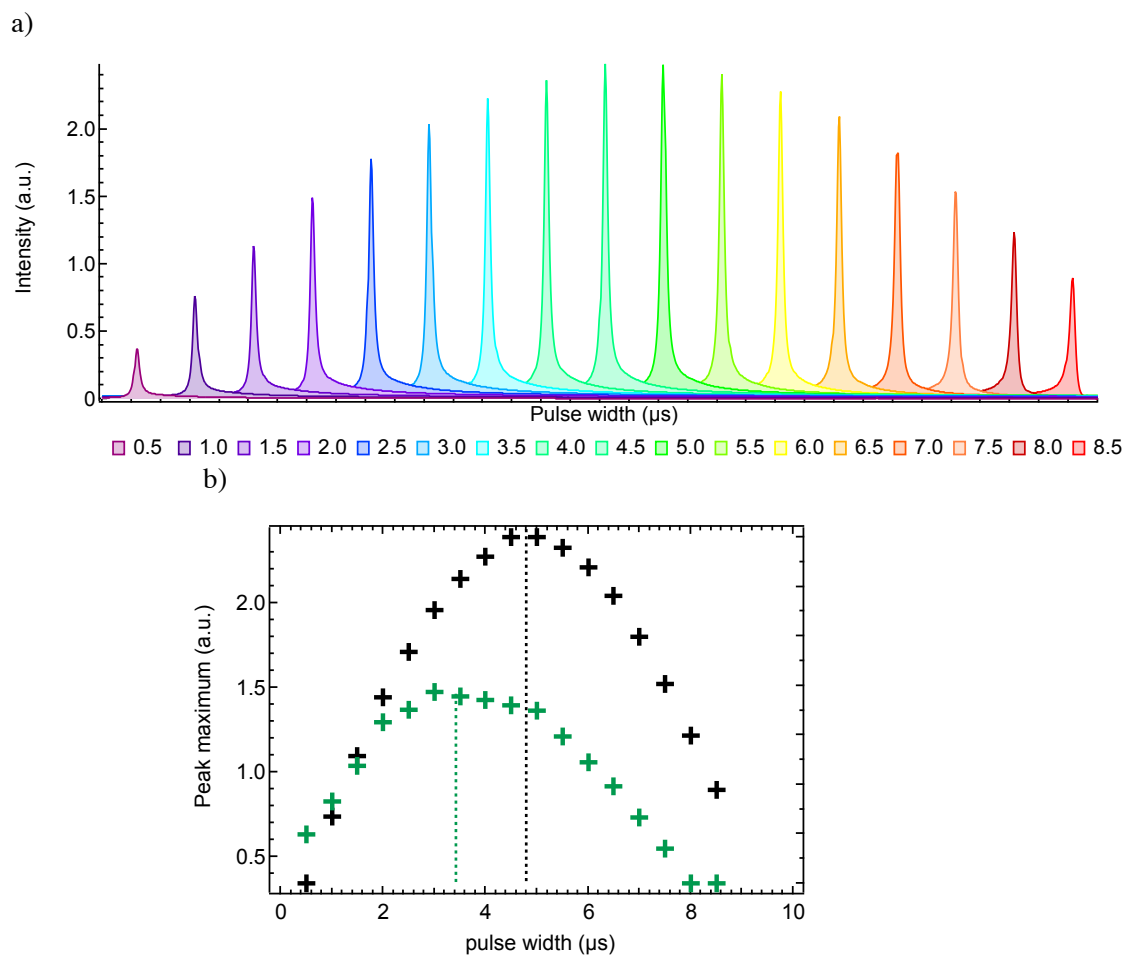


Figure A8. a) A pulse width array for the $\pi/2$ excitation shows a peak maximum close to $5 \mu\text{s}$ for the liquid narrow peak in the initial amorphous gel at room temperature. b) Deconvoluting the spectrum identifies the peak maximum associated with the broad peak close to $3 \mu\text{s}$ (green line). This is attributed to the solid nature of this peak which results in shorter pulse widths.

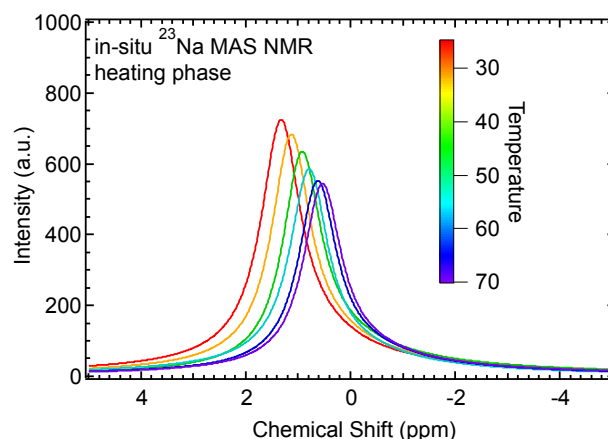


Figure A9. Effect of heating on the intensity and resolution of peaks observed with ^{23}Na MAS NMR during *in situ* measurements. On the left is the central band associated mainly with $\text{Na}^+_{(\text{aq})}$, on the right the corresponding spinning side bands due to the forming zeolite. The sideband peak at -22 ppm resolves at higher temperatures.

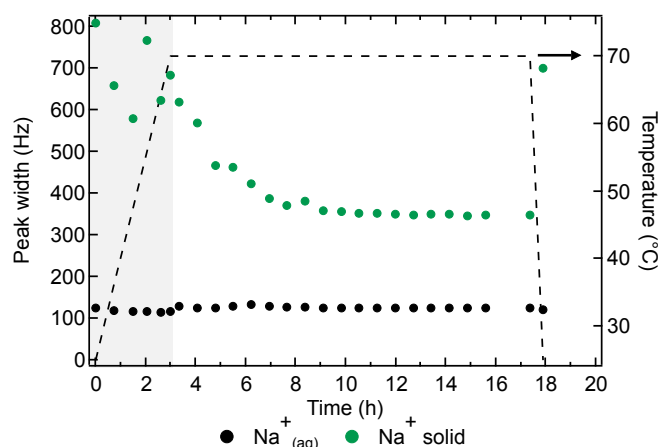


Figure A10. Observed changes in the line width of the central band observed close to 0 ppm (see also Figure 6 and Figure A9) during *in situ* ^{23}Na MAS NMR measurements. Two species, one broad with a large quadrupolar coupling constant (QCC) and one with a small QCC are being observed. The former is associated with Na ions interacting with solid (green) whereas the latter corresponds to $\text{Na}^+_{(\text{aq})}$ species (black). Color-coding is explained in the legend. The shaded area corresponds to the heating period, during which changes in the spectral parameters are affected mostly by temperature effects, rather than structural effects.

Ex situ characterization

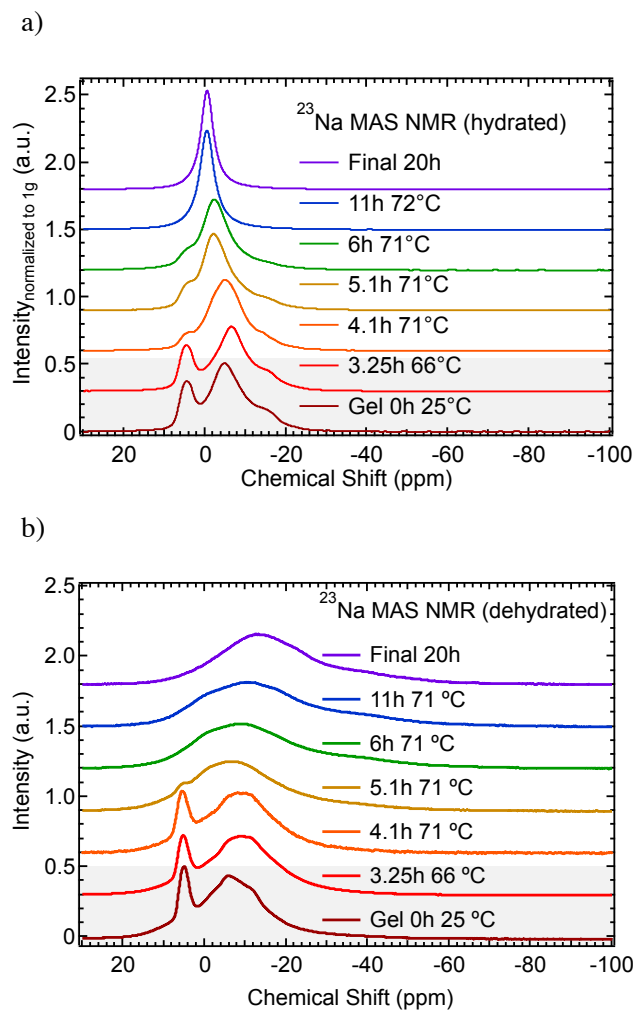


Figure A11. (a): ^{23}Na MAS NMR spectra taken *ex situ* in hydrated conditions for materials obtained at specific times during the classical synthesis as well as the final products obtained with *in situ* measurements and the classical approach. (b): A series of samples obtained via the classical approach, examined with ^{23}Na MAS NMR under dehydrated conditions. The spectra were obtained with a Bruker 600 MHz spectrometer. Color-coding is explained in the legend. The shaded area corresponds to measurements of samples obtained during the heating stage of the synthesis.

Chapter 2 – Formation of Faujasite Followed by in situ Spectroscopy

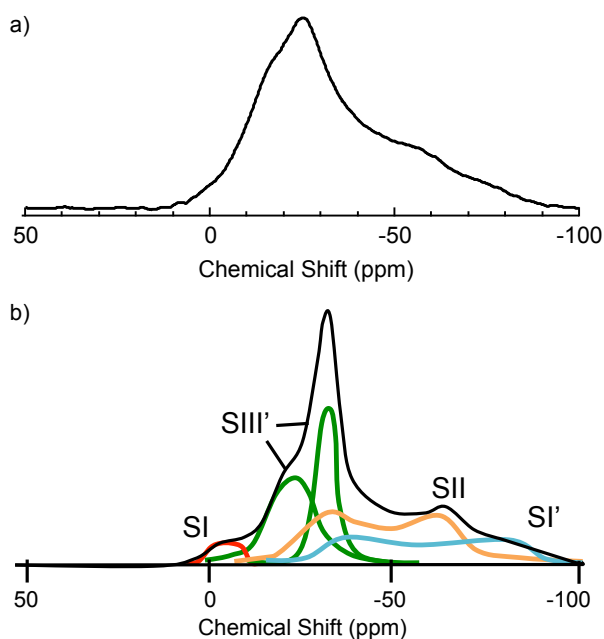


Figure A12. (a) the experimental spectrum of Na environments of zeolite X obtained through the reported synthesis are seen. The spectra were collected on a Bruker 500 MHz spectrometer to reproduce the same field strength as shown for the simulated spectra in (b), determining Na siting by Engelhardt et al. (Feuerstein, M.; Hunger, M.; Engelhardt, G.; Amoureux, J. P. *Solid State Nucl. Magn. Reson.* **1996**, 7, 95-103.). The reference spectrum (b) agrees well with the experimental spectrum obtained at the same field strength (a). Comparison of both spectra allowed us to conclude that Na cations populate similar sites in the final products of our synthesis.

Spinning side bands

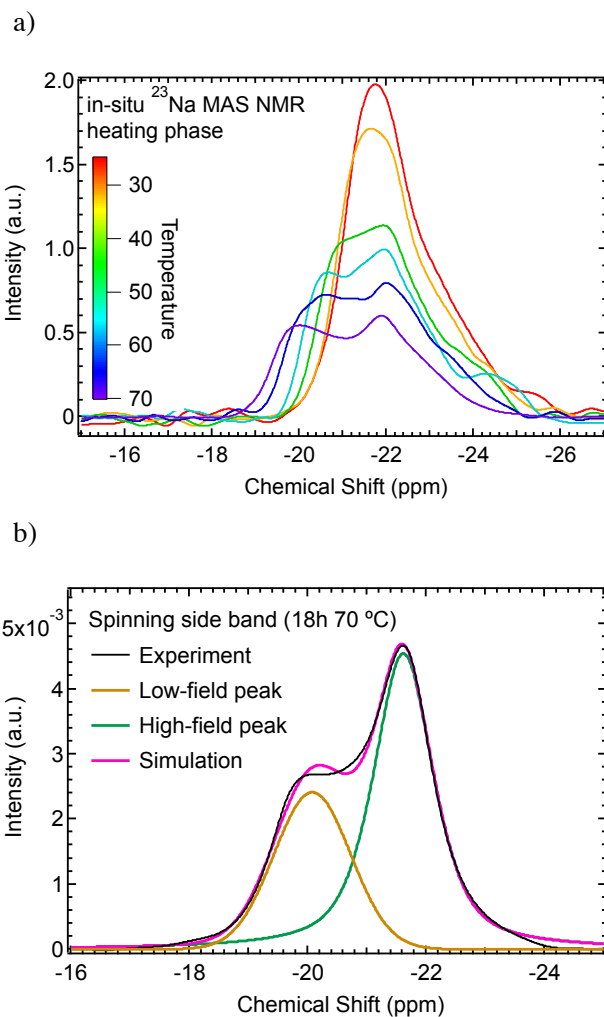
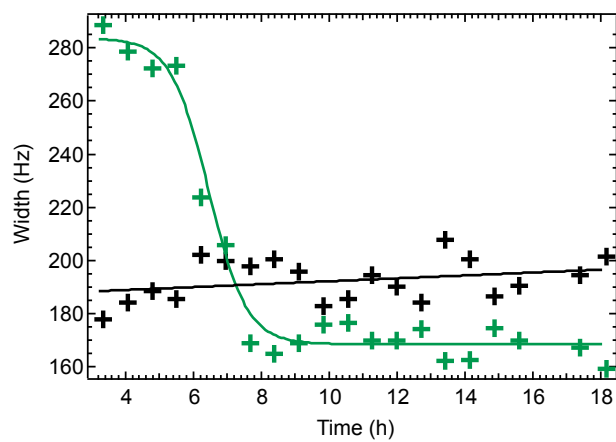


Figure A13. (a) Shows the temperature induced changes during the heating stage affecting the spinning side bands. They become resolved at elevated temperatures. (b) An example of the simulation of the spinning side bands observed during *in situ* ^{23}Na MAS NMR is shown. The low-field peak at -20 ppm corresponds to Na^+ in sodalite cages (e.g. SI' and SII'), whereas the high-field peak is attributed to Na^+ in FAU supercages (e.g. SII and SIII).

a)



b)

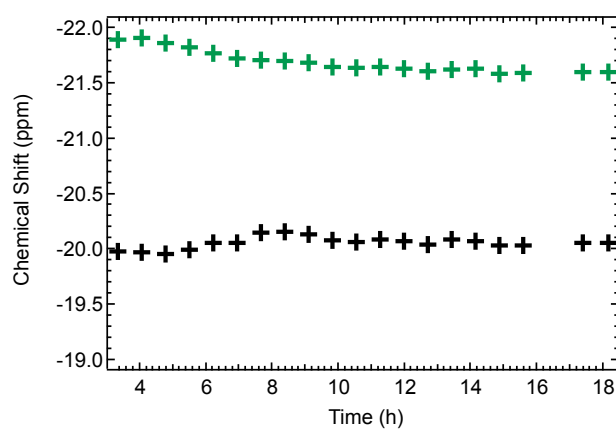


Figure A14. When simulating the spinning side band (Figure A12) with two Gaussian peaks, changes in the peak width (a) as well as chemical shift (b) can be observed, seen here. The peak area change is reported in the main text (Figure 7b).

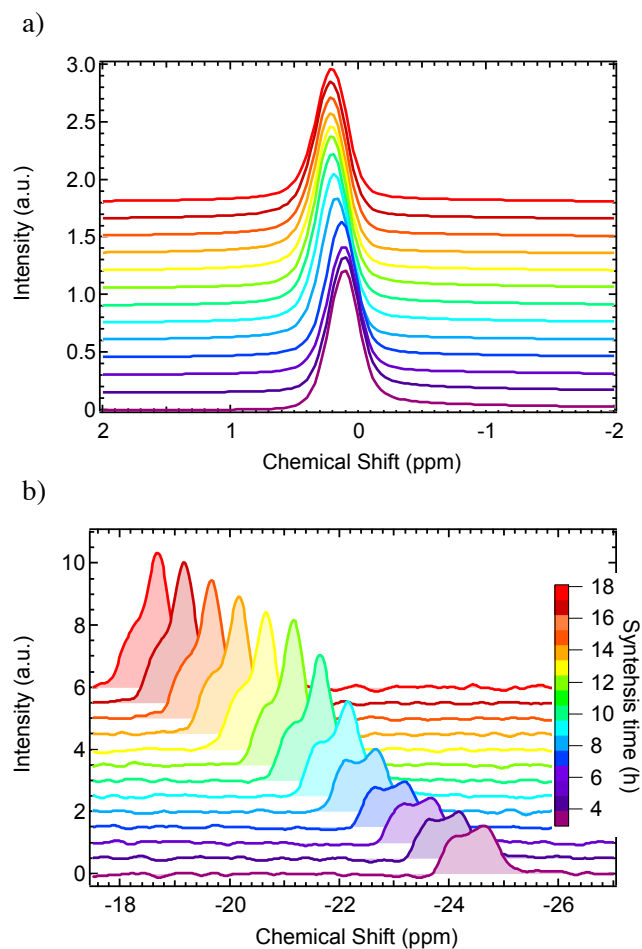


Figure A15. a) *in situ* ^{23}Na MAS NMR spectra measured on a 300 MHz spectrometer showing the central band. The peaks shift to slightly higher chemical shifts with increasing synthesis time. b) The spinning side bands are clearly present in at different fields. The increase in intensity is in line with the changes observed on the 500 MHz spectrometer (Figure 7).

Chapter 2 – Formation of Faujasite Followed by *in situ* Spectroscopy

ABBREVIATIONS

XAFS, X-ray Absorption Fine Structure; XANES, X-ray Absorption Near Edge Structure; EXAFS, Extended X-ray Absorption Fine Structure; MAS, Magic Angle Spinning; NMR, Nuclear Magnetic Resonance; XRD, X-Ray Diffraction.

REFERENCES

1. Barrer, R. M. *Berichte der Bunsengesellschaft für physikalische Chemie* 1965, 69 (9-10), 786-802.
2. Barrer, R. M. *Zeolites* 1981, 1 (3), 130-140.
3. Cundy, C. S.; Cox, P. A. *Microporous Mesoporous Mater.* 2005, 82 (1-2), 1-78.
4. Cundy, C. S.; Cox, P. A. *Chem. Rev.* 2003, 103 (3), 663-702.
5. Barrer, R. M.; Baynham, J. W.; Bultitude, F. W.; Meier, W. M. *Journal of the Chemical Society (Resumed)* 1959, (0), 195-208.
6. Kerr, G. T. *J. Phys. Chem.* 1966, 70 (4), 1047-1050.
7. Zhdanov, S. P., Some Problems of Zeolite Crystallization. In *Molecular Sieve Zeolites-I*, American Chemical Society: 1974; Vol. 101, pp 20-43.
8. Breck, D. W. *J. Chem. Educ.* 1964, 41 (12), 678.
9. Flanigen, E. M., A Review and New Perspectives in Zeolite Crystallization. In *Molecular Sieves*, American Chemical Society: 1973; Vol. 121, pp 119-139.
10. Guth, J. L.; Kessler, H., In *Catalysis and Zeolites*, Weitkamp, J.; Puppe, L., Eds. Springer-Verlag: Berlin, 1999; p 1.
11. Shi, J.; Anderson, M. W.; Carr, S. W. *Chem. Mater.* 1996, 8 (2), 369-375.
12. Valchev, V. P.; Bozhilov, K. N. *J. Phys. Chem. B* 2004, 108 (40), 15587-15598.
13. Yang, S.; Navrotsky, A.; Phillips, B. L. *Microporous Mesoporous Mater.* 2001, 46 (2-3), 137-151.
14. Baerlocher, C.; McCusker, L. B. *Database of Zeolite Structures*. <http://www.iza-structure.org/databases/> (accessed October 2016).
15. Frising, T.; Leflaive, P. *Microporous Mesoporous Mater.* 2008, 114 (1-3), 27-63.
16. Ramdas, S.; Thomas, J. M.; Klinowski, J.; Fyfe, C. A.; Hartman, J. S. *Nature* 1981, 292 (5820), 228-230.
17. Klinowski, J.; Thomas, J. M.; Audier, M.; Vasudevan, S.; Fyfe, C. A.; Hartman, J. S. *J. Chem. Soc., Chem. Commun.* 1981, (11), 570-571.

Chapter 2 – Formation of Faujasite Followed by in situ Spectroscopy

18. Engelhardt, G.; Lippmaa, E.; Magi, M. J. Chem. Soc., Chem. Commun. 1981, (14), 712-713.
19. Melchior, M. T.; Vaughan, D. E. W.; Jacobson, A. J. J. Am. Chem. Soc. 1982, 104 (18), 4859-4864.
20. Melchior, M. T.; Vaughan, D. E. W.; Pictroski, C. F. J. Phys. Chem. 1995, 99 (16), 6128-6144.
21. Hu, J. Z.; Hu, M. Y.; Zhao, Z.; Xu, S.; Vjunov, A.; Shi, H.; Camaioni, D. M.; Peden, C. H. F.; Lercher, J. A. Chem. Commun. 2015, 51 (70), 13458-13461.
22. Ravel, B.; Newville, M. Journal of Synchrotron Radiation 2005, 12 (4), 537-541.
23. Newville, M. Journal of Synchrotron Radiation 2001, 8 (2), 322-324.
24. Cundy, C. S., Synthesis of zeolites and zeotypes. In Stud. Surf. Sci. Catal., Čejka, J.; Bekkum, H. v., Eds. Elsevier: 2005; Vol. 157, pp 65-90.
25. Feijen, E. J. P.; Martens, J. A.; Jacobs, P. A., Hydrothermal Zeolite Synthesis. In Preparation of Solid Catalysts, G. Ertl; H. Knözinger; Weitkamp, J., Eds. Wiley-VCH Verlag GmbH: 2008; pp 262-284.
26. Coudurier, G.; Naccache, C.; Vedrine, J. C. J. Chem. Soc., Chem. Commun. 1982, (24), 1413-1415.
27. Jacobs, P. A.; Derouane, E. G.; Weitkamp, J. J. Chem. Soc., Chem. Commun. 1981, (12), 591-593.
28. van Bokhoven, J. A.; Sambe, H.; Ramaker, D. E.; Koningsberger, D. C. J. Phys. Chem. B 1999, 103 (36), 7557-7564.
29. Vjunov, A.; Fulton, J. L.; Govind, N.; Mei, D.; Huthwelker, T.; Shi, H.; Weng, M.; Lercher, J. A. in prep. 2017.
30. Li, D.; Bancroft, G. M.; Fleet, M. E.; Feng, X. H.; Pan, Y., Al K-edge XANES spectra of aluminosilicate minerals. In Am. Mineral., 1995; Vol. 80, p 432.
31. Fulton, J. L.; Govind, N.; Huthwelker, T.; Bylaska, E. J.; Vjunov, A.; Pin, S.; Smurthwaite, T. D. J. Phys. Chem. B 2015, 119 (26), 8380-8388.
32. Fyfe, C. A.; Thomas, J. M.; Klinowski, J.; Gobbi, G. C. Angewandte Chemie-International Edition in English 1983, 22 (4), 259-275.
33. Fyfe, C. A.; Bretherton, J. L.; Lam, L. Y. Chem. Commun. 2000, (17), 1575-1576.
34. Koller, H.; Engelhardt, G.; Kentgens, A. P. M.; Sauer, J. J. Phys. Chem. 1994, 98 (6), 1544-1551.

Chapter 2 – Formation of Faujasite Followed by in situ Spectroscopy

35. Feuerstein, M.; Hunger, M.; Engelhardt, G.; Amoureux, J. P. *Solid State Nucl. Magn. Reson.* 1996, 7 (2), 95-103.
36. Ziarelli, F.; Caldarelli, S. *Solid State Nucl. Magn. Reson.* 2006, 29 (1-3), 214-218.
37. Zhao, Z.; Xu, S.; Hu, M. Y.; Bao, X.; Hu, J. Z. *J. Phys. Chem. C* 2016, 120 (3), 1701-1708.
38. Welsh, L. B.; Lambert, S. L., Analysis of Cation Position in Ion-Exchanged Y Zeolites by ^{23}Na NMR. In *Perspectives in Molecular Sieve Science*, American Chemical Society: 1988; Vol. 368, pp 33-47.
39. Hunger, M.; Engelhardt, G.; Weitkamp, J. *Microporous Mater.* 1995, 3 (4), 497-510.
40. Karge, H. G.; Pal-Borbely, G.; Beyer, H. K. *Zeolites* 1994, 14 (7), 512-518.
41. Samoson, A. *Chem. Phys. Lett.* 1985, 119 (1), 29-32.
42. Melchior, M. T., Silicon and Aluminum Ordering of Zeolites: Interpretation of Silicon-29 NMR Data for Faujasite and ZK4. In *Intrazeolite Chemistry*, American Chemical Society: 1983; Vol. 218, pp 243-265.
43. Feijen, E. J. P.; Martens, J. A.; Jacobs, P. A., Zeolites and their Mechanism of Synthesis. In *Stud. Surf. Sci. Catal.*, J. Weitkamp, H. G. K. H. P.; Hölderich, W., Eds. Elsevier: 1994; Vol. Volume 84, pp 3-21.
44. Thompson, R. W.; Dyer, A. *Zeolites* 1985, 5 (5), 292-301.
45. Kumar, M.; Luo, H.; Roman-Leshkov, Y.; Rimer, J. D. *J. Am. Chem. Soc.* 2015, 137 (40), 13007-13017.

Chapter 3

Improving Stability of Zeolites in Aqueous Phase via Selective Removal of Structural Defects

Missing silicon-oxygen bonds in zeolites are shown to be the cause for structural instability of zeolites in hot liquid water. Their selective removal drastically improved their structural stability as demonstrated using zeolite beta as example. The defects in the siloxy bonds were capped by reaction with trimethylchlorosilane and Si-O-Si bonds were eventually formed. Hydrolysis of Si-O-Si bonds of the parent materials and dissolution of silica-oxygen tetrahedra in water causing a decrease in sorption capacity by re-precipitation of dissolved silica and pore blocking was largely mitigated by the treatment. The stability of the modified molecular sieves was monitored by ^{29}Si -MAS-NMR, transmission electron micrographs, X-ray diffraction, and adsorption isotherms. The microporosity, sorption capacity and long-range order of the stabilized material were fully retained even after prolonged exposure to hot liquid water.

Chapter 3 – Improving Stability of Zeolites in Aqueous Phase via Selective Removal of Structural Defects

INTRODUCTION

Porous aluminosilicates such as zeolites are used as shape selective solid acid catalysts for many industrial processes.^{1,2-3} While the stability against water in gas phase reactions has been studied extensively much less is known about the chemistry of such materials in hot liquid water. Structural and functional stability are, however, essential to be able to use them as catalysts for reactions in which the presence of large concentrations of water is unavoidable. Recent work demonstrate the corrosive properties of hot liquid water and the rapid degradation of zeolites.⁴

Understanding the process of framework decay, as well as its prevention has been addressed in several reports. We have recently shown the pathway of framework destruction in hot liquid water, starting with the selective hydrolysis of tetrahedrally coordinated Si (Si T-sites), and leading eventually to the dissolution and re-precipitation of silica. These processes are accompanied by a loss in sorption capacity and crystallinity.⁵ At the same time de-alumination is not observed with the coordination of Al T-sites remaining mostly unchanged by treatment in hot liquid water.⁶ The reduced catalytic activity is attributed to site blockage by re-precipitation of dissolved silica. The group of Resasco, recently communicated an in-depth study of factors influencing the (poor) stability of zeolites in hot liquid water, confirming that the concentration of silanol defects and the hydrolysis of Si-O-Si bonds are the key factors in the lattice disintegration.⁷

It has been shown by the group of Resasco that hydrophobization with organosilanes improves framework stability of zeolite HY.^{8,9} The initial method aims to lower the rates of hydrolysis by minimizing water concentration in the pores via silylation of the external surface.⁸ Obviously, the approach may be limited, if water is formed at high rates in the pores. Under such circumstances only the direct prevention of the hydrolytic attack of water onto Si-O-Si bonds may stabilize the zeolite, a hypothesis postulated in the follow-up work by Zapata et al.⁹

Based on the detailed insight into the deconstruction of zeolite frameworks in hot liquid water, we decided to explore whether internal SiOH groups can be chemically healed or protected via reaction with a silylating agent. This approach has been explored previously,¹⁰⁻¹³ to modify the chemical composition, as well as the acid and structural properties of zeolites. Chlorosilanes were used for example, by Kraushaar et al, to

Chapter 3 – Improving Stability of Zeolites in Aqueous Phase via Selective Removal of Structural Defects

characterize “SiOH nests”, i.e., the group of up to four OH groups generated by removal of a tetrahedrally coordinated lattice cation.¹²⁻¹³

In this work, we explore the impact of reacting a silylating agent, trimethylchlorosilane (TMS-Cl), with a series of BEA zeolites with well-defined SiOH nest concentrations. The modified materials are examined for their hydrothermal stability and compared to the parent defect-rich zeolites. It will be shown that the stability in hot liquid water, as measured by the retention of the zeolite crystallinity, is improved for the silylated material. It will also be shown that despite hydrolysis generating mesopores in silylated and untreated materials, the microporosity is only retained in the stabilized material. This in turn implies that the specific size and shape selectivity in the BEA framework were also retained.

EXPERIMENTAL SECTION

Chemicals. The silylating agent, Trimethylchlorosilane (TMS-Cl >99.0%), was obtained from Sigma Aldrich and used as received.

Sample preparation

H-form. The boron zeolites were synthesized according to the procedure reported by Derewinski et al.¹⁴ and calcined at 550°C for 6h in air to remove the template. The calcined Na-form was ion-exchanged with 0.1M NH₄NO₃ solution for two hours at 80°C under stirring conditions. The suspension was then centrifuged and the solid re-dispersed in NH₄⁺ solution and the procedure repeated two more times. Upon completion, the material was dried at 80°C overnight, before calcining it once more at 450°C for 6h in air to yield the H-form.

Defect form. The defect form was generated by washing the H-form of the desired zeolite for two hours at 50°C with MilliQ water (1 g : 50 mL H₂O). The suspension was then centrifuged, and the solid residue washed once more under the same conditions. This was followed by another centrifugation step and drying overnight. It yielded the defective starting material used for the following silylation step.

Silylation. The silylation procedure was adapted from a previously described procedure, designed for silica gels and silicalite in closed ampoules.^{12,15} In our case, an open system with flow characteristics was designed.

Chapter 3 – Improving Stability of Zeolites in Aqueous Phase via Selective Removal of Structural Defects

The sample, defect form, was suspended within a quartz tube and placed in a tube furnace. The quartz tube was then connected *via* Teflon tubing to a saturator containing the silylating agent cooled with an ice bath. N₂ carrier gas, set to a specific flow rate, enabled the transport of silane vapors to the reactor and subsequent removal of defects. The other end of the quartz tube was connected to an oil bubbler. If desired, the flow of N₂ could be shut off, essentially generating a reactive atmosphere saturated with silane vapors.

A typical silylation reaction consisted of an activation period, during which the sample was heated, under the flow of N₂, to the desired reaction temperature, typically 300°C, within one hour and then kept at this temperature for two hours. Then, the gas stream was passed through a saturator filled with the silane and allowed to react with the sample. Specific reaction parameters are reported in the SI. The silylated samples were subsequently removed from the quartz tube and used without further purification.

Stability testing. Zeolites underwent hydrothermal water treatment in Teflon lined batch autoclaves at 160°C. Typically, 300 mg of zeolite and 60 mL deionized MilliQ water (1:200) were added to an autoclave, which was then placed in an oven at 160°C. The autoclave was rotated inside the oven. The reactor was kept under these conditions for 48h before cooling it to room temperature, centrifuging the suspension and drying the solid residue at 80°C overnight.

Characterization methods

X-ray diffraction (XRD). XRD patterns were collected on a Rigaku Mini Flex II bench top X-ray diffractometer using a Cu-K α radiation of 0.154056 nm (30 kV and 15 mA). Experiments were conducted on a rotating powder sample holder in a 2θ range of 5° to 60° with a step size of 0.02 °/s. All measurements were performed under ambient conditions.

²⁹Si MAS NMR. The cross-polarization (CP) ²⁹Si MAS NMR experiments were performed using a Varian Inova 89-mm wide-bore 300 MHz NMR spectrometer and a 5 mm HXY MAS Chemagnetics style probe. The following parameters for the cross-polarization pulse sequence were used: the H90 was set to 4 μ sec, the contact time was 3 ms and the decoupling field of 62.5 KHz was applied for 10 ms during the acquisition time. The spinning speed was set to 5 KHz.

Chapter 3 – Improving Stability of Zeolites in Aqueous Phase via Selective Removal of Structural Defects

Helium ion microscopy (HIM). HIM images were obtained using 35 keV He ions with 0.1 pA beam current at normal incidence. Secondary electrons were detected using an Everhart–Thornley detector. For HIM imaging, a very thin layer of carbon (<1 nm) was coated using a carbon sputter deposition system as the samples were completely insulating. The instrument resolution was 0.35 nm.

Thermogravimetric analysis (TGA). A Netzsch STA 449C Jupiter system with an integrated differential scanning calorimeter (DSC) was used to analyze thermal stability. A heating ramp of 5 °C/min up to 1000 °C under a flow of 50 ml/min synthetic air and 15ml/min N₂ was chosen. Typically, 20 mg of material was tested in an Al₂O₃ crucible. The curves were corrected against an empty reference crucible.

Transmission electron microscopy (TEM). Imaging was performed on an FEI Tecnai F20 instrument, operated at 200keV. The images were collected in TEM mode. The samples were prepared by gently crushing the powder between two glass slides, and rubbing a holey carbon grid across the slide with one drop of ethanol.

N₂-physisorption. The BET surface areas and pore size distributions were obtained by physisorption in a Micromeritics ASAP 2020 unit. The pore volumes were determined using the Horvath-Kawazoe method.¹⁶ Micromeritics analysis software provided the method.

Infrared (IR) spectroscopy. The samples for IR measurements were prepared as self-supporting wafers with a density of approximately 10 mg/cm². Upon loading in the IR-cell, the samples were evacuated to (1.0 × 10⁻⁷ mbar) and heated in intervals to 150 °C and 300 °C and kept at 300 °C for 12 h. The heating rate is set to 20 °C/min. Infrared spectra are recorded on a ThermoScientific Nicolete FTIR spectrometer using a MCTA detector with a resolution of 4 cm⁻¹. 128 scans were accumulated for each spectrum. The spectra are normalized to the overtones and combination vibrations of the BEA lattice between 2090 and 1740cm⁻¹.¹⁷

RESULTS AND DISCUSSION

Model system

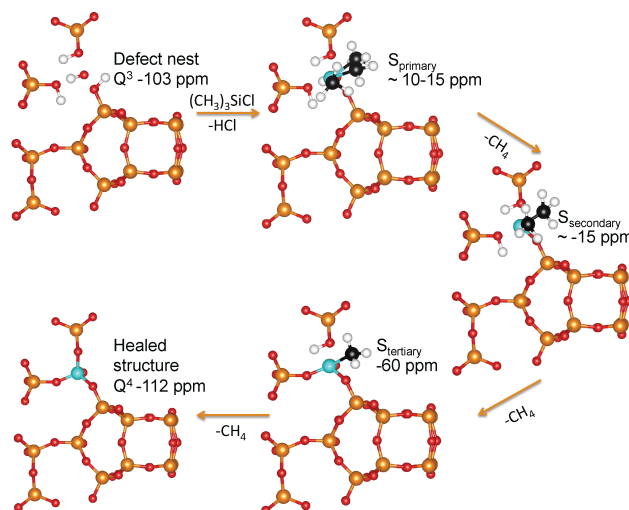
Three samples of zeolite beta (BEA) with varying concentration of defect sites synthesized from boron-containing materials were used to test the impact of improving framework stability through selective removal of structural defects. We focus on the BEA structure, because it has been previously used as an efficient catalyst for acid catalysis in water.⁶ BEA has 12-membered ring pores organized in a three-dimensional network.¹⁸⁻¹⁹ It occurs in three different polymorph structures, of which only polymorphs A (BEA) and B (BEB) are present in the investigated samples.

The intergrowth of the polymorphs as well as their relative abundance was assessed with X-ray diffraction (XRD). The X-ray diffractograms of the materials showed a variety of broad and sharp reflections as the result of the inter-planar stacking faults. This disorder increases the tortuosity of the pores in the (001) plane.²⁰ Of the nine crystallographically distinct tetrahedral sites (T), Vjunov et al. recently showed that the Si T₁ and T₂ sites, connecting the 4-membered ring, are most accessible to hydrolysis.⁵ The boron containing BEA zeolites were synthesized by isomorphous substitution of the tetrahedral Si framework atoms with B.^{14, 21-22} Aluminum was present only in traces as a result of impurities in the silica source. Hence, the Si/Al ratio was higher than 150. Water can leach boron from its framework position *via* nucleophilic attack, forming SiOH nests, i.e., four silanols within close vicinity and tetrahedral geometry. Generally, SiOH nests are considered to be labile at elevated temperatures, resulting in condensation of the hydroxyl groups, subsequent closure of SiOH nests, and a distortion of the framework structure.²³

The zeolites were synthesized in the presence of Na⁺ ions, to minimize charge compensation by the templating amines, which in turn would protect B(SiO)₄⁻ units during calcination.²⁴ During the ion exchange step, Na⁺ cations were replaced with NH₄⁺, which were then decomposed in one last calcination step. Compared to Na⁺ and NH₄⁺, the resulting charge balancing protons are very poor in maintaining the tetrahedral coordination of the framework boron at high calcination temperatures.²⁵ As a result, it becomes trigonally bonded to the framework. In the final step, boron is completely removed from the framework as BO₄⁻ in the presence of water²⁶ as verified by ¹¹B-MAS-NMR. The defect-form (e.g., BEA14_{def}) obtained in this way has defined

Chapter 3 – Improving Stability of Zeolites in Aqueous Phase via Selective Removal of Structural Defects

concentrations of SiOH nests, which directly correlate to the Si/B ratios of the as-made material.



Scheme 1. Schematic depiction of the stepwise process of a typical silylation procedure, showing the removal of silanol nests in BEA structure, and the associated ^{29}Si chemical shifts, is shown. Color coding is as follows: carbon – black ; hydrogen – white ; incorporated silicon – turquoise ; framework silicon – orange ; oxygen – red.

The physicochemical characterization data of the three B-BEA zeolites from which defect-rich materials were derived are shown in Table 1. An upper limit for the concentration of B incorporated corresponding to a Si/B ratio of 14 is apparent.

It appears that the maximum packing density of the charge balancing cations determines this upper concentration.^{22, 27}

The morphologies of the as-made zeolites were probed macroscopically with He ion microscopy (HIM) (Figure A1). All showed well-separated, large pillow-shaped particles ($d \sim 1 \mu\text{m}$) with terrace structures indicating growth along the z-axis.²⁸ The uniformity of the samples, independent of their Si/B ratio, was also reflected in the N_2 -physisorption isotherms (Table 1), indicating nearly identical micro- and mesopore volumes for all three samples.

Note that only B-BEA19 showed a hysteresis loop in the sorption isotherm (Figure A4), indicating some mesoporosity. The HIM images in Figure A1 indicate a larger presence of smaller particles for B-BEA19, which is concluded to induce mesopore formation between particles.

Chapter 3 – Improving Stability of Zeolites in Aqueous Phase via Selective Removal of Structural Defects

Strategies to remove structural defects via Si-reincorporation

A large number of silylating agents capable of reacting with SiOH groups has been documented in literature, including SiCl_4 ,¹¹ silanes - $\text{Si}(\text{CH}_3)_x\text{Cl}_{4-x}$,^{10, 12} octadecyltrichlorosilane⁸ or hexamethyldisilazane.¹⁰ The approach of Kraushaar et al., who silylated silicalite with $\text{Si}(\text{CH}_3)_3\text{Cl}$ (TMS-Cl) was adopted for this study.^{13,15} TMS-Cl was chosen to minimize the concentration of HCl formed during surface reactions. In order to scale production of stabilized zeolites, a flow reactor system was developed, in which silane vapors were passed through the reactor bed using N_2 as carrier gas. The typical reaction pathway for removal of SiOH nests is depicted in Scheme 1. In the first step, TMS-Cl caps a Si-OH defect through a condensation reaction accompanied by the release of HCl. In subsequent steps further defect healing is achieved by Si-O-Si bridge formation and methyl group removal, likely in the form of methane. The optimized reaction conditions are reported in Table A1 in the Appendix.

In order to test the thermal stability of silylated samples, thermogravimetric analysis coupled with a differential scanning calorimetry was conducted. The plots are shown in the Appendix (Figure A2). The exothermic peak, indicative of decomposition of alkyl groups present in the material, has its maximum to 600°C. A continuous mass loss totaling 10% is observed over the whole temperature range, which is attributed to water desorption as well as removal of alkyl groups.⁸ At 300°C only marginal mass loss of 3% was observed. Thus, it can be concluded that the silylated material is stable under the silylation conditions as well as conditions chosen for hydrothermal stability testing.

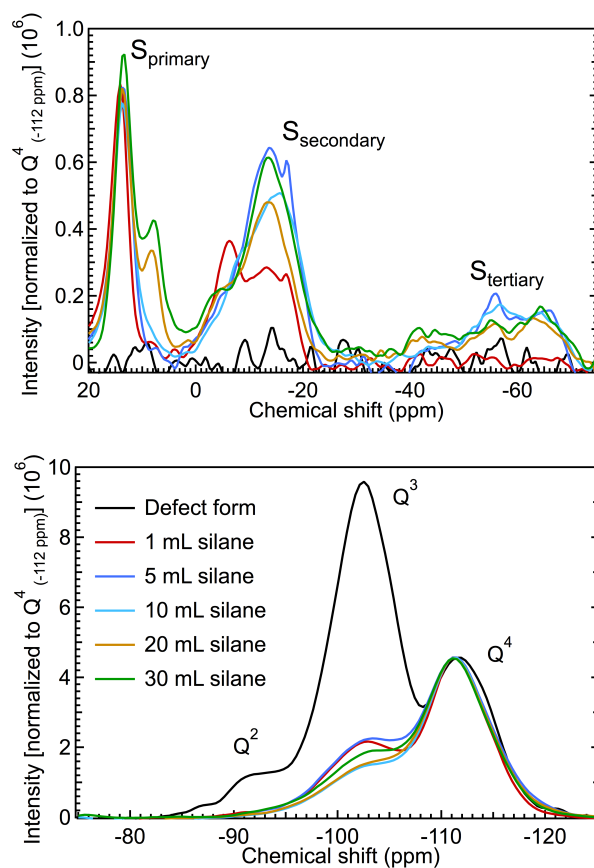


Figure 1. ^{29}Si -CP-MAS-NMR spectra of $\text{BEA16}_{\text{def}}$ with increasing amounts of TMS-Cl (1-20 mL). The intensities are normalized to the Q^4 peak intensity at -112 ppm. Primary silylation product ($\text{S}_{\text{primary}}$) at ~10-15 ppm, secondary product at ~ -15 ppm ($\text{S}_{\text{secondary}}$) and trace amounts of tertiary product ($\text{S}_{\text{tertiary}}$) at -60 ppm. Color-coding is reported in the legend.

Impact of silane

The impact of the amount of silane on the defect healing efficiency was explored using the defect form of B-BEA16 ($\text{BEA16}_{\text{def}}$). The high concentration of defects in this material is evident from the ^{29}Si -CP-MAS-NMR results (Figure 1). The large Si Q^3 peak at -103 ppm associated with the defect $\text{Si}(\text{OH})(\text{OSi})_3$ species significantly outweighs the neighboring Q^4 peak (-112 ppm), caused by Si fully surrounded by other Si atoms, $\text{Si}(\text{OSi})_4$. Additionally, a peak at -92 ppm was observed, attributed to the Q^2 species, $\text{Si}(\text{OH})_2(\text{OSi})_2$.²⁹⁻³⁰ The appearance of Q^2 peaks is related to the presence of silanols in a geminal conformation.³⁰ Note, that the presence of trace amounts of Al (Si/Al 150) results in a signal at -106 ppm³⁰, thus causing a slight overestimation of the contribution of defects.

Chapter 3 – Improving Stability of Zeolites in Aqueous Phase via Selective Removal of Structural Defects

After reaction with TMS-Cl, the Q² and the Q³ peak intensities decreased significantly. Simultaneously, Si species at higher chemical shifts were observed, which are assigned to primary (~10-15 ppm) and secondary (~ -15 ppm) and tertiary (-60 ppm) silylation products (Scheme 1).¹²

Based on the N₂-isotherms (Table 2) silylation also led to a decrease in the micropore volume, whereas the mesopore volume was hardly affected. As the majority of SiOH groups exists inside the channels, the formation of silylation side products leads to reduced micropore accessibility.¹² There appears to be a maximum accessibility loss. Increasing amounts of silane, beyond 10 mL, hardly reduced the micropore volume. Instead, the mesoporosity appears to be slightly reduced, possibly due to silylation of surface hydroxyls and the generation of a mesoporous structure at the outer surface of the particles. Increasing amounts of TMS-Cl reduced the intensity of the Q³ peak, however, there was no significant difference between 10, 20 and 30 mL of TMS-Cl. Instead, an additional peak (~10 ppm) is observed at higher silane loadings, which we attribute tentatively to a dimethylchlorosilyl species attached to a defect SiOH. At such large loadings and temperatures reaction between the methyl group as opposed to the chloro group cannot be ruled out unambiguously leading to the formation of a separate species observed at ~10 ppm rather than 15 ppm. For further Si-O-Si bridge condensation reactions to occur, yielding tertiary (-60 ppm) and quaternary (Q⁴) products, three and four silanol groups, respectively, must be within close proximity and correct geometrical orientation to each other.¹² If SiOH groups are solely found on the particle surface, as in case of silica gels, only the formation of primary and secondary products is possible. Therefore, we conclude that the applied post-synthetic treatment method preferentially removed internal SiOH nests.

Increasing time on stream

Having determined that effective silylation is achieved using as little as 5 mL silane per 0.75 g of zeolite, it was explored, how the time on stream affects the results.

By keeping the sample at 300°C for extended periods, it can be seen in Figure A7 that the concentration of SiOH groups is slightly reduced. Additionally, more primary and secondary silylation products are converted into tertiary (-60 ppm) and quaternary (Q⁴) products. The longer interval at 300°C allows more methyl groups of the deposited

Chapter 3 – Improving Stability of Zeolites in Aqueous Phase via Selective Removal of Structural Defects

silane to react with neighboring Si-OH. Thus, the longer the time, the more the microporosity is regained (Table A2).

Increasing residence time

Adjusting the inlet flow rate of the carrier N₂ gas varied the residence time, i.e., the time for a set amount of TMS-Cl to react with the SiOH groups. This neither improved the pore accessibility, nor further decreased the defect concentration as monitored by NMR spectroscopy and N₂-physisorption (Figure A7 and Table A3). Thus, we conclude that only the longer exposure to high reaction temperatures improves the extent of surface reactions.

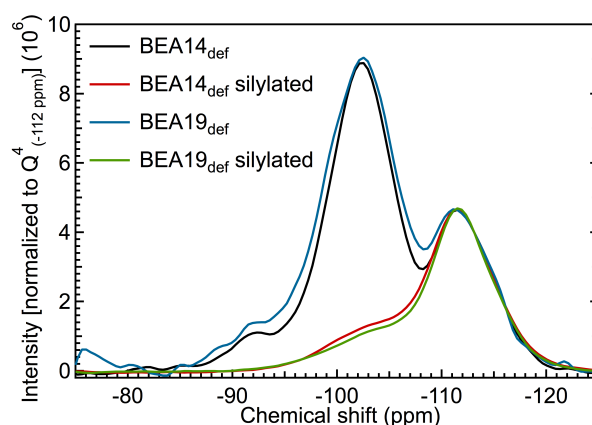


Figure 2. Superimposed ²⁹Si-CP-MAS-NMR spectra normalized to intensity of Q⁴ signal at -112 ppm. The color-coding is reported in the legend.

Method reproducibility

In order to demonstrate the general applicability of this approach, BEA14_{def} and BEA19_{def} samples were investigated. Their ²⁹Si-CP-MAS-NMR spectra are shown Figure 2. An assessment of the Q³ and Q² signal intensities at -103 and -92 ppm respectively leads to the conclusion that both materials have a similar extent of defect concentrations. The samples also show a comparable degree of defect removal and loss in pore volume (50-55%; Table 3). The parallel variation in properties of modified and the unmodified materials demonstrate the general applicability of the method.

The IR spectra of the activated materials clearly show the impact of the modification (Figure A3). The overall impact of silylation is best seen in the difference in the IR spectra before and after silylation (Figure 3). The positive peaks indicate increased intensity; the negative peaks illustrate a decrease. The lattice vibration overtones and

Chapter 3 – Improving Stability of Zeolites in Aqueous Phase via Selective Removal of Structural Defects

combination bands between 2090 and 1740 cm^{-1} did not change. In agreement with the ^{29}Si -CP-MAS-NMR spectra methyl groups remain in the structure (C-H stretching bands at 3000 -2800 cm^{-1} and C-H deformation bands at 1410 cm^{-1}).³¹ Additionally, the bands at 3725 and 3500 cm^{-1} were significantly reduced in both investigated samples. This former band is typically associated with isolated SiOH groups at defect sites and may contain a small contribution of SiOH at external surfaces.³²⁻³⁶ The latter broad band is caused by strong hydrogen bonding of internal SiOH.^{26, 35-37} The silylation reduced, thus, the intensity of both internal SiOH groups. These had been associated with the framework instability via hydrolysis of adjacent Si-O-Si bonds.^{5, 7} Protection or removal of these sites is critical to stabilize zeolites kinetically in hot liquid water.

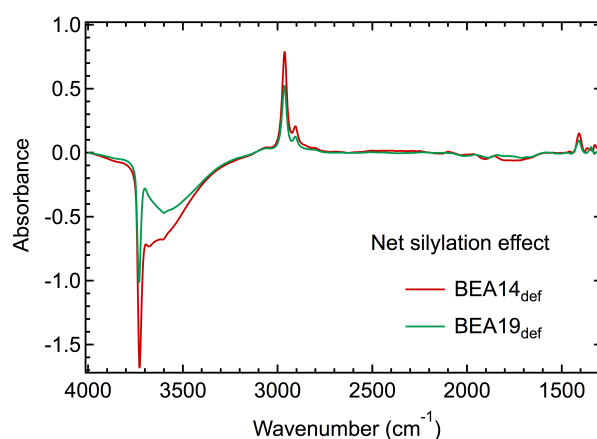


Figure 3. Difference IR spectra illustrating the silylation effectiveness for BEA14_{def} and BEA19_{def}. Positive peaks indicate generation of vibrations, negative peaks removal of vibrations. The spectra were acquired at 300°C in vacuum. Color-coding is reported in the legend.

The generation of tertiary silylation products, the extensive reduction in Q³ peak intensities and the decreased intensities of bands associated with internal SiOH groups show conclusively that the extensive removal of internal structural defects stabilizes. These findings are in agreement with Resasco et al. noting that short-chain alkylchlorosilanes were more effective than long-chain ones to stabilize zeolites in hot liquid water.⁹

Hydrothermal stability of modified zeolites

The impact of removing the internal SiOH of BEA14_{def} and BEA19_{def} on the stability in hot liquid water was explored in an autoclave at 160°C for 48h in an excess of water

Chapter 3 – Improving Stability of Zeolites in Aqueous Phase via Selective Removal of Structural Defects

(1:200). These conditions lead to hydrolysis of the siloxane bonds in the zeolite framework and partial dissolution of the crystal and potential re-precipitation of SiO_2 .^{5,6} The relative crystallinity of the parent and silylated zeolite samples after hydrothermal treatment was estimated by analyzing the areas under all peaks in the X-ray diffractograms allowing to quantitatively assess the effect of stabilization. The stacking faults in the BEA framework lead to sharp and broad peaks in the X-ray diffractograms, with the two main peaks appearing at $\sim 2\theta = 7.5^\circ$ and $2\theta = 22^\circ$.¹⁸ In polymorph B (BEB) these reflections are associated mainly with (-111), (110) and (-332), (330) planes, respectively, while in polymorph A (BEA) planes (101) and (302) have the strongest signal intensity.¹⁹ A substantial loss in the intensity of the XRD peaks, e.g., as observed for $2\theta = 7.5^\circ$ in Figure 4, in the course of framework hydrolysis is attributed to the long-range order of the individual crystallites being reduced.

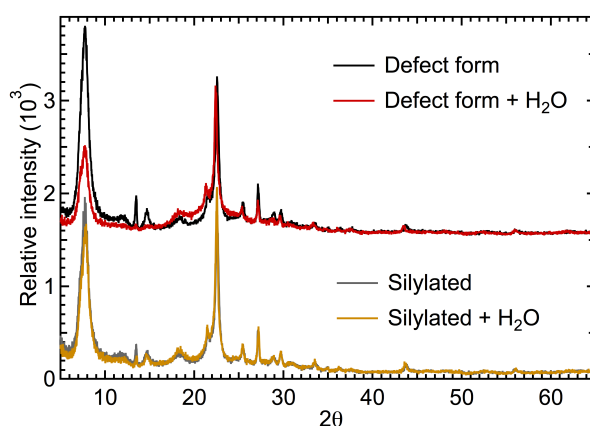


Figure 4. The impact of zeolite hydrothermal treatment on the crystallinity of the BEA framework is shown on the example of XRD patterns collected for the parent and treated $\text{BEA}_{14_{\text{def}}}$. The color-coding is reported in the legend.

Previous work associated this intensity loss with the removal of atoms and generation of defects disrupting the coherency of the related lattice planes.⁵ The fact that only certain planes, in this case mainly (101) for BEA and (-111), (110) in BEB are affected, helps to deduce the degradation mechanism.⁵ These planes run parallel to 4- and 6-membered rings and dissect the same T-O-T bridges ($\text{T}_1\text{-O-T}_1$, $\text{T}_1\text{-O-T}_2$ and $\text{T}_2\text{-O-T}_2$) in the pristine zeolite.

While the defect form lost about 20% of its crystallinity after water treatment at 160°C for 48h, the silylated material remained almost unchanged (Figure 4). A slight shift in

Chapter 3 – Improving Stability of Zeolites in Aqueous Phase via Selective Removal of Structural Defects

the peak position was observed for the parent water-treated material, indicating the modification of the unit cell lattice parameters induced by the degradation of the zeolite. Similar observations were made for BEA19_{def} (see Figure A6). The generation of a separate phase was observed for the water-treated parent material, which is tentatively attributed to magadiite, a layered silicate.³⁸⁻³⁹ The silylated material, in contrast, did not form a new phase, signifying the stabilization.

Framework hydrolysis led to the formation of mesoporosity as well as to partial destruction of the microporous character of the unmodified sample (Table 3), in addition to the loss of crystallinity (as seen by XRD). Yet, the silylated material hardly changed its microporosity after exposure to hot liquid water.

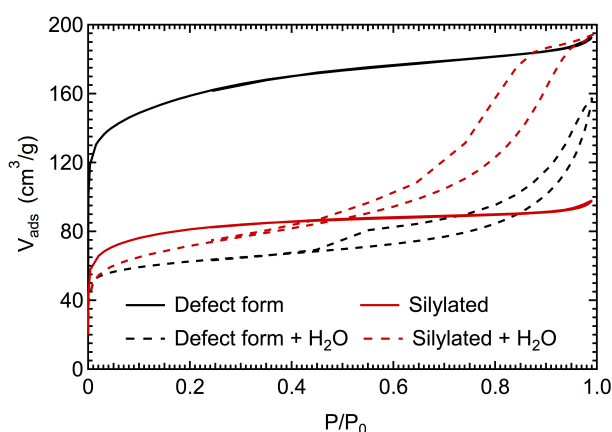


Figure 5. The N₂-sorption isotherms for the parent and silylated form of BEA14_{def} and their respective water-treated counterparts are shown. The color-coding is reported in the legend.

N₂ sorption isotherms in Figure 5 show two different hysteresis shapes. Water treatment of the stabilized material leads to the formation of a hysteresis loop resembling H2 type,⁴⁰ indicating non-uniform cylindrical pore shapes. The pores are likely to have ink-bottle shapes due to a longer retention of the adsorbate at high relative pressures during the desorption process. This specific type, has a smaller pore mouth than pore body, hence the non-uniform hysteresis shape.⁴¹ For the unmodified material, water treatment leads to a very different and atypical hysteresis.

While only the isotherm of BEA14_{def} is presented here, BEA19_{def} behaves the same (see Figure A5). We hypothesize, therefore, that introduction of water to the silylated material at elevated temperatures leads to ink-bottle mesopores, whereas the

Chapter 3 – Improving Stability of Zeolites in Aqueous Phase via Selective Removal of Structural Defects

unmodified material forms ill-defined mesopores or mesovoids. The differences in the mesopore shapes are a direct effect of the silylation.

Having established that water treatment of the silylated material does not only result in retention of crystallinity and microporosity, but also changes the mesoporosity compared to the unmodified material, we turn to transmission electron microscopy (TEM). The images in Figure 6 show different magnifications of the defect form BEA14_{def} after water treatment. The dark areas are attributed to increasing sample thickness. Small crystallites adjacent to larger particles are observed. The presence of lattice fringes indicates that these fragments are crystalline.

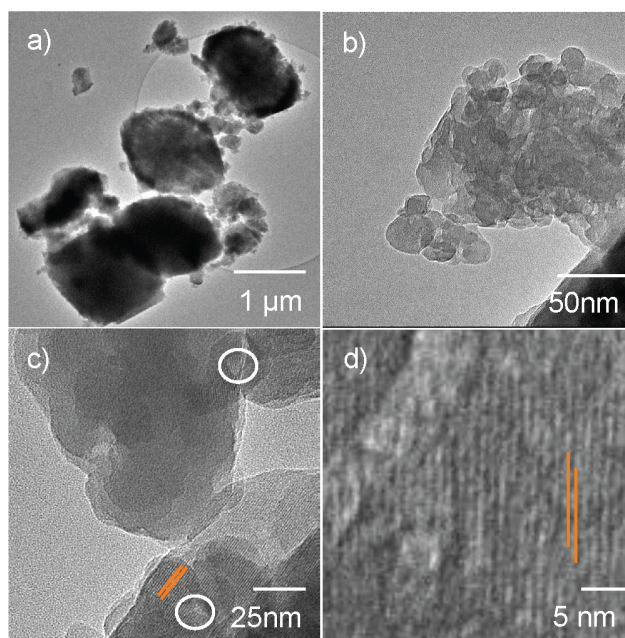


Figure 6. TEM images of water treated defect form, BEA14_{def} + H₂O. Mesopores are shown with white circles, lattice fringes in orange. The fringes are still present on observed small particles.

The small particles are agglomerates of even smaller crystallites, forming inter-crystal mesovoids amongst them, in line with the hysteresis shape observed with N₂ sorption reported above. This reduction in particle size is attributed to the cleavage of siloxy bonds and the subsequent dissolution of silica leading to cracking and fracturing of the crystals.⁵ TEM images in Figure 7 illustrate the macroscopic morphology of silylated particles and their porous character after water treatment.

Chapter 3 – Improving Stability of Zeolites in Aqueous Phase via Selective Removal of Structural Defects

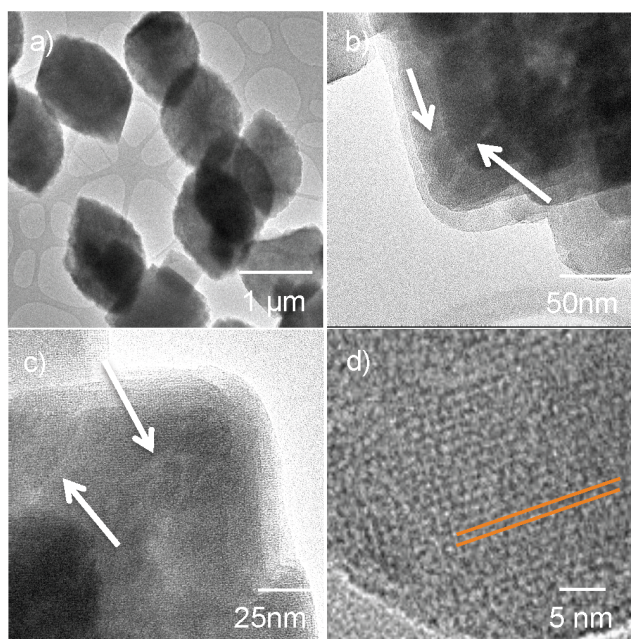


Figure 7. TEM images of water-treated silylated material, BEA14_{def} silylated + H₂O. Channel-type mesopores can be observed next to white arrows, lattice fringes in orange. No fractured particles were observed.

The significant difference between water-treated defective and silylated material is the absence of small crystallites in the latter. Water-treatment has no effect on the macroscopic morphology of the stabilized materials, as can be seen by comparison with TEM images in Figure A9 of the Appendix. However, mesopores are observed, as micropores remained clearly visible. While the mesoporosity is similar, the shape of the pores formed, is different between the defect and the stabilized material. Long elongated mesopores are observed at the edges of the water-treated silylated material. Similar observations were made for BEA19_{def}, with the images shown in the Appendix (Figure A10). However, that material showed less fracturing than BEA14_{def}. Both the unmodified and silylated material appear quite similar after water-treatment in terms of particle morphology and size. However, at closer inspection, the unmodified material presents a lower particle density due to excessive formation of mesopores.

We conclude that silylation removes most defects resulting in a drastic retardation of the framework hydrolysis. The mesoporosity generated is presented in the form of channels with narrow pore mouths due to the fact that cleavage of the Si-O-Si bonds progresses along the few remaining defects. In the parent defective form hydrolysis

Chapter 3 – Improving Stability of Zeolites in Aqueous Phase via Selective Removal of Structural Defects

proceeds at more sites and distributed throughout the crystal, leading to fragmentation of crystallites.

The XRD results confirm that crystallinity is retained in the stabilized material after water treatment, inferring that fewer atoms are removed such that the coherency of the planes is less disrupted. In the defect form on the other hand, the reduction in crystallite size as well as extensive removal of atoms spread over the whole particle leads to a disruption of the plane integrity and resulting loss in XRD peak intensity. The XRD and TEM analyses agree well with the ^{29}Si -CP-MAS-NMR analysis (Figure 8) that show the comparison of the Si-OH intensities measured for the parent and stabilized zeolite BEA14_{def} upon treatment in hot liquid water (for BEA19_{def} see Figure A8). The Q³ signal intensity was significantly reduced for the water-treated unmodified material. We attribute the loss in Q³ signal intensity to fracturing and loss of microporosity. The starting material has a high fraction of internal SiOH giving rise to a large Q³ signal (-103 ppm).

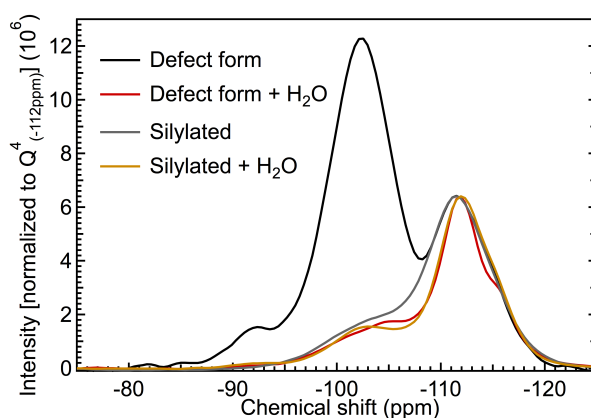


Figure 8. ^{29}Si -CP-MAS-NMR spectra of unmodified and silylated BEA14_{def} before and after water treatment at 160°C for 48h. Color-coding is reported in the legend. The full spectrum can be found in the Appendix (Figure A8).

Water treatment removes a major fraction of these silanols as it cleaves neighboring Si-O-Si bridges, leading to fracturing. The small crystallites still yield a Q⁴ signal. However, due to the particles being mostly defect free, the Q³ signal is significantly reduced, with the remaining signal being contributed to surface SiOH groups (-100 ppm).⁴² It is noted in passing that the cross-polarization enhancement factor varies

Chapter 3 – Improving Stability of Zeolites in Aqueous Phase via Selective Removal of Structural Defects

between internal silanols and surface silanols hindering a quantitative assessment of SiOH concentrations.⁴²⁻⁴³

In the case of the stabilized material only small changes were observed by Si-MAS-NMR spectroscopy, which is in agreement with minor changes in crystallinity (XRD) and morphology (TEM). The formation of mesopores at the expense of micropores leads to the removal of material from the crystal body. This material initially contained a relatively high concentration of Si-OH groups in the form of nests (Q^3). The conditions of the cross-polarization experiment were optimized to enhance these SiOH nests with a high density of protons (-103 ppm). However, the resulting mesopores have mostly surface Si-OH groups (- 100 ppm) on the walls. They are isolated and the lower proton concentration is likely to result in a lesser enhancement and thus a smaller peak in the Q^3 region.

Chapter 3 – Improving Stability of Zeolites in Aqueous Phase via Selective Removal of Structural Defects

CONCLUSIONS

The zeolite post-synthetic silylation treatment is demonstrated to significantly improve material stability in hot liquid water, under retention of crystallinity and microporosity. Silylation reduces efficiently the concentration of internal structural defects, known to be the primary active sites for framework hydrolysis. The reported procedure is expected to be applicable to a range of zeolites prone to hydrolysis. The silylation treatment is suggested as a potential pathway toward stabilizing and extending the lifetime of Al-rich zeolites enhancing their use as a solid acid catalyst in aqueous phase, e.g., dehydration of alcohols and alkylation of phenols in hot liquid water.

Chapter 3 – Improving Stability of Zeolites in Aqueous Phase via Selective Removal of Structural Defects

ACKNOWLEDGMENT

B.W. Arey (PNNL) is acknowledged for performing HIM measurements, J.L. Fulton and D.M. Camaioni for their valuable input and discussion. This work was supported by the US Department of Energy, Office of Science, Office of Basic Energy Sciences and by the Materials Synthesis and Simulation Across Scales (MS³ Initiative) conducted under Laboratory Directed Research & Development Program at PNNL. Pacific Northwest National Laboratory (PNNL) is a multiprogram national laboratory operated for DOE by Battelle.

Chapter 3 – Improving Stability of Zeolites in Aqueous Phase via Selective Removal of Structural Defects

APPENDIX

Silylation parameters

Several parameters such as amount of silane, reaction time, and flow rate were varied to investigate their effect on the effectiveness of silylation, listed in Table A1.

Table A1. A list of all silylation experiments conducted, with varied parameters per 0.75g of BEA_{def}.

Experiment	Boron concentration [mmol/g]	N ₂ flow rate [ml/min]	Time on stream [h]	Silane [mL]	Molar excess
1	0.81	50	0.55	1	15
2	0.81	50	2.75	5	65
3	0.81	50	5.5	10	130
4	0.81	50	11	20	260
5	0.81	50	16.5	30	390
6	0.81	50	5.5	5	65
7	0.81	50	11	5	65
8	0.81	50	22	5	65
9	0.67	75	11	5	80
10	0.67	50	11	5	80
11	0.67	25	11	5	80
12	0.88	50	11	5	60

Helium ion microscopy

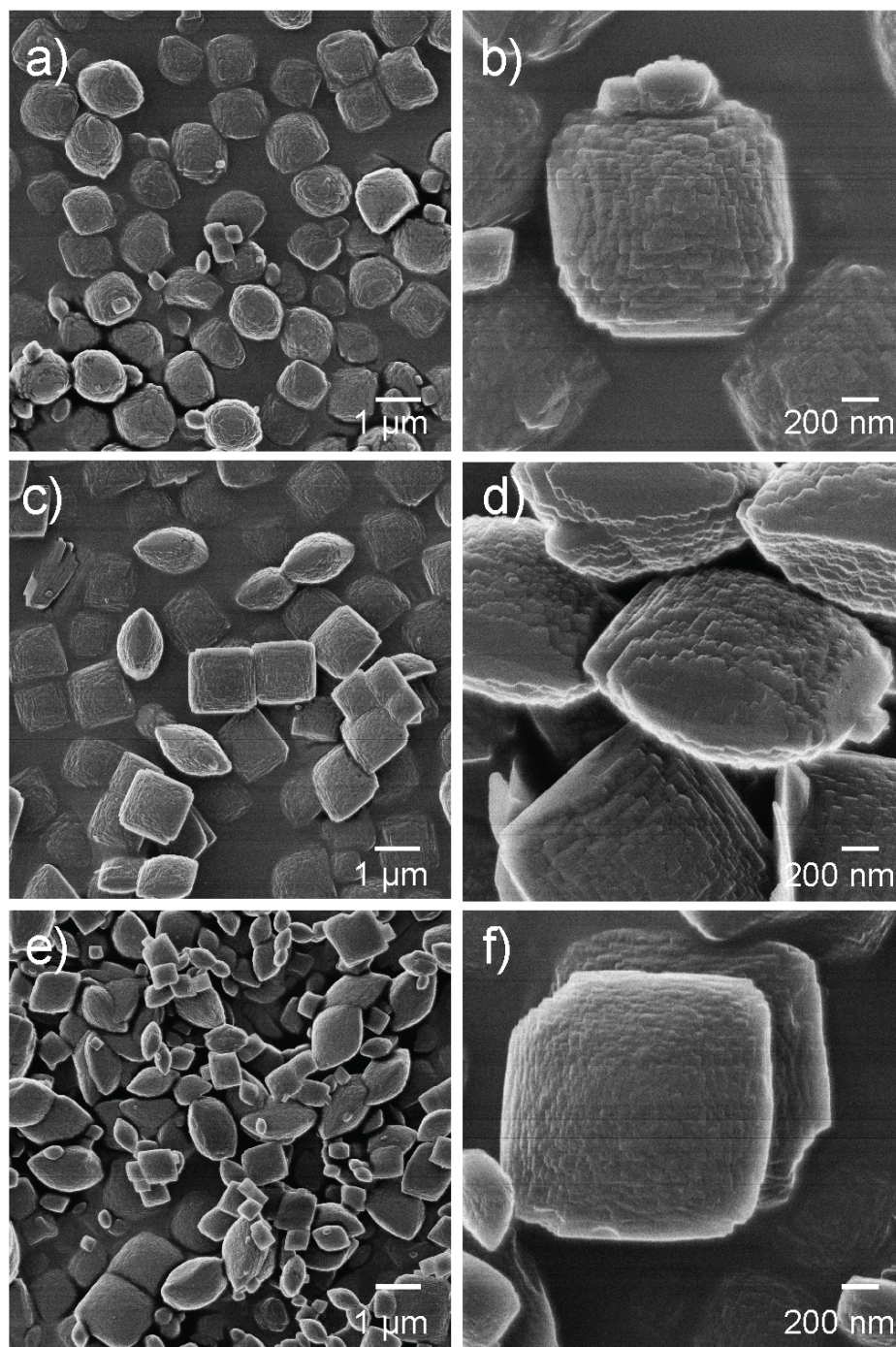


Figure A1. HIM images showing morphology of the investigated as-made samples B-BEA14 (a&b), B-BEA16 (c&d) and B-BEA19 (e&f). The magnifications are reported in the images.

Thermogravimetric analysis

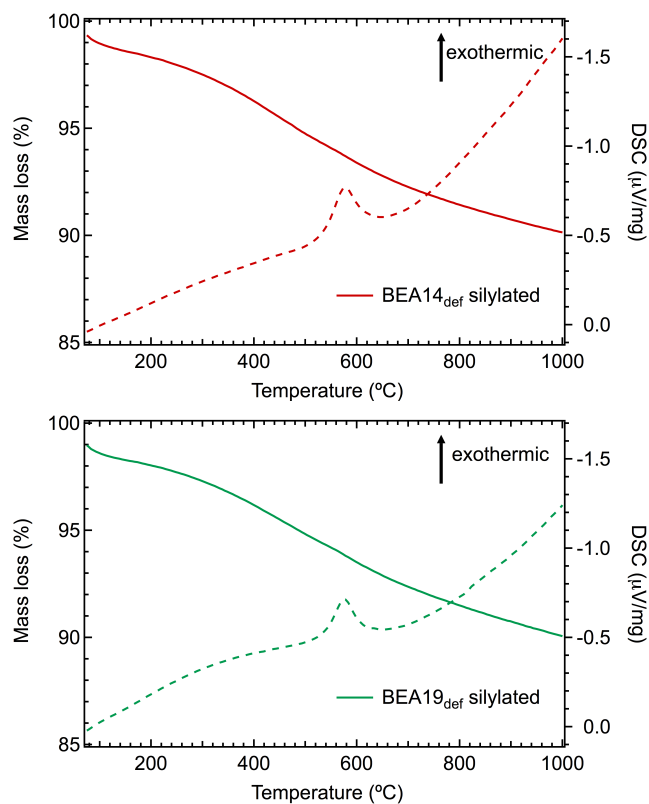


Figure A2. TG and DSC curves analyzing the temperature dependent changes of the silylated materials. In both cases a mass loss of 10% is observed up to 1000 °C. An exothermic peak close to 600 °C is attributed to the combustion of methyl groups. Only 3% mass loss is observed up to 300 °C.

Infrared Spectroscopy

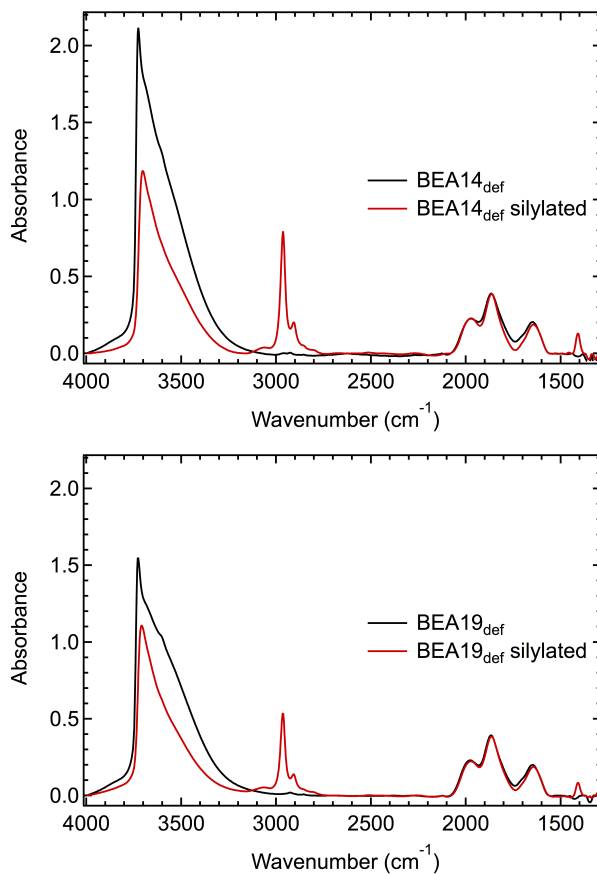


Figure A3. IR spectra of BEA14_{def} and BEA19_{def} before and after silylation measured at 300 °C. The spectra were normalized to the overtones and combination vibration bands of the BEA framework between 2090 and 1750 cm⁻¹. Silylation clearly reduces the vibrations at 3500 cm⁻¹ associated with H-bonded internal silanol nests. At the same time isolated internal silanols (3725 cm⁻¹) were also removed.

Chapter 3 – Improving Stability of Zeolites in Aqueous Phase via Selective Removal of Structural Defects

N₂-physorption

Isotherms for silylated materials are shown in Figure A4. Figure A5 shows the corresponding isotherm for defect form and silylated material of BEA16_{def} and BEA19_{def} and its water-treated counterparts respectively.

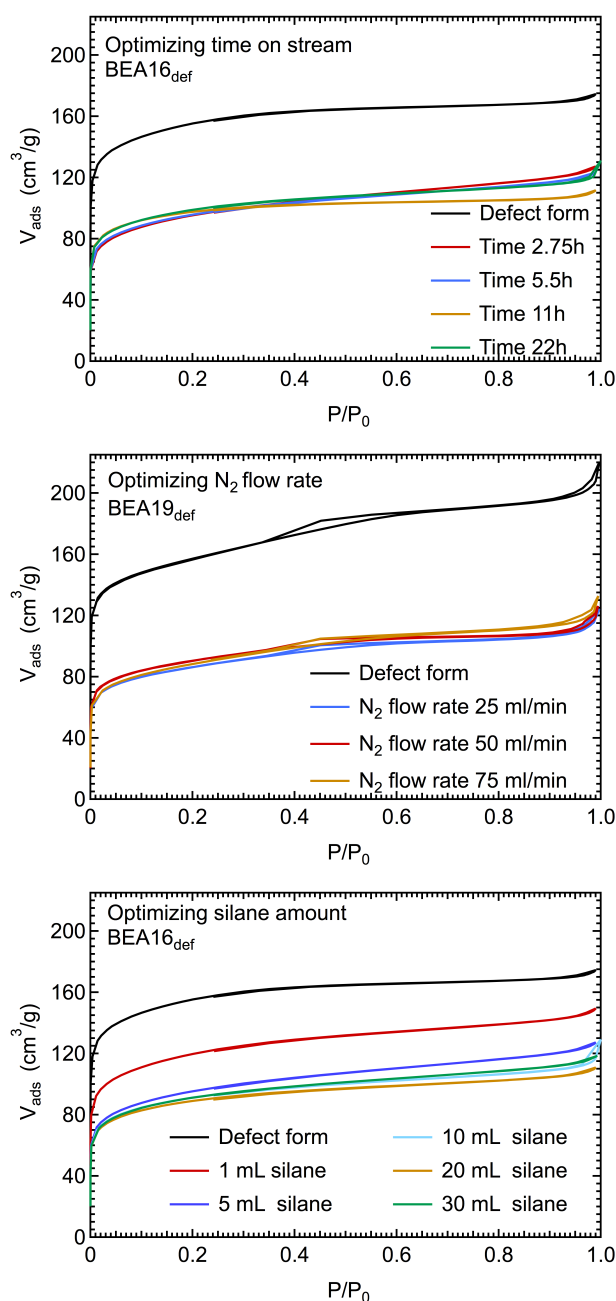


Figure A4. Showing the sorption isotherms for BEA_{def} zeolites with varying silylation parameters.

Chapter 3 – Improving Stability of Zeolites in Aqueous Phase via Selective Removal of Structural Defects

Table A2. N₂-physorption data for BEA16_{def} silylated with 5mL TMS-Cl and increasing time on stream

Sample	BET [m ² /g]	micropore volume [cm ³ /g]	mesopore volume [cm ³ /g]
Defect form	585	0.23	0.03
Silylated – time 2.75h	340	0.14	0.05
Silylated – time 5.5h	345	0.14	0.04
Silylated – time 11h	360	0.15	0.02
Silylated – time 22h	360	0.15	0.03

Table A3. Presentation of N₂-physorption data for BEA19_{def} silylated with increasing flow rate.

Sample	BET [m ² /g]	micropore volume [cm ³ /g]	mesopore volume [cm ³ /g]
Defect form	585	0.23	0.07
Silylated – flow rate 25 ml/min	310	0.13	0.04
Silylated – flow rate 50 ml/min	330	0.13	0.04
Silylated - flow rate 75 ml/min	320	0.13	0.05

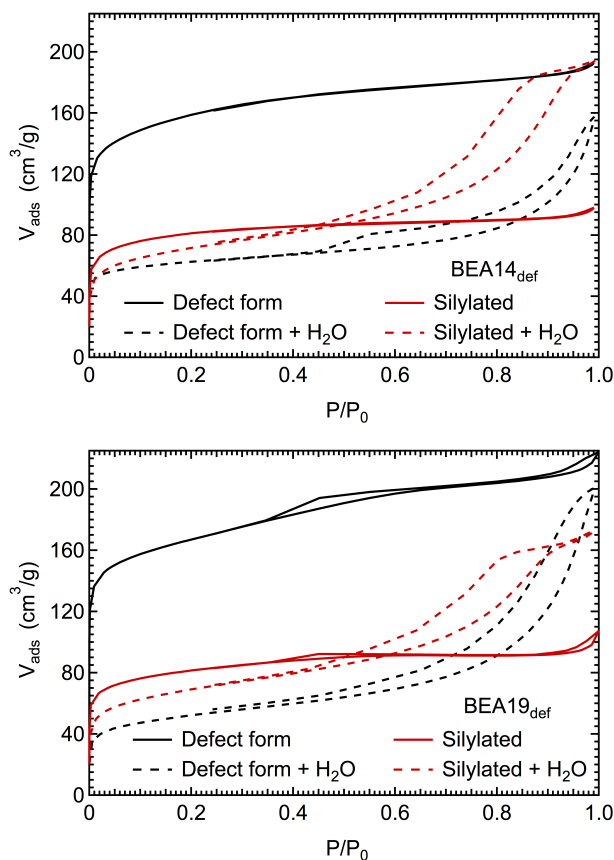


Figure A5. The effect water treatment has on the sorption isotherms of stabilized and unmodified material. The hysteresis shapes resulting from the water-treatment in Figure A5 differentiate between silylated and unmodified materials. The hysteresis for silylated materials indicates retention of the adsorbate during desorption at lower pressures, compared to the unmodified water-treated materials.

Chapter 3 – Improving Stability of Zeolites in Aqueous Phase via Selective Removal of Structural Defects

X-ray Diffraction

The diffractograms for defect form and silylated material before and after water treatment are shown in Figure A6. The estimated crystallinity is assessed by simple line fitting of all peaks, followed by fitting a broad amorphous peak at 22° and determining the ratio of crystalline to amorphous material using the analysis program provided by Rigaku.

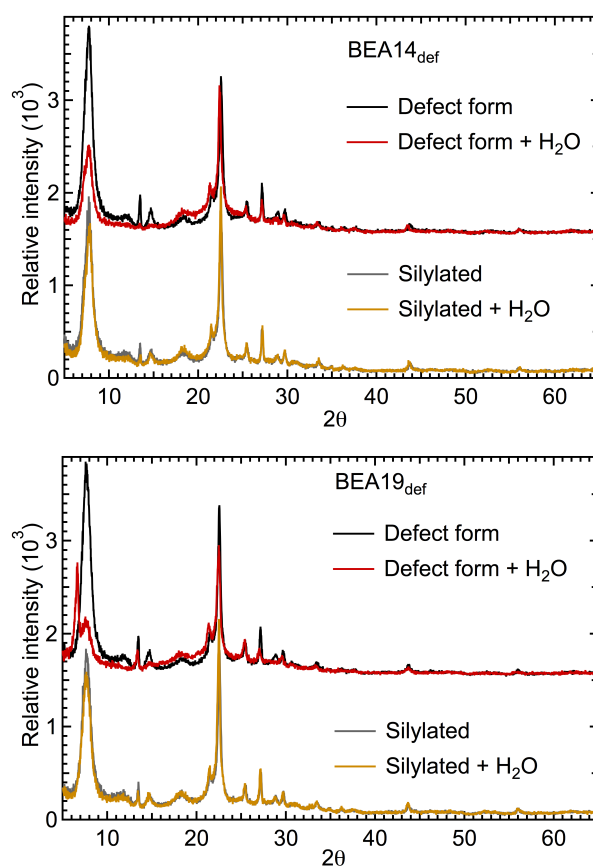


Figure A6. Showing diffractograms for BEA14_{def} and BEA19_{def} to illustrate the effect water has on the crystallinity. BEA14_{def} (top) loses 20% for the unmodified material with silylation reducing that loss to 1%. BEA19_{def} (bottom) loses 23% and stabilization reducing this number to 2.5%.

Chapter 3 – Improving Stability of Zeolites in Aqueous Phase via Selective Removal of Structural Defects

^{29}Si -CP-MAS NMR

Cross-polarization ^{29}Si -MAS NMR spectra are shown to illustrate the effect of varying reaction time and residence time has on the defect concentration (Figure A7) as well the effect water treatment has on the unmodified and stabilized material (Figure A8).

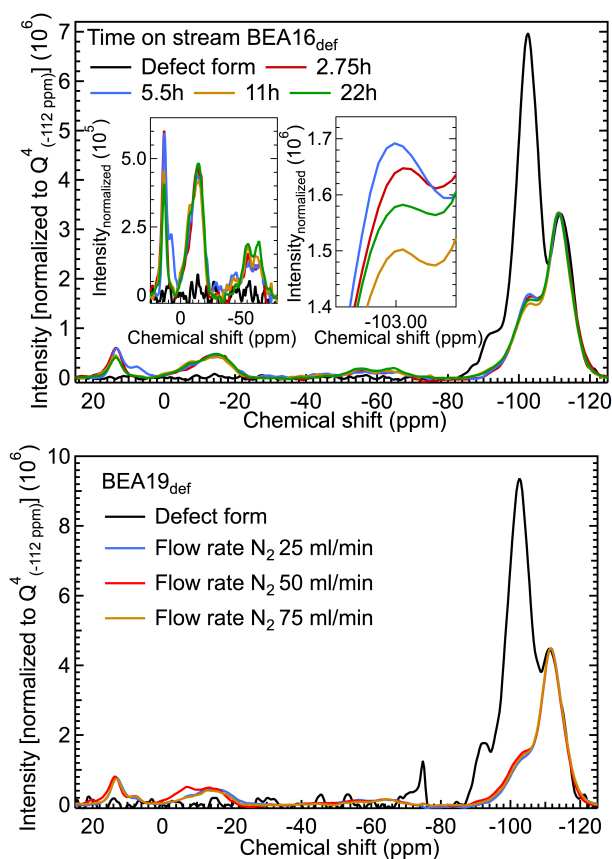


Figure A7. Spectra showing the influence the time on stream has on the defect concentration in BEA16_{def} (top). Also, it can be seen (bottom) that changing the N₂ carrier gas flow rate has no effect on the defect concentration in BEA19_{def}.

Chapter 3 – Improving Stability of Zeolites in Aqueous Phase via Selective Removal of Structural Defects

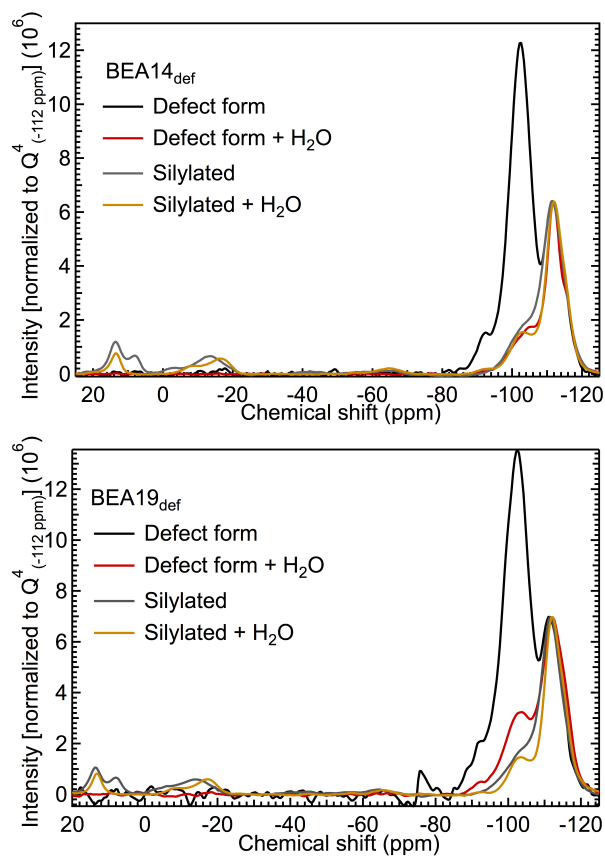


Figure A8. Spectra of unmodified and stabilized material before and after water treatment. The reduction in Q^3 intensity is related to formation of mesopores and fracturing of particles, in agreement with N_2 -sorption and TEM images.

Transmission electron microscopy

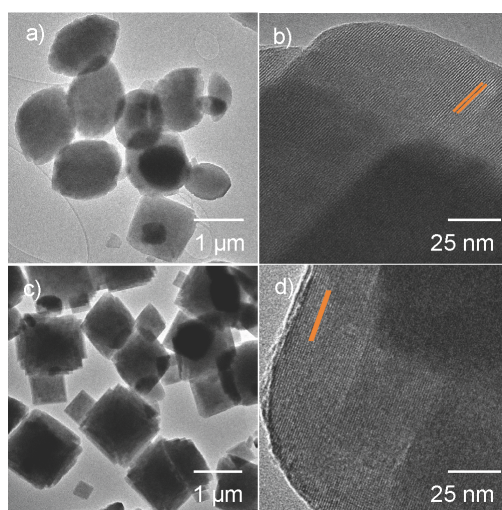


Figure A9. TEM images of the defect form (a&b) as well as silylated materials (c&d) before water treatment for BEA14_{def} are shown. Lattice fringes are shown in orange. No mesopores were observed. The magnifications are reported in the images.

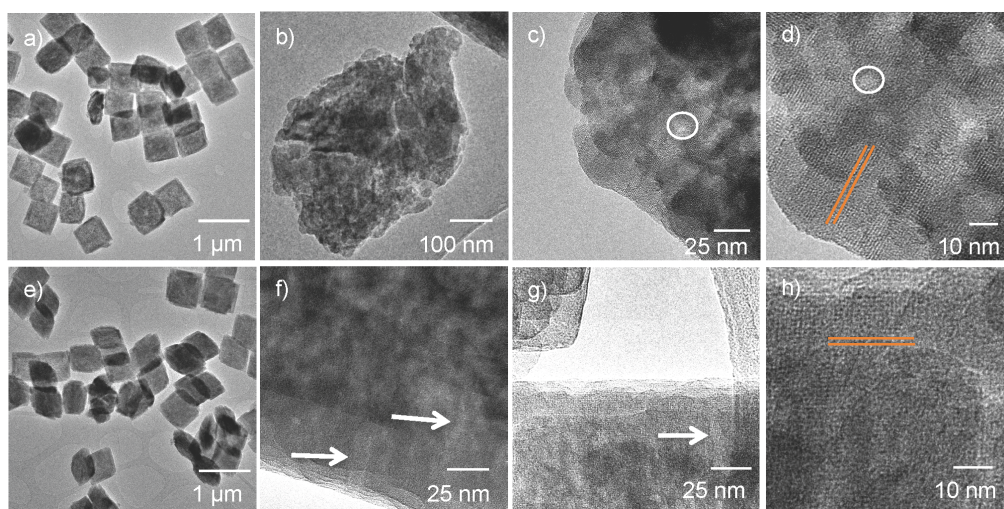


Figure A10. TEM images illustrating the effect water treatment has on unmodified (a-d) and silylated (e-h) BEA19_{def}. Note the homogeneity of the silylated material after water treatment compared to the defect rich material on the left at low magnifications. Mesopores are marked with white circles/arrows, lattice fringes in orange. Magnifications are reported in the legend.

Chapter 3 – Improving Stability of Zeolites in Aqueous Phase via Selective Removal of Structural Defects

REFERENCES

1. Yilmaz, B.; Müller, U. *Top. Catal.* 2009, 52 (6-7), 888-895.
2. Zhao, C.; Kou, Y.; Lemonidou, A. A.; Li, X.; Lercher, J. A. *Chem. Commun.* 2010, 46 (3), 412-414.
3. Zhao, C.; Camaioni, D. M.; Lercher, J. A. *J. Catal.* 2012, 288, 92-103.
4. Ravenelle, R. M.; Schüßler, F.; D'Amico, A.; Danilina, N.; van Bokhoven, J. A.; Lercher, J. A.; Jones, C. W.; Sievers, C. *J. Phys. Chem. C* 2010, 114 (46), 19582-19595.
5. Vjunov, A.; Fulton, J. L.; Camaioni, D. M.; Hu, J. Z.; Burton, S. D.; Arslan, I.; Lercher, J. A. *Chem. Mater.* 2015, 27 (9), 3533-3545.
6. Vjunov, A.; Derewinski, M. A.; Fulton, J. L.; Camaioni, D. M.; Lercher, J. A. *J. Am. Chem. Soc.* 2015, 137 (32), 10374-10382.
7. Zhang, L.; Chen, K.; Chen, B.; White, J. L.; Resasco, D. E. *J. Am. Chem. Soc.* 2015, 137 (36), 11810-11819.
8. Zapata, P. A.; Faria, J.; Ruiz, M. P.; Jentoft, R. E.; Resasco, D. E. *J. Am. Chem. Soc.* 2012, 134 (20), 8570-8578.
9. Zapata, P. A.; Huang, Y.; Gonzalez-Borja, M. A.; Resasco, D. E. *J. Catal.* 2013, 308, 82-97.
10. Huang, M.; Adnot, A.; Kaliaguine, S. *J. Chem. Soc., Faraday Trans.* 1993, 89 (23), 4231-4237.
11. Klinowski, J.; Thomas, J. M.; Anderson, M. W.; Fyfe, C. A.; Gobbi, G. C. *Zeolites* 1983, 3 (1), 5-7.
12. Kraushaar, B.; Van De Ven, L. J. M.; De Haan, J. W.; Van Hooff, J. H. C. *Stud. Surf. Sci. Catal.* 1988, 37, 167-174.
13. Kraushaar, B.; de Haan, J. W.; van De Ven, L. J. M.; van Hooff, J. H. C. *Z. Anorg. Allg. Chem.* 1988, 564 (1), 72-80.
14. Derewinski, M.; Renzo, F. D.; Espiau, P.; Fajula, F.; Nicolle, M.-A. *Stud. Surf. Sci. Catal.* 1991, 69, 127-134.
15. Rutten, G.; van de Ven, A.; de Haan, J.; van de Ven, L.; Rijks, J. *J. High. Resolut. Chromatogr.* 1984, 7 (11), 607-614.
16. Horváth, G.; Kawazoe, K. *J. Chem. Eng. Jpn.* 1983, 16 (6), 470-475.
17. Jentys, A.; Lercher, J. A. *Stud. Surf. Sci. Catal.* 1989, 46, 585-594.

Chapter 3 – Improving Stability of Zeolites in Aqueous Phase via Selective Removal of Structural Defects

18. Higgins, J. B.; LaPierre, R. B.; Schlenker, J. L.; Rohrman, A. C.; Wood, J. D.; Kerr, G. T.; Rohrbaugh, W. J. *Zeolites* 1988, 8 (6), 446-452.
19. Baerlocher, C.; McCusker, L. B. Database of Zeolite Structures. <http://www.iza-structure.org/databases/>.
20. Newsam, J. M.; Treacy, M. M. J.; Koetsier, W. T.; Gruyter, C. B. D. *Proc. R. Soc. London, Ser. A* 1988, 420 (1859), 375-405.
21. Reddy, K. S. N.; Eapen, M. J.; Joshi, P. N.; Mirajkar, S. P.; Shiralkar, V. P. *J. Inclusion Phenom. Mol. Recognit. Chem.* 1994, 20 (3), 197-210.
22. de Ruite, R.; Famine, K.; Kentgens, A. P. M.; Jansen, J. C.; van Bekkum, H. *Zeolites* 1993, 13 (8), 611-621.
23. Kerr, G. T. *J. Phys. Chem.* 1969, 73 (8), 2780-2782.
24. Kuehl, G. H. US Pat. 4 661 467, 1987.
25. Fild, C.; Shantz, D. F.; Lobo, R. F.; Koller, H. *Phys. Chem. Chem. Phys.* 2000, 2 (13), 3091-3098.
26. de Ruiter, R.; Kentgens, A. P. M.; Grootendorst, J.; Jansen, J. C.; van Bekkum, H. *Zeolites* 1993, 13 (2), 128-138.
27. de Ruiter, R.; Jansen, J. C.; van Bekkum, H. *Zeolites* 1992, 12 (1), 56-62.
28. Cundy, C. S.; Cox, P. A. *Chem. Rev.* 2003, 103 (3), 663-702.
29. Fyfe, C. A.; Gobbi, G. C.; Kennedy, G. J. *J. Phys. Chem.* 1985, 89 (2), 277-281.
30. Hunger, M.; Karger, J.; Pfeifer, H.; Caro, J.; Zibrowius, B.; Bulow, M.; Mostowicz, R. *J. Chem. Soc., Faraday Trans. 1* 1987, 83 (11), 3459-3468.
31. Mirth, G.; Lercher, J. A.; Anderson, M. W.; Klinowski, J. *J. Chem. Soc., Faraday Trans.* 1990, 86 (17), 3039-3044.
32. Woolery, G. L.; Alemany, L. B.; Dessau, R. M.; Chester, A. W. *Zeolites* 1986, 6 (1), 14-16.
33. Datka, J.; Tużnik, E. *Zeolites* 1985, 5 (4), 230-232.
34. Maier, S. M.; Jentys, A.; Lercher, J. A. *J. Phys. Chem. C* 2011, 115 (16), 8005-8013.
35. Takei, T.; Kato, K.; Meguro, A.; Chikazawa, M. *Colloids Surf., A* 1999, 150 (1-3), 77-84.
36. Krijnen, S.; J. Harmsen, R.; C. L. Abbenhuis, H.; H. C. Van Hooff, J.; A. Van Santen, R. *Chem. Commun.* 1999, (6), 501-502.

Chapter 3 – Improving Stability of Zeolites in Aqueous Phase via Selective Removal of Structural Defects

37. Holm, M. S.; Svelle, S.; Joensen, F.; Beato, P.; Christensen, C. H.; Bordiga, S.; Bjørgen, M. *Appl. Catal., A* 2009, *356* (1), 23-30.
38. Fletcher, R. A.; Bibby, D. M. *Clays Clay Miner.* 1987, *35* (4), 318-320.
39. Eugster, H. P. *Science* 1967, *157* (3793), 1177-1180.
40. Sing, K. S. W.; Everett, D. H.; Haul, R. A. W.; Moscou, L.; Pierotti, R. A.; Rouquerol, J.; Siemieniowska, T. *Pure Appl. Chem.* 1985, *57* (4), 603-619.
41. Leofanti, G.; Padovan, M.; Tozzola, G.; Venturelli, B. *Catal. Today* 1998, *41* (1-3), 207-219.
42. Engelhardt, G.; Lohse, U.; Samoson, A.; Mägi, M.; Tarmak, M.; Lippmaa, E. *Zeolites* 1982, *2* (1), 59-62.
43. Sindorf, D. W.; Maciel, G. E. *J. Phys. Chem.* 1982, *86* (26), 5208-5219.

Chapter 4

Stability of Zeolites in Aqueous Phase Reactions

Strategies to understand and mitigate the corrosive interactions of zeolites in aqueous phase under reaction conditions have been explored using zeolite BEA as an example. The state of Si and Al atoms after chemical modification and during gradual degradation were followed by cross-polarization enhanced ^{29}Si MAS NMR, ^{27}Al MAS NMR as well as IR spectroscopy. The key to stabilizing a zeolite for aqueous phase catalysis is to reduce the pore concentration of water in presence of reacting substrates. The concentration of tetrahedral aluminum, which is charge balanced by hydrated hydronium ions, is the most important parameter determining the concentration of water in the zeolite pores. Lower intraporous water concentrations, largely independent of ubiquitous defects, led to longer zeolite lifetimes during cyclohexanol dehydration. The concentration of intraporous water was directly related to the rate of hydrolysis of Si^{4+} from the zeolite lattice and its removal from the crystal. Dissolution of Si^{4+} led eventually to a loss of confinement of the catalytically active hydronium ions and decreased so the catalytic activity. At low Brønsted acid site concentrations, water bound to lattice defects begins to exert a measurable influence on the stability under reaction conditions.

INTRODUCTION

Increasing efforts have been devoted to applying zeolites to aqueous phase conversions of organic molecules including the conversion of biomass-derived feedstocks.¹⁻⁵ One of the key challenges for these applications has been the insufficient stability of zeolites in hot liquid water (HLW) which is primarily due to desilication.^{4, 6} Recently, the elementary steps of these processes were characterized by structural analyses, identifying the Si-O-Si hydrolysis pathway leading to framework collapse, and identifying the concentration of silanol-terminated lattice defects as the main factor responsible for framework disintegration.⁷⁻⁸

In order to improve the stability of zeolites in HLW, several groups focused on the minimization of defect concentration and the removal of SiOH groups associated with these defects. Resasco and co-workers were amongst the first to increase the hydrophobicity of SiO₂ surfaces with long chain alkyl chlorosilanes followed by preferential silylation of internal surfaces with smaller silanes.⁹⁻¹⁰ Sels et al. showed that extra-framework Al (EFAI) could be used to form a protective layer capping terminal SiOH groups, which retards or prevents the degradation of the framework.¹¹ While both studies focused on ultra-stable Y zeolites (USY; FAU framework type), we have explored stabilization strategies for the BEA framework, which is better suited for organic transformations.¹²⁻¹⁴ Both FAU and BEA structures are in principle quite labile in HLW because of their low framework density.¹⁵ As a first step towards developing methods to stabilize BEA zeolites, we designed a model system with a large concentration of internal structural defects in the form of H-bonded SiOH nests. This high defect-density material was stabilized with trimethylchlorosilane (TMS-Cl), a small silylation agent, resulting in retained microporosity, long-range order and particle morphology after HLW treatment relative to the parent material.¹⁶

This work reports the extension of the concept of zeolite stabilization to catalytically relevant systems by improving the stability of a series of BEA zeolites with varying Al and Brønsted acid site concentrations against hydrolytic destruction. In the aqueous phase, all Brønsted acidic protons are present as hydronium ions (H₃O⁺) that are confined in the nanopores of the zeolite, thus enhancing their catalytic performance compared to homogeneous acids.¹⁷ The disintegration of the framework is then believed to result in the deactivation of the catalyst as the hydronium ion environment

Chapter 4 – Stability of Zeolites in Aqueous Phase Reactions

is changed drastically. While it was initially hypothesized that the concentration of structural defects plays the critical role for the lifetime of these catalysts, the present experiments show conclusively that the overall water concentration in the pores is the decisive element for lattice stability. Reducing the water concentration via hydrophobization or the introduction of a co-solvent then suppresses the framework hydrolysis.

EXPERIMENTAL SECTION

Chemicals. The silylating agent, trimethylchlorosilane (TMS-Cl >99.0%), was obtained from Sigma Aldrich and used as received. Cyclohexanol (Sigma-Aldrich, 99%), cyclohexene (Sigma-Aldrich, 99%, GC-grade), 1,3-dimethoxy-benzene (Sigma-Aldrich, 99%), dichloromethane (Sigma-Aldrich, HPLC grade), and sodium sulfate (Acros Organics, 99%, anhydrous) are used as received without further purification.

H-form BEA zeolites. BEA15 and BEA40, were synthesized according to the procedure reported by Derewinski et al.¹⁸ For the example of BEA15 (Si/Al 15), 260.2 g of tetraethylammonium hydroxide (TEAOH) was added to 39.6 g distilled water (MilliQ) under stirring in a polypropylene beaker. This was followed by the addition of 4.57 g sodium aluminate and subsequent stirring at room temperature until a clear solution was obtained. 50.0 g of Zeosil (175 mp Rhone-Poulenc) was slowly added. The gel was then aged for 24 h at room temperature under stirring, before being placed in a Teflon-lined autoclave. The synthesis proceeded at 150 °C for 40 h under stirring. Upon completion the solution is centrifuged and the white filtrate washed several times with distilled water before being dried in an oven at 80 °C overnight. The as-made material was calcined at 550 °C for 6 h in synthetic air to remove the template. The calcined Na-form was ion-exchanged with 0.1 M NH₄NO₃ solution for 2 h at 80 °C under rapid stirring conditions. The suspension was then centrifuged and the solid re-dispersed in NH₄⁺ solution and the procedure repeated two more times. Upon completion, the material was dried at 80 °C overnight, before calcining it once more at 450 °C for 6 h in air to yield the H-form. Zeolites, BEA12 and BEA75, were obtained from Zeolyst and Clariant, respectively. BEA12 (Si/Al 12) was provided in the NH₄ form, requiring further calcination, as described above, to obtain the H-form. BEA75 (Si/Al 75) was used without further treatment as provided in the H-form. Defect-free BEA with a Si/Al of 100 was synthesized according to a procedure by Cambor et al.¹⁹ Defect-BEA was obtained by de-boronation as described previously.¹⁶

Silylation. Al-BEA was stabilized using the previously established silylation method for zeolite BEA.¹⁶ In short, the H-form is placed within a quartz tube reactor held inside a tube furnace. N₂ carrier gas (50 ml/min) transports silane vapors to the zeolite bed at reaction temperature. A typical silylation reaction consisted of an activation period, during which the sample was heated, under the flow of N₂, to the desired reaction

Chapter 4 – Stability of Zeolites in Aqueous Phase Reactions

temperature, typically 300 °C, within one hour and then kept at this temperature for two hours. Then, the gas stream was passed through a saturator filled with 5 mL TMS-Cl and allowed to react with the sample for the course of 11 h. The silylated samples were subsequently removed from the quartz tube and used without further purification. *Stability testing.* Zeolites were treated in hot liquid water in Teflon lined batch autoclaves at 160 °C. 300 mg of zeolite and 60 mL deionized MilliQ water (1:200) were added to an autoclave, placed in a rotating oven and kept at 160 °C for 48 h. Upon completion, the cooled suspension was centrifuged and the solid dried at room temperature for 48 h.

Catalysis. The catalytic activity and stability of the materials was tested in aqueous phase cyclohexanol dehydration. In a typical experiment, 80 mL of 0.33 M cyclohexanol solution and 30 mg of catalyst (H-Form or silylated) was added in a Hastelloy PARR reactor, pressurized to 20 bar H₂ and heated to 170 °C. Once the set temperature was reached, stirring (670 rpm) was started and the time was recorded as time zero of the reaction. To quench the reaction, an ice-water mixture was used to rapidly cool the reactor vessel to 4 °C within 10 min. After depressurizing and opening the vessel, the reaction mixture was poured into a separatory funnel and the aqueous portion was extracted five times with a total of 100 mL (20 mL per extraction) of dichloromethane (containing internal standard). The organic phase was dried over Na₂SO₄ and analyzed using an Agilent 7890A GC equipped with HP-5MS 25-m 0.25-um i.d. column, coupled with Agilent 5975C MS. 1,3-Dimethoxybenzene was used as internal standard for identification and quantification of products. A control experiment was performed using 300 mg BEA75 treated with 600 mL 0.33 M cyclohexanol solution at 170 °C (zeolite:H₂O 1:2000) in a Teflon lined 1L autoclave under autogeneous pressure. It was kept at reaction temperature for 27h. Upon completion it was quenched with cold water and the solution was centrifuged. The solid was dried in an oven overnight.

Trickle bed reactor. Zeolite dissolution was probed in a stainless-steel trickle bed reactor (SS316, 3/8 in OD x 0.049 in wall, 12 in length) connected to a single barrel ISCO syringe pump and two cooled collecting vessels that allowed for time-dependent sampling. The reactor was heated with a furnace. The system was kept at the desired pressure using N₂ as inert gas and a backpressure regulator. In a typical reaction, 0.75 g zeolite (40/80 mesh) was suspended in the reactor. The reactor was then pressurized

Chapter 4 – Stability of Zeolites in Aqueous Phase Reactions

to 11 bar N₂, filled with 13 mL distilled water upon which the reactor is heated to 160 °C. Once the temperature was reached, 150 mL H₂O was pumped through the reactor at 10 ml/h. Sampling was conducted every 5h. In order to collect any precipitated SiO₂ in the collecting vessels, 30 mL 0.25 M NaOH was added to the collecting vessel to dissolve any precipitated SiO₂. The resulting solution was then analyzed for Si and Al content via ICP analysis.

Atomic absorption spectroscopy (AAS). The elemental composition of the samples was determined by atomic absorption spectroscopy in a Unicam M Series Flame-AAS equipped with an FS 95 autosampler and a GF 95 graphite furnace.

Helium ion microscopy (HIM). HIM images were obtained using 35 keV He ions with 0.1 pA beam current at normal incidence. Secondary electrons were detected using an Everhart–Thornley detector. For HIM imaging, a very thin layer of carbon (<1 nm) was coated using a carbon sputter deposition system as the samples were completely insulating. The instrument resolution was 0.35 nm.

X-ray diffraction (XRD). XRD patterns were collected on a Rigaku Mini Flex II bench top X-ray diffractometer using a Cu–K α radiation of 0.154056 nm (30 kV and 15 mA). Experiments were conducted on a rotating powder sample holder in a 2 θ range of 5° to 60° with a step size of 0.02 °/s. All measurements were performed under ambient conditions.

N₂-physisorption. The pore size distributions were obtained by N₂-physisorption at 77K in a Micromeritics ASAP 2020 unit. The Tarazona NL-DFT method for N₂ in cylindrical pores without any smoothing, provided by Micromeritics was applied to assess the micropore volume. Single point adsorption close to p/p₀ 0.99 was applied to determine the total pore volume. Select samples also underwent Ar-physisorption at 87K as described in the Appendix.

²⁹Si MAS NMR. The cross-polarization (CP) ²⁹Si MAS NMR experiments were performed using a Varian Inova 89–mm wide-bore 300 MHz NMR spectrometer and a 5 mm HXY MAS Chemagnetics style probe. The following parameters for the cross-polarization pulse sequence were used: the H90 was set to 4 μ s, the contact time was 3 ms and the decoupling field of 62.5 KHz was applied for 10 ms during the acquisition time. The spinning speed was set to 5 kHz. The following parameters were used for a direct-pulse measurement: the H90 was set to 4 μ s, the recycle delay to 60s and the

Chapter 4 – Stability of Zeolites in Aqueous Phase Reactions

number of scans accumulated was 2000. For defect-free BEA the H90 was set to 0.4 μ s and the recycle delay kept at 60s. The number of scans accumulated was 6000.

²⁷Al MAS NMR. The ultrahigh field ²⁷Al MAS NMR experiments were performed on a Varian-Agilent Inova 63 mm wide-bore 850 MHz NMR spectrometer. Experiments were conducted in a commercial 3.2 mm pencil type MAS probe allowing for the use of typically 15 mg of sample. In order to facilitate complete hydration of the sample, they were stored in a desiccator with saturated aqueous Ca(NO₃)₂ solution for 48 h. A single pulse sequence with a pulse length of 0.4 μ s, corresponding to a pulse angle of 45°, was selected for acquiring each ²⁷Al MAS NMR spectrum with a recycle time of 1 s and total accumulation of 5000 scans. The spectra were acquired at a sample spinning rate of 20 kHz \pm 2 Hz and were referenced to 1.5 M Al(NO₃)₃ in H₂O (0 ppm) using the center of the octahedral peak of solid γ -Al₂O₃ (at 13.8 ppm) as a secondary reference. For quantitative measurements, the weights of samples loaded into the MAS rotor were recorded and four spectra were acquired to check the stability of the spectrometer. The matching and tuning conditions of the RF circuit of the NMR probe were set using a network analyzer. All other experimental conditions were kept identical for all analyzed samples. In this way, the absolute peak areas normalized to the external standard (BEA75) were proportional to the Al in the sample. The spectra were analyzed using the MestreNova 8.1 software package.

Infrared (IR) spectroscopy. The samples for IR measurements were prepared as self-supporting discs with a density of approximately 10 mg/cm². Upon loading in the IR-cell, the samples were evacuated to (1.0×10^{-7} mbar) and heated in intervals to 150 °C and 300 °C and kept at 300 °C for 12 h. The heating rate is set to 20 °C/min. Infrared spectra are recorded on a ThermoScientific Nicolette FTIR spectrometer using a MCTA detector with a resolution of 4 cm⁻¹. 128 scans were accumulated for each spectrum. The spectra are normalized to the overtones and combination vibrations of the BEA lattice between 2090 and 1740 cm⁻¹.²⁰ The acidity was probed by dosing the base pyridine onto the sample in a controlled way. The previously activated sample (see above) was allowed to equilibrate with pyridine vapors at 0.1 mbar for one hour at 150 °C before removing all excess physisorbed pyridine via a vacuum pump (1×10^{-4} mbar). Integration of the Brønsted and Lewis peaks (1565–1515 cm⁻¹ and 1470–1430 cm⁻¹ respectively) and using the molar extinction coefficients determined by Emeis²¹ along with the disc weight, the acidity could be quantified.

Chapter 4 – Stability of Zeolites in Aqueous Phase Reactions

Liquid phase adsorption. Uptake of cyclohexanol (q) was determined using liquid ¹H-NMR and water gate suppression at a frequency of 46.2 MHz. Typically, a 0.05 g zeolite (m) sample was immersed in 2 mL of a 0.33 M cyclohexanol solution (c₀) for 24 h at 7 °C, 25 °C and 40 °C. Quantification was accomplished adding an internal standard (trioxane) to the solution at equilibrium (c_e), assuming $q = V \times (c_0 - c_e) \times m^{-1}$. Extrapolation of the measured saturation uptake to reaction temperature of 170 °C was achieved using the linear temperature dependence reported by Liu et al.¹⁷

RESULTS AND DISCUSSION

Characterization of parent Al-BEA

Four different BEA samples with varying Si/Al ratio were investigated in their protonic form. Among these, BEA15 (Si/Al 15) and BEA40 (Si/Al 40) were synthesized based on the procedure described previously,¹⁸ while two commercial samples, Al-rich BEA12 (Si/Al 12) and Si-rich BEA75 (Si/Al 75), were obtained from Zeolyst and Clariant, respectively. All four samples showed X-ray diffraction patterns (Figure A1) typical for the BEA framework along with micropore volumes between 0.23 and 0.25 cm³/g (Table A1). The distribution of the micropore volume shows the typical 0.67 nm pore width for BEA (Figure A2).²² The more aluminous samples BEA12 and BEA15 additionally had a pronounced hysteresis in N₂ sorption, indicating the presence of inter-crystalline mesopores (Figure A3). Examination of these zeolites with He ion microscopy (HIM) confirmed mesoporosity to be a consequence of particle agglomeration (Figure A4). The particle size increased with increasing Si/Al ratio (Figure A5).

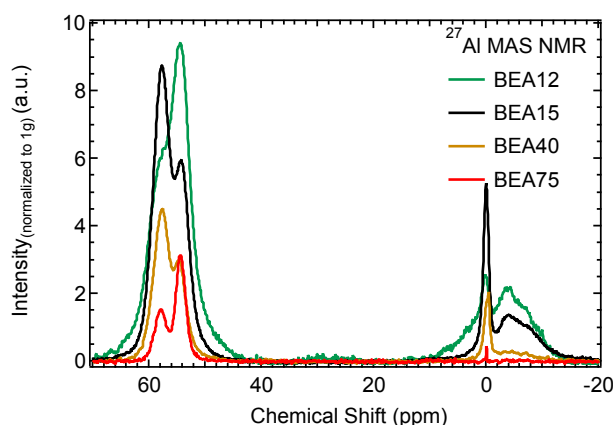


Figure 1. Mass normalized, quantitative ²⁷Al MAS NMR spectra of the investigated Al-BEA samples. The tetrahedral framework Al is represented by the peak between 54-57 ppm with octahedral species appearing between 0 and -10 ppm. Color-coding is reported in the legend.

The concentrations and distributions of Al in the zeolites were determined by ²⁷Al MAS NMR. The combination of high field strength and short excitation pulses enabled the quantitative determination of the Al concentration using an external standard with a known Al concentration (Figure 1).²³⁻²⁴ The accuracy of the method is shown by the good agreement with the total Al determined via elemental analysis (Table A2). The

Chapter 4 – Stability of Zeolites in Aqueous Phase Reactions

narrower line width of the tetrahedral Al^{3+} (Table A2) observed with ^{27}Al MAS NMR for samples with high Si/Al suggests a more homogeneous Al environment than for zeolites of higher Al concentration.²⁵ A significant contribution of octahedral Al (0 – 10 ppm) was observed for BEA12 and BEA15. The six-coordinated, EFAI is hypothesized to be the consequence of exposure to high temperatures during calcination at various stages of preparation and activation, dislodging tetrahedral Al from the framework.^{24,26} The narrow peak at 0 ppm is associated with highly symmetric EFAI such as $\text{Al}(\text{H}_2\text{O})_6^{3+}$, the broad peak at -10 ppm to distorted octahedral Al in small alumina clusters.²⁷ With increasing Al concentrations, the tendency to form EFAI species increased from 2% for BEA75 to 26% for BEA12 (Table A2). Additionally, the concentrations of Al, in Brønsted acid sites (BAS) and Lewis acid sites (LAS), were determined indirectly by IR spectra of adsorbed pyridine, compiled in Table A2.²⁸⁻²⁹ The BAS are a function of the tetrahedral Al in the lattice, while the LAS are related to EFAI. Thus, materials with a higher Al concentration (BEA12 and BEA15) also contained higher concentrations of LAS.

Previous works suggest that various defects in BEA zeolites may promote degradation of the framework and subsequent loss of active sites.⁷⁻⁸ While defect sites may occur through incomplete condensation of the BEA lattice around template molecules,^{19,30} the intergrowth of A and B polymorphs and the resulting interplanar stacking faults additionally cause a sizable concentration of structural defects.³¹⁻³² Cross-polarization (CP) enhanced ^{29}Si MAS NMR was used to probe the presence of defects (Figure 2). Cross-polarization detects indirectly the concentration of protons next to Si.³³ Consequently, Q^2 (-92 ppm) and Q^3 (-103 ppm) peaks, $[\text{Si}(\text{OSi})_2(\text{OH})_2]$ and $[\text{Si}(\text{OSi})_3\text{OH}]$ respectively, are higher in intensity, when cross polarization is used. These peaks represent the structural defects. In addition, the presence of Al which leads to the peak at -106 ppm $[\text{Si}(\text{OSi})_3\text{OAl}]$ ³⁴ adds to the overall Q^3 intensity. Normalization of the spectra to the Q^4 peak $[\text{Si}(\text{OSi})_4]$ allows, therefore, to determine the relative defect concentration.¹⁶ The Q^3/Q^4 ratio was higher for BEA40 and BEA75 samples than for the BEA12 and BEA15 samples, indicating that these high-silica zeolites had larger concentrations of defects.

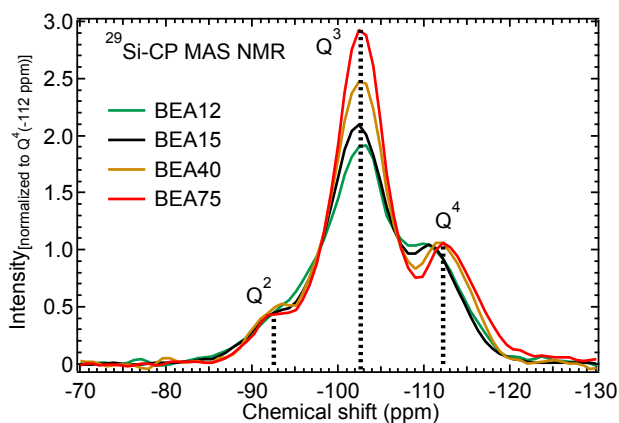


Figure 2. ^{29}Si -CP MAS NMR of BEA in its H-form. The NMR spectra are normalized to the same Q^4 at -112 ppm to qualitatively deduce the amount of SiOH in the samples. Color-coding is reported in the legend.

The different types of SiOH groups were differentiated by IR spectroscopy (Figure 3). The IR spectra (normalized to the combination vibrations of the lattice vibrations $2090\text{--}1740\text{ cm}^{-1}$)²⁰ show the band of the bridging hydroxyl group at 3610 cm^{-1} ,³⁵ isolated SiOH groups at $3730\text{--}3750\text{ cm}^{-1}$,³⁶⁻³⁷ and a broad band at 3500 cm^{-1} attributed to H-bonded silanol nests.³⁸⁻⁴⁰ In such defects several mutually hydrogen-bonded SiOH groups exist. In agreement with ^{29}Si MAS NMR, a higher defect concentration was identified for BEA with higher Si/Al ratios, which also had a weaker SiOHAl band at 3610 cm^{-1} .

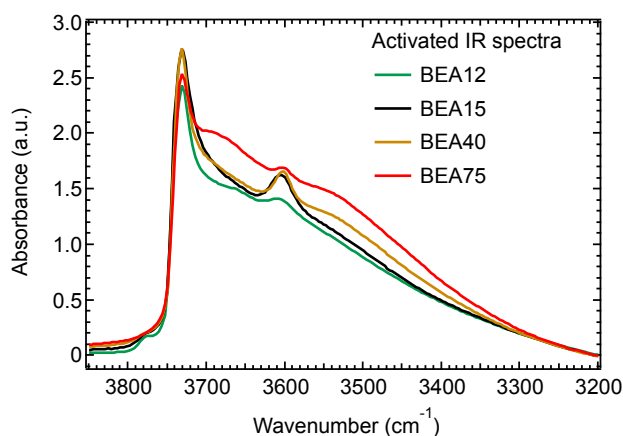
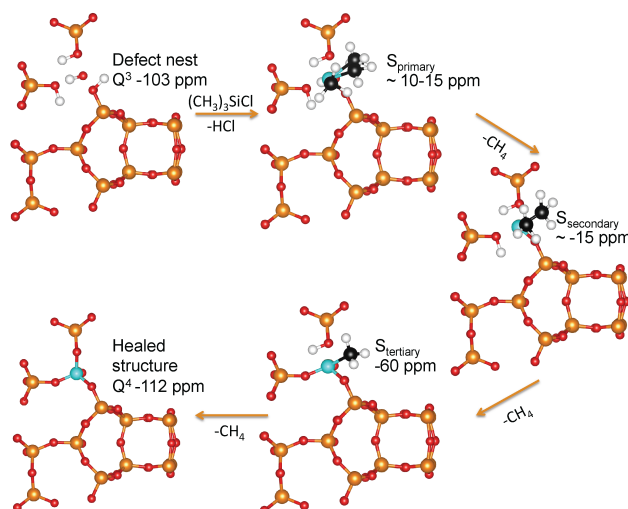


Figure 3. IR spectra of BEA samples. The spectra are normalized to the lattice bands between $2090\text{--}1740\text{ cm}^{-1}$ (not shown). All IR spectra were obtained after activation at $300\text{ }^\circ\text{C}$ overnight to remove residual physisorbed water. Color-coding is reported in the legend.

Chapter 4 – Stability of Zeolites in Aqueous Phase Reactions

The presence of EFAL in clusters, as indicated by the presence or absence of the weak band at 3780 cm^{-1} ,³⁵ was observed in the Al-rich materials but not in the Al-poor BEA samples. This is in agreement with ^{27}Al MAS NMR results showing a higher concentration of EFAl clusters (-10 ppm) for BEA12 and BEA15 (Figure 1, Table A2). The increased concentration of defects in Si-rich materials is related to the fact that in absence of Al the positive charge of the template ions had to be balanced by Si defects, resulting in the incomplete condensation of the framework and generation of defect sites.^{19, 30}

Scheme 1. Silylation via the attack of SiOH in a hydroxyl nest with TMS-Cl. The reaction temperature is $300\text{ }^{\circ}\text{C}$. Reprinted with permission from Proding, S.; Derewinski, M. A.; Vjunov, A.; Burton, S. D.; Arslan, I.; Lercher, J. A. *J. Am. Chem. Soc.* 2016, *138*, 4408--4415. Copyright 2016 American Chemical Society.



Characterization of silylated Al-BEA

Gas-phase silylation⁴¹ has been employed to reduce the concentration of defects in BEA zeolites.^{16, 41} During the process, TMS-Cl reacts with framework hydroxyls capping them, while HCl is released. SiOH groups within close proximity, such as those in silanol nests, are able to react further with the silane through the release of methane, until Si is fully incorporated into the framework (Scheme 1). The removal of these defect sites was shown to reduce the rate of hydrolysis in HLW,¹⁶ and hence hypothesized to extend the catalytic lifetime of the investigated Al-BEA zeolites as well.

Chapter 4 – Stability of Zeolites in Aqueous Phase Reactions

While silylation reduced the microporosity (Table A1), by forming silylation side products (S_{primary} , $S_{\text{secondary}}$ and S_{tertiary}) in the channels (see Scheme 1);^{16, 41} the mesoporosity was hardly changed. BEA15 was an exception as silylation reduced also the mesopore volume, likely due to surface silylation filling the inter-crystalline voids. The silylation process is accompanied by the conversion of some of the tetrahedral Al into octahedral Al (Figure A6). This transformation is caused by HCl, which is produced when TMS-Cl reacts with a hydroxyl group. However, the small concentrations of HCl produced led only to a mild removal of lattice alumina and the migration of alumina clusters to positions outside of the zeolite pores as concluded from the largely retained Al concentration (Table A2).

Changes in the tetrahedral Al due to silylation are also in line with the reduced BAS concentration, attributed to the fact that TMS-Cl reacted also with the bridging hydroxyl groups.⁴² Furthermore, the concentration of accessible LAS decreased, which is attributed to the formation of larger alumina particles consistent with the line broadening of the ^{27}Al MAS NMR peak at 0 ppm, indicating a wider variance of the Al species.

NMR spectra of the silylated materials (Figure 4, top) show that the concentration of defects (-103 ppm) was significantly reduced by silylation in comparison to the parent H-form (Figure 2). The residual concentration of defects is attributed to the incomplete insertion of Si, as deduced from the silylation side products^{16, 41} identified in the low field region of the spectra (20 ppm – -80 ppm). The more intense Q^3 peak for BEA12 and BEA15 is in part attributed to their higher framework Al content.

The difference IR spectra (Figure 4, bottom) also show the effect of silylation. In all samples C-H stretching bands appear at 3000-2800 cm^{-1} ⁴³ attributed to the methyl groups of side products (Figure A7). The largest concentration of methyl groups was found with BEA15 in agreement with the substantial silylation of intercrystalline void spaces indicated by the reduced mesoporosity (Table A1).

The band for the isolated SiOH groups (3735 cm^{-1}) was largely removed. In parallel, the bands of the H-bonded silanol nests (3500 cm^{-1}) were also reduced in intensity, most prominently for BEA75. The SiOHAl groups (3610 cm^{-1}) were reduced in concentration, but still present after silylation as verified by the partial retention of Brønsted acidity (Table A2). Thus, we conclude that the silylation is a possible pathway to reduce the concentration of SiOH groups, the silane preferentially removing internal

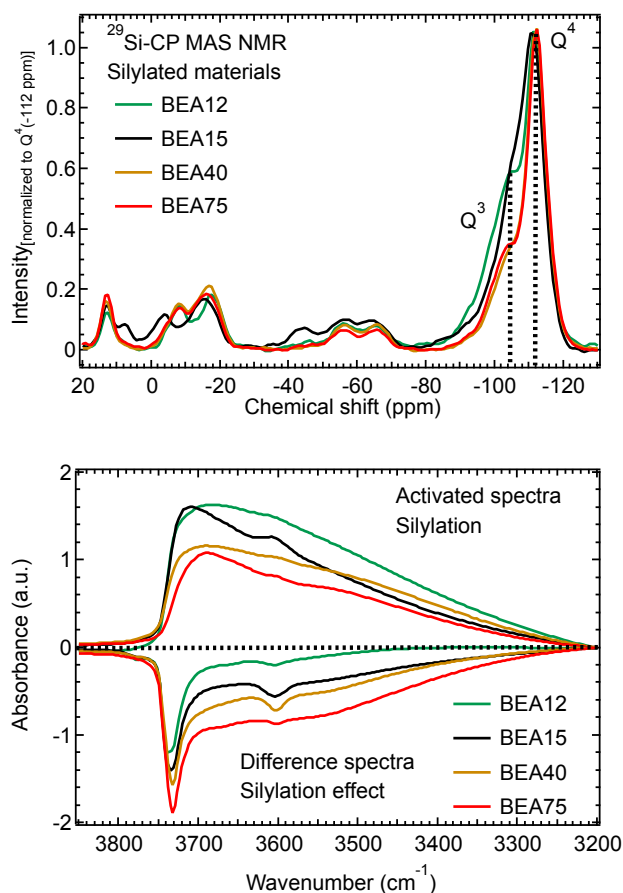


Figure 4. ^{29}Si -CP MAS NMR (top) and infrared (bottom) spectra of Al-rich materials. The NMR spectra are normalized to the same Q^4 as in Figure 2. The peaks between 20 and -80 ppm are assigned to various silylation side products, involving surface species, see also Scheme 1.¹⁶ The IR spectra are normalized to the lattice bands between 2090 - 1740 cm^{-1} (not shown). Difference spectra are obtained with spectral subtraction of silylated samples from parent samples. All IR spectra were obtained after activation at $300\text{ }^\circ\text{C}$ overnight to remove residual physisorbed water. Color-coding is reported in the legend.

H-bonded SiOH nests and isolated SiOH found at intergrowth regions between polymorphs A and B, both of which are associated with the framework instability.³¹⁻³² At the same time, surface hydrophobization also occurred as evident from the lack of external SiOH (3745 - 3750 cm^{-1}) after silylation.

Stability of zeolites in pure water

Chapter 4 – Stability of Zeolites in Aqueous Phase Reactions

In line with previous findings, the presence of lattice defects resulted in pronounced disintegration of the zeolite framework after exposure of the material to pure hot liquid water.¹⁶ The rate of dissolution, as assessed in a trickle bed reactor, was shown to be higher for BEA75 than BEA12, owing to the larger concentration of defects in the high-silica BEA75 (Figure A9). Accompanying the dissolution was a loss of apparent crystallinity and microporosity (Figure A1 and Table A1 respectively). The rates for Si and Al leaching also clearly establish desilication to be the favored pathway of framework degradation.

Silylation prevents framework degradation by capping and removing structural defects, as seen by the retained XRD intensities and microporosity (Figure A1 and Table A1). Interestingly, the effectiveness of the silylation treatment on framework stability was reduced for BEA40 and BEA75, as both the untreated and silylated counterparts show a marked decrease in XRD peak intensity and porosity (Figures A1 and Table A1).

Stability of zeolites during catalysis

The stability of zeolites was also explored during aqueous phase cyclohexanol dehydration. The reaction leads to 99% cyclohexene and 1% dicyclohexyl ether when catalyzed by HBEA zeolites.¹⁷ The mass specific initial rates of cyclohexene formation, turnover frequencies (TOF) and the turnover number (TON), i.e. the number of cyclohexanol molecules converted per acid site until it is deactivated, are reported in Table A3. As HBEA degrades in water, the rate of conversion slows down with time, and depending on the amount of HBEA used, may even stop before reaching equilibrium conversion (i.e. 87% at 200 °C, see also Figure A8).¹⁷ The formation of coke is excluded as a possible cause for deactivation as coke precursor is typically formed via the oligomerization of olefins at high conversions (>70%). Moreover, with BEA15 as an example, the carbon balance at the end of its lifetime remained close to those at shorter reaction times (Figure A10), confirming that there is no continuous formation of coke and thus the deactivation is not due to coke formation.

Instead, the deactivation should be interpreted as the result of the zeolite dissolution initiated by the hydrolysis of Si-O-Si bonds and the gradual collapse of the framework. The solubility of amorphous SiO₂ at reaction temperatures (ca. 680 mg/L)⁴⁴ allows for complete dissolution of the zeolite during the aqueous phase reactions of cyclohexanol

Chapter 4 – Stability of Zeolites in Aqueous Phase Reactions

(1:2600). This was verified with a larger scale control experiment for BEA75 simulating conditions for catalysis, where 94 % of the zeolite was dissolved after 27 h. The catalyst was completely deactivated at this point, as indicated by the cyclohexanol conversion seen in Figure A8. The residual material was investigated with He ion microscopy and X-ray diffraction (Figure A11 and A12), showing no amorphous domains. Instead a narrow peak at 2θ 18° was observed, tentatively attributed to a clay material.⁷

The catalytic activity of hydronium ions for cyclohexanol dehydration is 20 times lower in homogeneous aqueous solution than in BEA pores.¹⁷ In addition, the concentration of hydronium ions generated from water dissociation is not sufficient to catalyze the reaction at detectable rates. As a result, the structural degradation could lead to a loss of confinement for hydronium ions, consequently decreasing the activity by at least one order of magnitude. That is, we believe, the major explanation for the observed decay (virtually flat after complete degradation, see the conversion-time profile in Figure A8). Alternatively, the dissolution and collapse of the aluminosilicates structure could lead to a compensation of the framework charge without the formation of hydronium ions, as well as the blocking of access sites by hydrolyzed silica species.

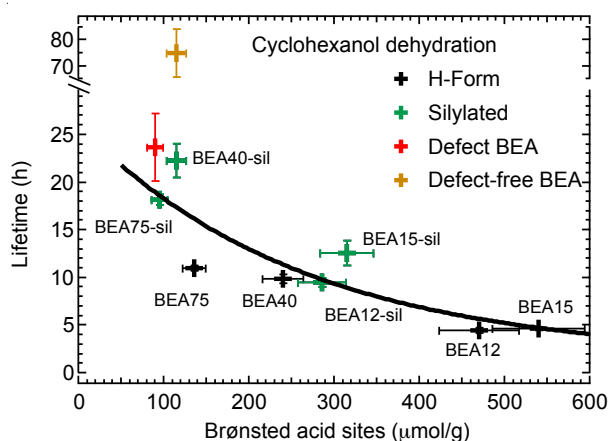


Figure 5. Correlation between the lifetime of a BEA catalyst and the concentrations of Brønsted acid sites during catalysis. This correlation is established for the dehydration of an aqueous solution of cyclohexanol at 170 °C and 30 mg BEA.

Figure 5 compiles the lifetime as a function of the BAS. The catalyst lifetime was derived from the apparent exponential decay function describing the conversion-time profile in Figure A8. Surprisingly, the catalyst lifetime during cyclohexanol dehydration did not generally track the concentration of defects in any monotonous

Chapter 4 – Stability of Zeolites in Aqueous Phase Reactions

way. While high-silica materials (BEA40 and BEA75) contain higher defect concentrations, as deduced from both ^{29}Si MAS NMR and IR spectroscopies, they show longer lifetimes than the Al-rich BEA12 and BEA15 samples. Conversely, the reduced defect concentration upon silylation did yield more stable catalysts as indicated by the improved lifetime (compare green and black symbols in Figure 5). However, there is a good correlation between the lifetime (during catalysis) and the concentration of Brønsted acid sites for all the studied samples. In general, a decrease in Brønsted acid site concentration leads to a longer lifetime and a higher TON (Table A3). The scatter is somewhat more pronounced in the high-silica region where defects appear to be an additional factor impacting the lifetime. Comparing BEA75-sil and BEA40-sil with BEA75, all three samples have similar BAS concentrations, yet only the silylated, low-defect materials exhibited significantly longer lifetimes. The question arises now, to what extent the concentration of aluminum in the lattice (determining the concentration of BAS/hydronium ions) and the defects determine the lifetime of the working catalyst. To accurately deconvolute the roles of defects and BAS on the stability, we additionally investigated two BEA zeolites with a comparable BAS concentrations but very different defect concentrations, respectively. The defect-free BEA was synthesized in fluoride media,¹⁹ whereas the defect-BEA was obtained via de-boronation of a B-BEA.^{16, 45} Both materials are well defined, (see Appendix Note 3 for additional characterization and information). The significance of defects at low BAS concentrations becomes clear when testing these materials. The defect-free BEA, owing to its pristine nature, has an extraordinarily long lifetime while the defect BEA enriched in internal structural defects has a much shorter lifetime in the aqueous phase test reaction. The longer lifetime, compared to BEA75, is attributed to the larger particle size.

Having established that the concentration of defects does not determine the rate of catalyst deactivation for most samples, it is important to understand, how the concentration of Brønsted acid sites influences the conditions in the zeolite pores to favor lattice hydrolysis. We measured, therefore, the micropore uptake of cyclohexanol from an aqueous solution as a function of the BAS.

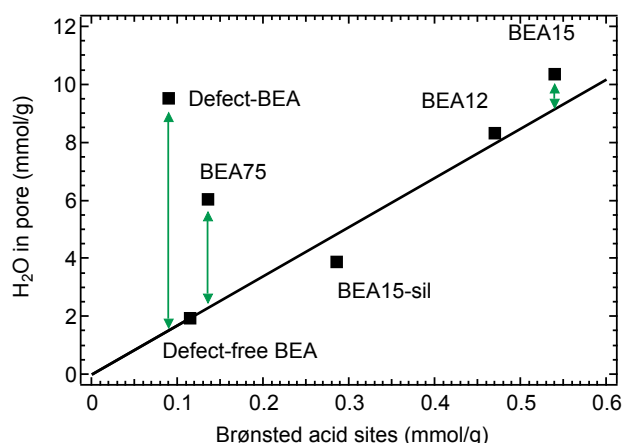


Figure 6. The estimated water concentration in the zeolite micropores as determined from measuring the uptake of cyclohexanol in an aqueous solution at room temperature. The bulk concentration was 0.33 M cyclohexanol in H₂O. Note the linear correlation between Brønsted acid concentration and water uptake. Any upward deviation is linked to adsorption on defect sites, shown by green arrows.

This allowed us to indirectly estimate the concentration of water in the pores,¹⁷ correlating linearly with the BAS concentration (Figure 6).

Defect-free BEA, is the benchmark for the linear correlation between intraporous water and BAS concentration, amounting to roughly 17 H₂O molecules per Brønsted site. Any upwards deviation from this line is attributed to the adsorption of water molecules on internal defect sites. Terminal SiOH found on the external surface area as possible adsorption sites are excluded on the basis of the measured water uptake only being determined for the micropore volume. Using ²⁹Si MAS NMR it was possible to determine the defect concentration for both the defect BEA and defect-free BEA (see Appendix for details).⁴⁶⁻⁴⁷ While the defect concentration in defect-free BEA was below the detection limit, the defect BEA sample had a concentration of 1100 μmol/g SiOH. As determined for defect-free BEA, each Brønsted site binds about 17 H₂O molecules which allows us to determine that each defect SiOH binds about 7-8 H₂O molecules. Assuming that all defects bind an equal amount of water, the difference between the linear correlation and measured uptake gives an estimate of the defect concentration. This clearly tracks with the varying degrees of defects established with ²⁹Si-CP MAS NMR and infrared spectroscopy (Figure 2 and 3). Looking at Figures 5 and 6 combined, the rate of catalyst deactivation induced by framework hydrolysis varied sympathetically with the concentration of water in the pores. The amount of water

Chapter 4 – Stability of Zeolites in Aqueous Phase Reactions

available to facilitate framework hydrolysis is determined primarily by BAS. Only when the concentration of BAS is small, does the water adsorbed on defect sites and hence the number of defects, play a significant role in the lifetime of a catalyst. This begs the question how the apparent influence of the local concentration of water in the pores on the lattice integrity is related to that of the water in the bulk. In an equilibrated system, the rate of framework dissolution should be a function of the chemical potential of water, which in turn must be equivalent in and out of the zeolite pores. Thus, we conclude that either (i) the stabilization of water in the hydronium ion hydration shell changes the chemical potential of water attacking the silica lattice, or (ii) that the hydronium ions themselves are involved in the lattice degradation or (iii) that water diffusion into the pores plays an important role. We tend to rule out hydronium ions in playing a role in the framework degradation, beyond providing part of required water, as the observation of extensive framework decay was observed in a model system containing only traces of Al.¹⁶

In summary, different observations with respect to the stability of zeolites have arisen from testing in pure hot liquid water and in the presence of organic molecules (Figure 7). Conceptually, water in the pore, the concentration of which is primarily affected by the number of hydrophilic framework Al sites, hydrolyzes the lattice Si-O tetrahedra. The defect sites, on the other hand, mainly serve as the location for the hydrolysis to be initiated. The lack of a general correlation between defect concentration and catalyst lifetime assessed under reaction conditions appeared at first to challenge the previously held notion that defects determine the stability of zeolites. However, the shift in the major descriptor for zeolite stability, from structural defects in pure liquid water to BAS concentration in aqueous-organic mixtures, can be explained by considering that in the presence of the organic molecules, the variation in the intraporous water concentration among Al-rich and Al-poor samples is much more pronounced (i.e., enhanced hydrophobicity conferred by the less polar guest molecule) than in the pure liquid water, rendering the role of defects secondary or minor. The higher affinity of zeolites with lower BAS concentrations for cyclohexanol leads to a significantly higher concentration of cyclohexanol in the pores compared to the bulk, which at the same time reduces the intraporous water concentration. Thus, longevity of the catalyst can be achieved, as the intraporous water concentration is minimized.

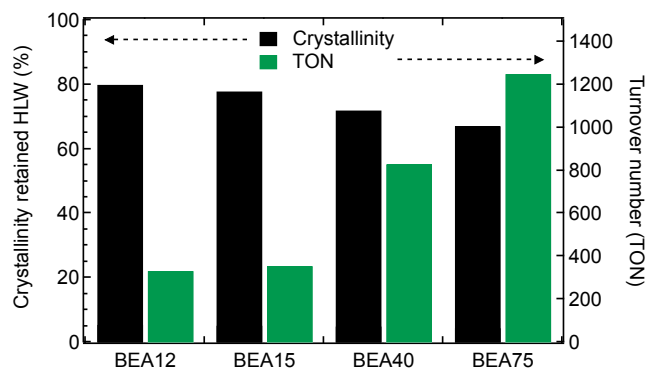


Figure 7. A comparison between the zeolite stability in pure hot liquid water (assessed by retained crystallinity) and for aqueous phase catalysis (i.e. TON) shows opposite trends for the investigated parent BEA zeolites. The high affinity of BEA40 and BEA75 for cyclohexanol leads to a stabilization effect, compensating for the instability caused by structural defects.

CONCLUSION

The stability of zeolite catalysts in aqueous phase reactions is primarily determined by the concentration of water in the pores, controlled by the concentration of hydrated hydronium ions. Reducing the concentration of water significantly decreases the rate of framework hydrolysis and prolongs so the usable lifetime of a zeolite. The concentration of defect sites is only important at low concentrations of hydronium ions. This points to self-limiting processes, as the distribution of water and organic substrates and the presence of hydrolyzed silica species dramatically reduces the available mobile water molecules for continued hydrolysis. The current conclusions reached are in stark contrast to the stabilities in pure HLW. Under such circumstance defects determine the rate of hydrolysis. We tend to rule out hydronium ions as indispensable, directly catalytically active species for hydrolysis, because despite low concentrations of hydronium ions in aluminum free molecular sieves high rates of dissolution were observed.¹⁶

These results show that successful zeolites for organic reactions in water should have a low concentration of Brønsted acid sites together with a low concentration of defect sites. Reactions should be preferentially conducted under conditions that maximize concentrations of organics in zeolite pores.

Chapter 4 – Stability of Zeolites in Aqueous Phase Reactions

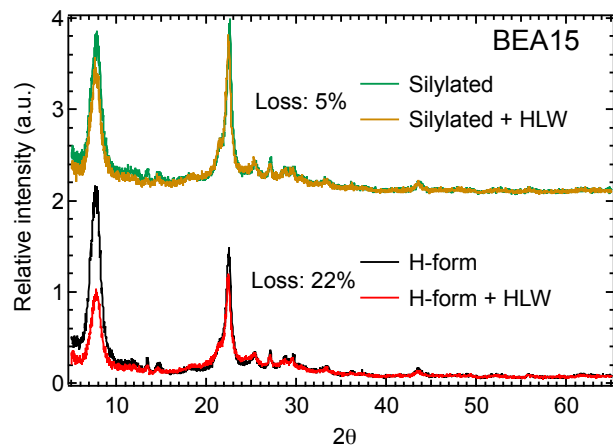
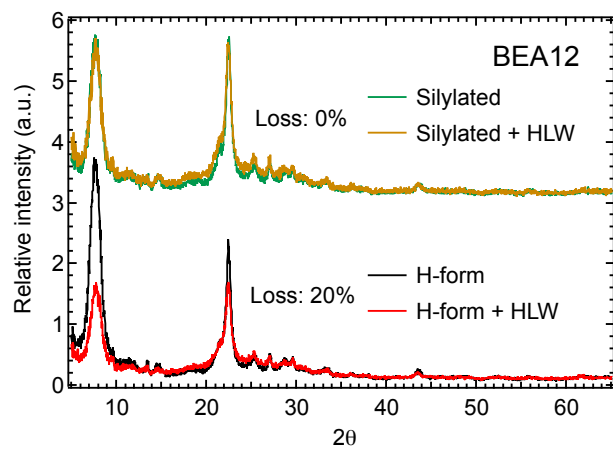
ACKNOWLEDGMENT

B.W. Arey is acknowledged for the He ion micrographs, M. Neukamm and T. Lemmon are recognized for their contribution with AAS and ICP, respectively. The high field NMR experiments and He ion microscopy were performed at the Environmental Molecular Science Laboratory, a national scientific user facility sponsored by the DOE Office of Science, Office of Biological and Environmental Research, located at Pacific Northwest National Laboratory (PNNL), a multiprogram national laboratory operated for DOE by Battelle.

This work was supported by the US Department of Energy, Office of Science, Office of Basic Energy Sciences and by the Materials Synthesis and Simulation Across Scales (MS³ Initiative) conducted under Laboratory Directed Research & Development Program at PNNL.

APPENDIX

X-ray diffraction



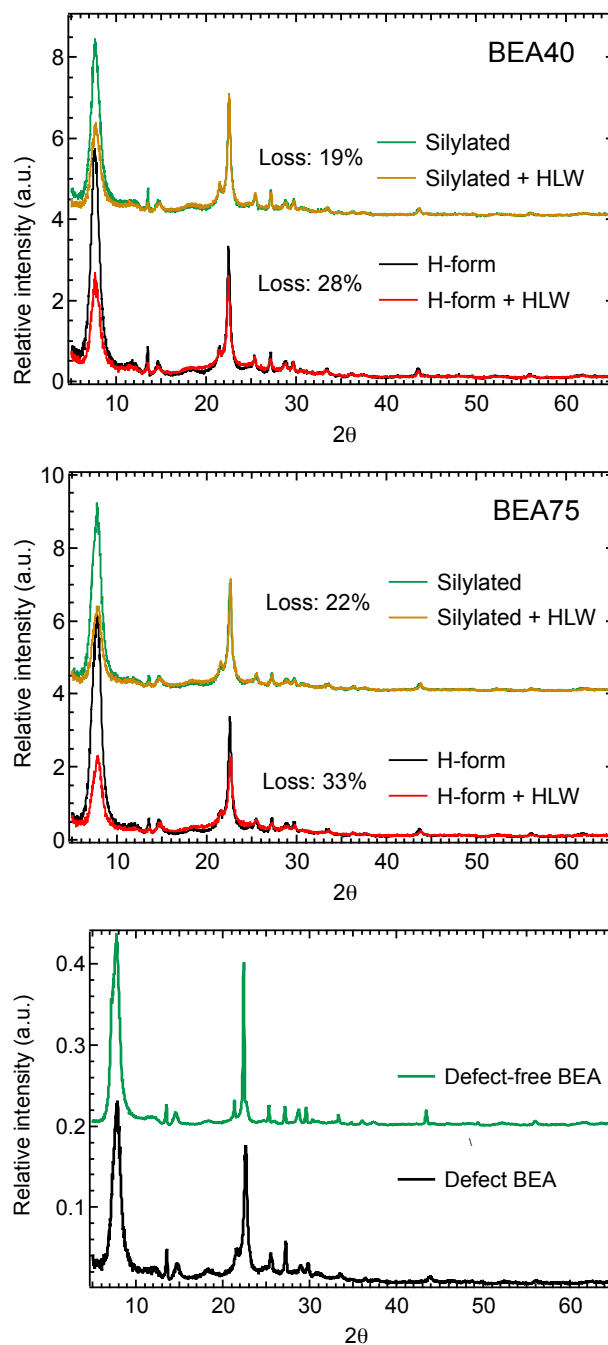


Figure A1. X-ray diffractograms of parent and silylated BEA before and after the interaction with hot liquid water for extended periods of time. Notice, that the integrity of the framework, as measured by the loss in peak area denoted in the legend, suffers extensively in the parent materials compared to the silylated version. Diffraction peak areas were calculated using simple peak fitting. The diffractograms for the defect-BEA and defect-free BEA are also presented, both show reflections attributed to the BEA framework.

N₂ physisorption

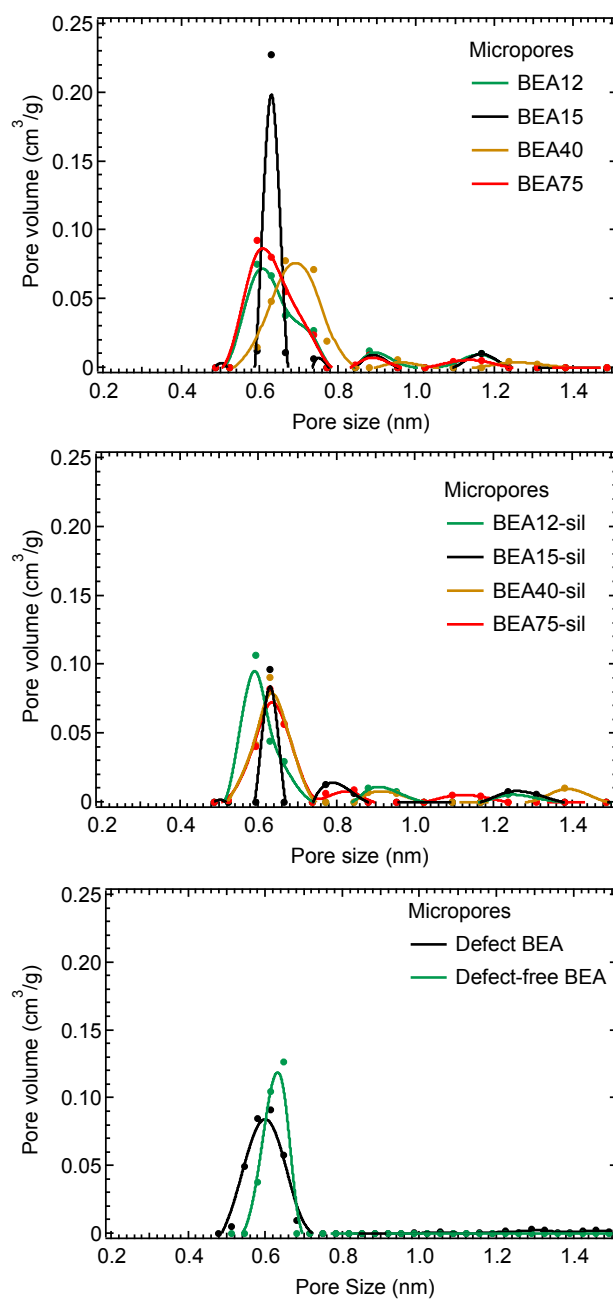
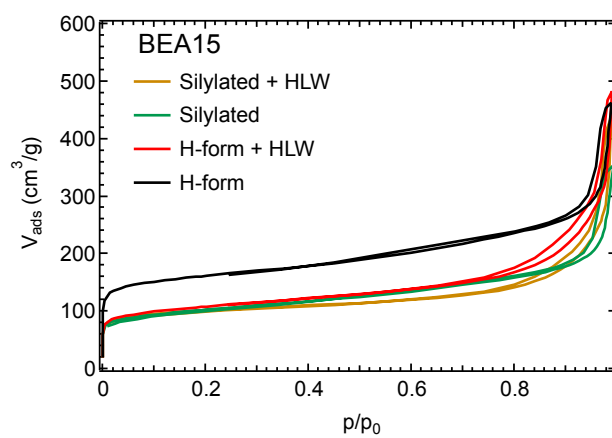
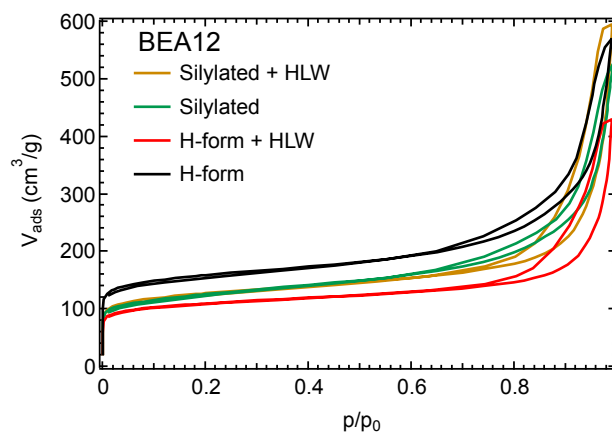


Figure A2. Micropore size distribution for the parent and silylated materials. In the parent materials, there is no clear trend observable. Silylation leads to a reduction of the micropore volume due to the deposition of side products.

Chapter 4 – Stability of Zeolites in Aqueous Phase Reactions



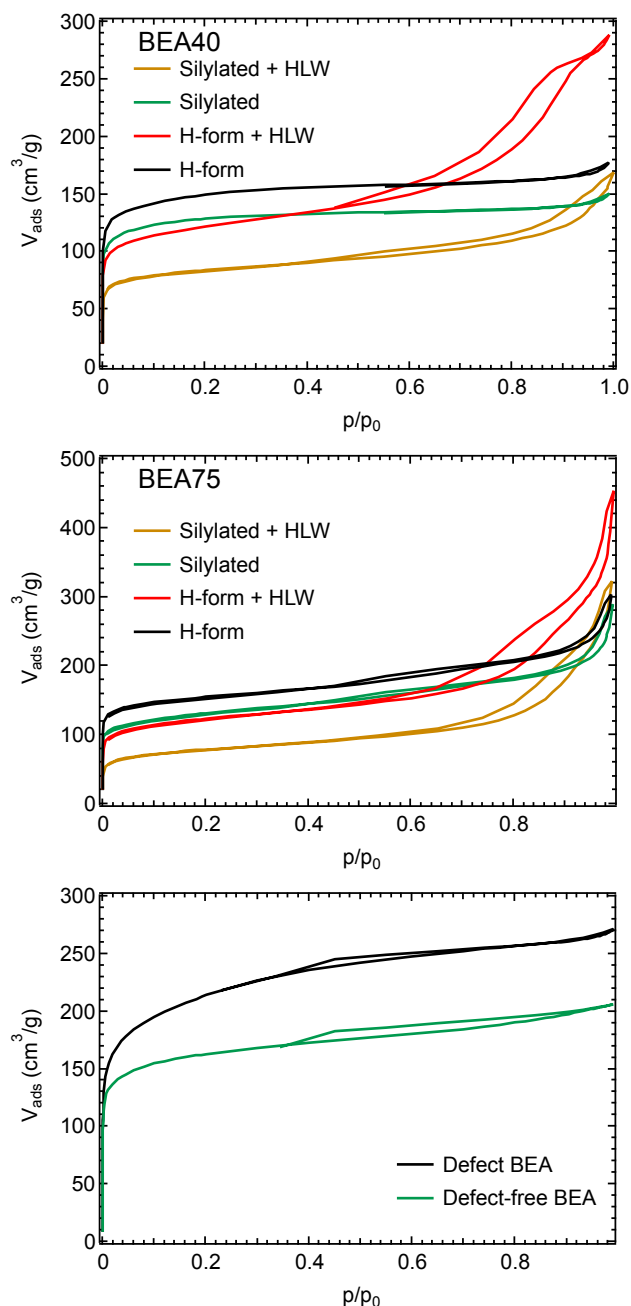


Figure A3. N_2 -physorption isotherms for parent and silylated materials before and after water-treatment. Retention of microporosity upon HLW-treatment is an indicator for stability and can be observed for BEA12 and BEA15 after silylation. BEA40 and BEA75 have an increased mesopore contribution after HLW-treatment due to excessive desilication. At the bottom Ar-physorption isotherms for defect BEA and defect-free BEA are shown. The corresponding pore volumes are reported in Table A1.

Chapter 4 – Stability of Zeolites in Aqueous Phase Reactions

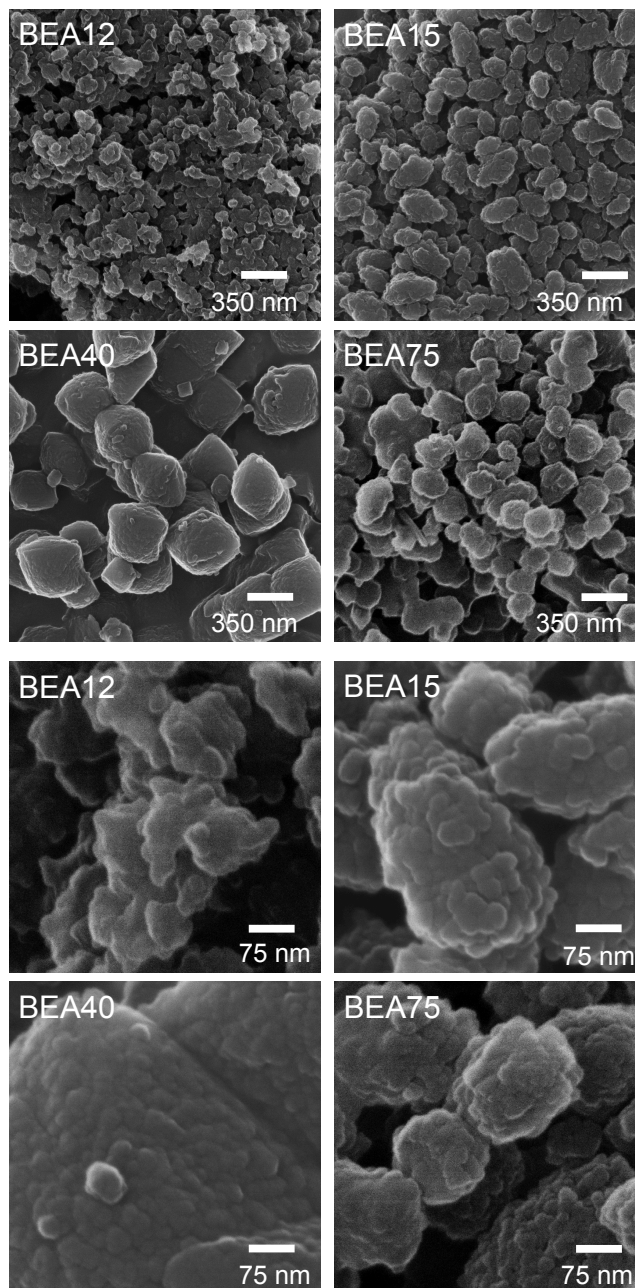
Table A1. BEA samples and their porosities as determined with N₂-physisorption. Total pore volume is determined with single point adsorption close to $p/p_0 = 0.99$. Retention of microporosity after water-treatment is a measure of stability.

Sample	Micropore volume [cm ³ /g] DFT	Mesopore volume [cm ³ /g]	Total pore volume [cm ³ /g]
BEA12	0.23	0.62	0.85
BEA12 + HLW	0.17	0.47	0.64
BEA12-sil	0.18	0.64	0.82
BEA12-sil + HLW	0.18	0.73	0.91
BEA15	0.25	0.48	0.73
BEA15 + HLW	0.13	0.61	0.74
BEA15-sil	0.12	0.42	0.54
BEA15-sil + HLW	0.13	0.53	0.68
BEA40	0.23	0.04	0.27
BEA40 + HLW	0.18	0.30	0.44
BEA40-sil	0.20	0.03	0.23
BEA40-sil + HLW	0.10	0.16	0.26
BEA75	0.25	0.21	0.46
BEA75 + HLW	0.14	0.49	0.64
BEA75-sil	0.15	0.30	0.45
BEA75-sil + HLW	0.09	0.40	0.48
Defect BEA*	0.30	0.05	0.35
Defect-free BEA*	0.28	0.02	0.30

*Samples were measured with Ar-physisorption at 87K.

Chapter 4 – Stability of Zeolites in Aqueous Phase Reactions

Helium Ion Microscopy



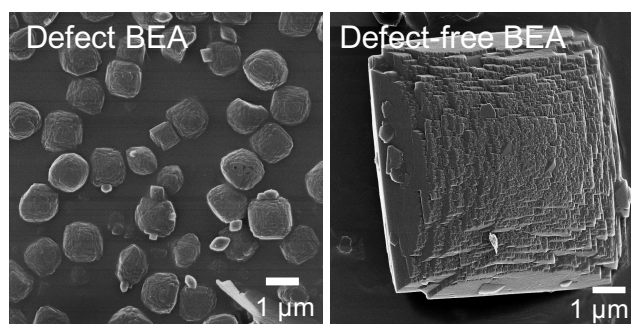


Figure A4. He ion micrographs of BEA samples in their parent form as well as the defect BEA and defect-free BEA. The respective samples are denoted in the legend. Note the much larger particle size of both the defect BEA and defect-free BEA samples.

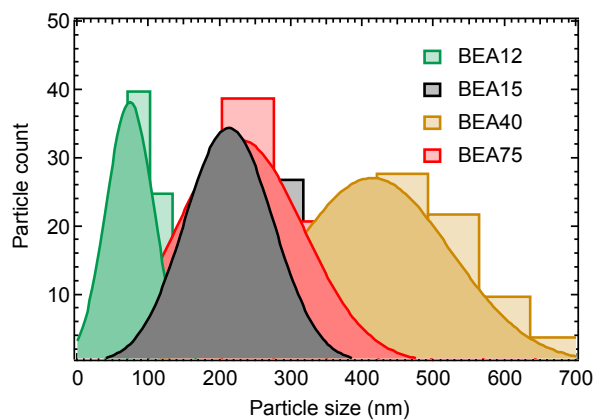


Figure A5. Particle size distribution showing the changes in size as a function of the Si/Al ratio and synthesis method. This is obtained by optically counting and measuring the size of 100 particles. Color-coding is reported in the legend. A Gaussian bell curve is used as a fitting function

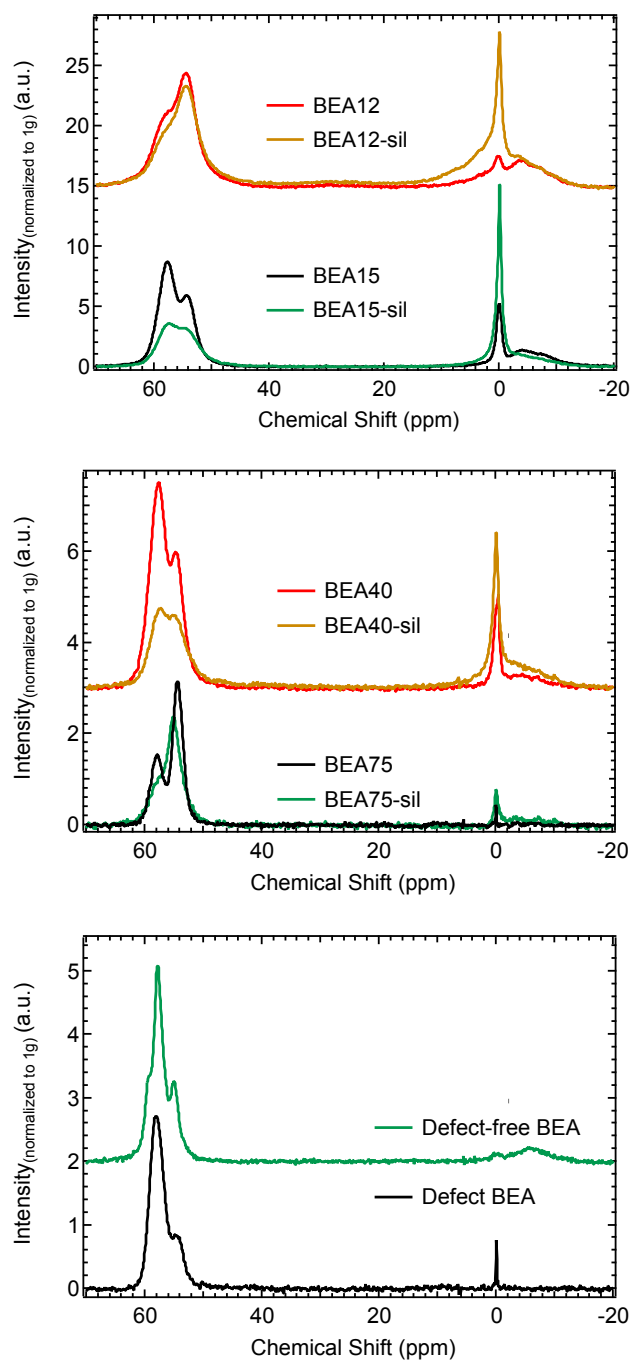
^{27}Al MAS NMR and Py-IR quantification

Figure A6. Mass normalized ^{27}Al MAS NMR spectra of parent and silylated materials. The tetrahedral framework Al is represented by the peaks between 54-57 ppm with octahedral species appearing between 0 and -10 ppm. Silylation leads to a selective transformation from tetrahedral Al to octahedral EFAI. At the bottom, defect-free BEA and defect BEA

Chapter 4 – Stability of Zeolites in Aqueous Phase Reactions

are displayed. Both have only traces of octahedral Al in line with the observations made for the remaining Al-BEA materials. Only the central band is shown.

Table A2. Quantitative analysis of ^{27}Al MAS NMR analyzing the relative distribution of tetrahedral Al^{3+} (IV) and octahedral Al^{3+} (VI) species as well as the total Al concentration (determined by integrating both central and spinning side bands). Additionally, quantitative data of Brønsted and Lewis acidity is also presented. The relative contribution of EFAl and LAS to the total amount of Al/acid sites is reported in the brackets.

Sample	Si/Al _{AAS}	Al _{AAS} ^{a)} ($\mu\text{mol/g}$)	Al _{NMR} ^{b)} ($\mu\text{mol/g}$)	Tetrahedral Al ³⁺ ($\mu\text{mol/g}$)	Linewidth IV _A /IV _B ^{c)} (Hz)	Octahedral Al ³⁺ ($\mu\text{mol/g}$)	Brønsted acid sites ^{d)} ($\mu\text{mol/g}$)	Lewis acid sites ^{d)} ($\mu\text{mol/g}$)
BEA12	11.9	1340	1190	840	890/1075	310 (26%)	470	475 (50%)
BEA12-sil	12.3	1290	1160	675	1255/1732	475 (41%)	315	250 (44%)
BEA12 + HLW	9.6	1520	1340	1000	1020/930	340 (25%)	505	515 (50%)
BEA15	15.0	1120	910	675	680/750	235 (26%)	540	415 (43%)
BEA15-sil	n/a	n/a	935	485	1045/890	450 (48%)	285	310 (52%)
BEA15 + HLW	n/a	n/a	950	675	985/785	275 (29%)	415	480 (54%)
BEA40	37.8	440	495	400	680/670	95 (19%)	240	120 (33%)
BEA40-sil	40.0	380	460	250	1000/725	210 (46%)	115	100 (46%)
BEA40 + HLW	30.1	505	600	450	490/735	150 (27%)	325	250 (43%)
BEA75	75.0	220	220	215	450/530	5 (2%)	135	32 (19%)
BEA75-sil	n/a	n/a	170	140	640/765	30 (21%)	95	52 (35%)
BEA75 + HLW	n/a	n/a	370	290	735/750	80 (27%)	245	165 (40%)
Defect BEA	150	90	100	97	630/555	3 (3%)	90	20 (18%)
Defect- free BEA	110	165	180	170	490/520	10 (7%)	115	25 (17%)

^{a)} Determined with AAS ^{b)} Determined using an external standard, BEA75 with known Al concentration from elemental analysis (AAS) ^{c)} Linewidth determined by simple line fitting of Al spectra with mixed Lorentzian-Gaussian (L/G 0.5) function. IV_A and IV_B correspond to the peak at 54 and 57 ppm respectively ^{d)} Quantification using pyridine adsorption.

Chapter 4 – Stability of Zeolites in Aqueous Phase Reactions

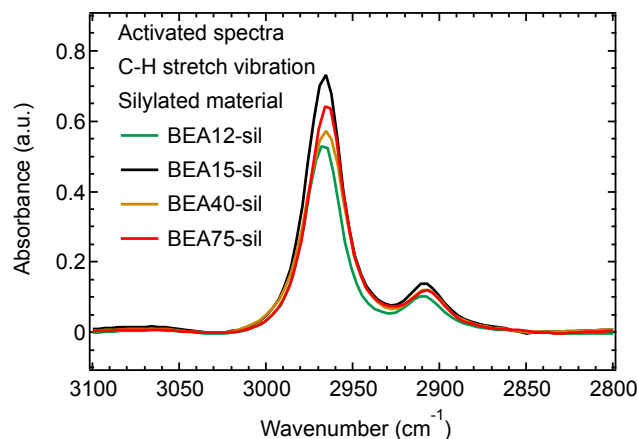
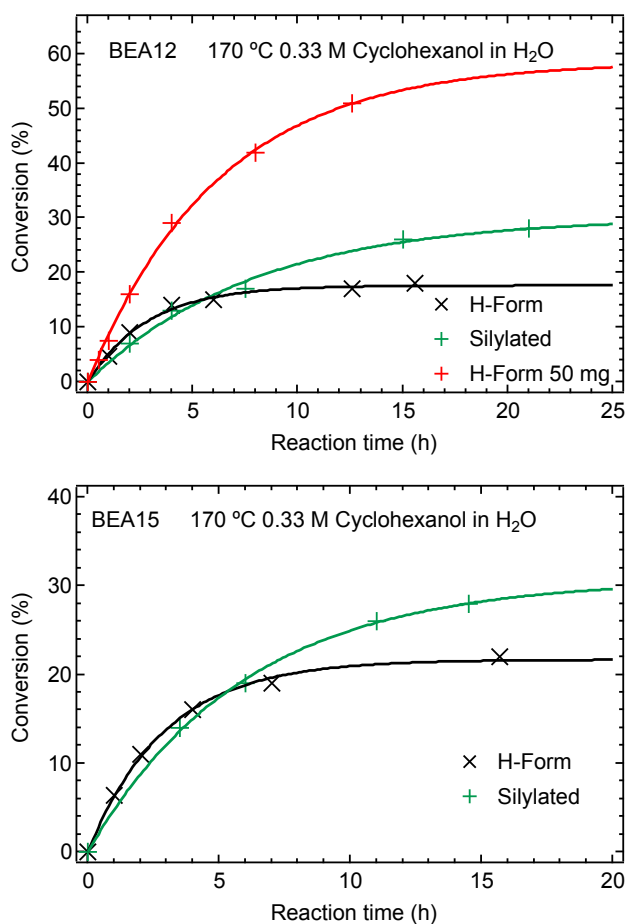


Figure A7. IR spectra of the C-H stretch region for silylated materials. The spectra are normalized to the combination vibrations of the lattice bands between 2090-1740 cm^{-1} (not shown).

Catalysis – conversion plots



Chapter 4 – Stability of Zeolites in Aqueous Phase Reactions

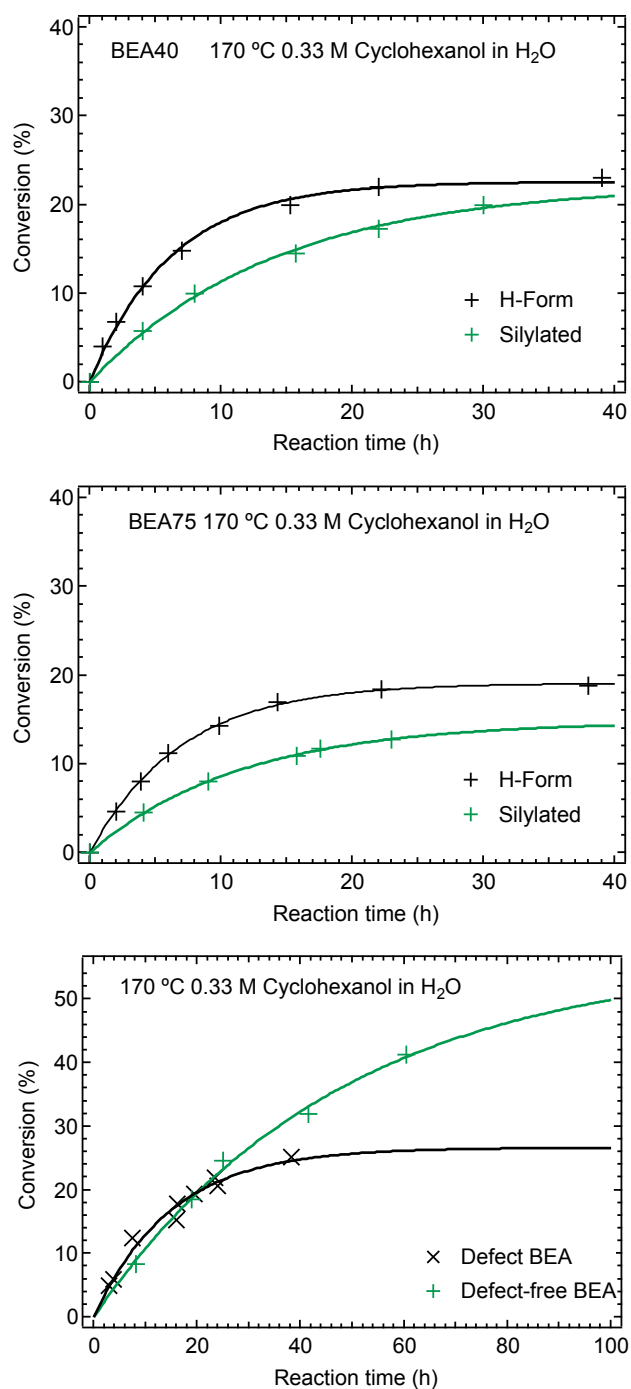


Figure A8. Conversion plots for cyclohexanol dehydration on BEA12, BEA15, BEA40 and BEA75 shown for the parent H-form and silylated materials respectively. Reaction conditions for 30 mg catalyst are reported in the legend. Longer lifetime of silylated materials is evident. Note that using larger amounts of catalyst leads to higher conversion being attained (BEA12 50 mg, red trace, top). This highlights that the conversion of cyclohexanol in the investigated materials is far from equilibrium. While it is likely to be

Chapter 4 – Stability of Zeolites in Aqueous Phase Reactions

less than the 87% reported for 200 °C as mentioned in the main text, this experimental evidence proves the equilibrium conversion to still be high. The conversion for the defect-free BEA and defect BEA are shown at the bottom. Sharing a similar number of active sites, the lifetime and turnover number is determined by the defect concentration, with defect BEA deactivating faster.

Table A3. Derived catalytic properties, i.e. initial rates, turnover frequencies (TOF) and turnover number (TON) for the conversion of cyclohexanol on HBEA zeolite.

Sample	Brønsted acid sites ^{c)} ($\mu\text{mol/g}$)	Rate ^{d)} ($\mu\text{mol}_{\text{Cyclo}}/\text{g}_{\text{BEA}}\cdot\text{s}$)	TOF ($\text{mol}_{\text{Cyclo}}/\text{mol}_{\text{BAS}}\cdot\text{s}$) $\times 10^{-3}$	Turnover number (TON) ($\text{mol}_{\text{Cyclo}}/\text{mol}_{\text{BAS}}$)	Lifetime (h)
BEA12	470	15.1 ± 1.1	32 ± 4.0	330 ± 34	4.5 ± 0.3
BEA12-sil	315	9.3 ± 1.1	29 ± 4.5	845 ± 92	12.6 ± 1.3
BEA15	540	18.0 ± 1.0	33 ± 3.8	355 ± 36	4.7 ± 0.2
BEA15-sil	285	12.6 ± 0.6	44 ± 5.0	950 ± 96	9.5 ± 0.5
BEA40	240	8.9 ± 0.5	37 ± 4.2	830 ± 84	9.9 ± 0.5
BEA40-sil	115	3.9 ± 0.3	34 ± 4.5	1710 ± 182	22.3 ± 1.8
BEA75	135	6.7 ± 0.2	49 ± 5.1	1250 ± 125	11.0 ± 0.3
BEA75-sil	95	3.2 ± 0.1	33 ± 3.5	1375 ± 138	18.2 ± 0.6
Defect BEA	90	4.4 ± 0.4	49 ± 9.0	2620 ± 330	23.7 ± 3.6
Defect-free BEA	115	2.9 ± 0.3	25 ± 3.0	4365 ± 555	75.0 ± 9.4

^{a)} Quantification using pyridine adsorption and desorption at 150°C; Accuracy $\pm 10\%$ ^{b)} Initial rate and TOF of cyclohexene formation and catalyst lifetime determined from fitting the conversion-time plots (Fig A8) for 80 mL 0.33 M aqueous cyclohexanol solution at 170 °C, 20 bar H₂ and 30 mg BEA catalyst with an exponential decay function.

All silylated BEA zeolites deactivated more slowly and converted larger amount of cyclohexanol, as seen by an increased TON for all cases. (Table A3). The reduced micropore volume (Table A1 and Figure A3), induced by the silylation, did not prevent access of the reactant molecules to the active hydronium ions; the TOF changed only marginally.

Appendix Note 1 – Zeolite Degradation

Dissolution rate in pure hot liquid water

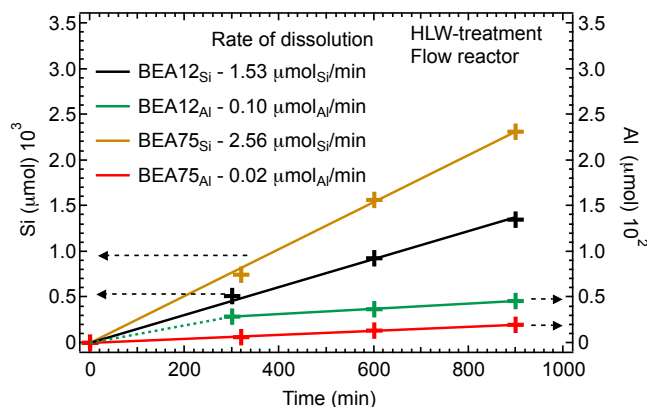


Figure A9. BEA exposed to pure HLW in a trickle bed reactor (200:1, 15h, 10ml/h, 160 °C, 11 bar N₂) elucidated the Si and Al dissolution rates for BEA12 and BEA75. Color-coding and initial rates of Si and Al leaching are reported in the legend.

Deactivation during catalysis

Carbon balance

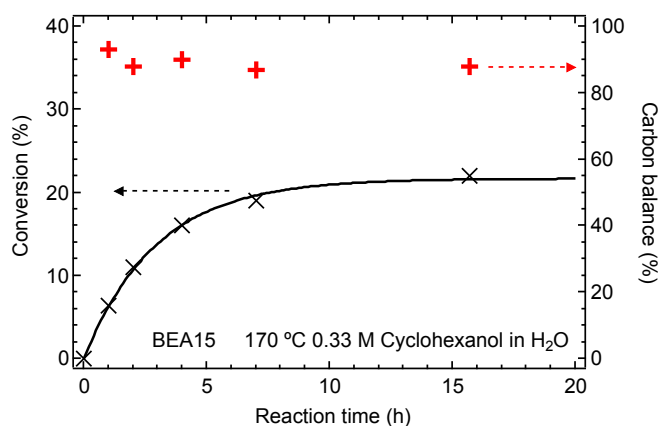


Figure A10. Deactivation of the catalyst during cyclohexanol dehydration and the resultant carbon balance. The carbon balance is less than 100%, due to the formation of volatile cyclohexene as well as uncertainty introducing in the work up procedure. The changes associated with the carbon balance are not significant enough to justify deactivation via coking.

Dissolution of the catalyst

To verify that catalyst deactivation under catalysis conditions occurs via dissolution, a control experiment was conducted with BEA75 using a 0.33 M cyclohexanol solution containing an excessive amount of H₂O compared to the zeolite mass used (2000:1),

able to fully dissolve the zeolite, similar to conditions reported for catalytic testing (2600:1). 94% of the zeolite mass was dissolved while the residual amount was analyzed with X-ray diffraction and He ion microscopy, presented below.

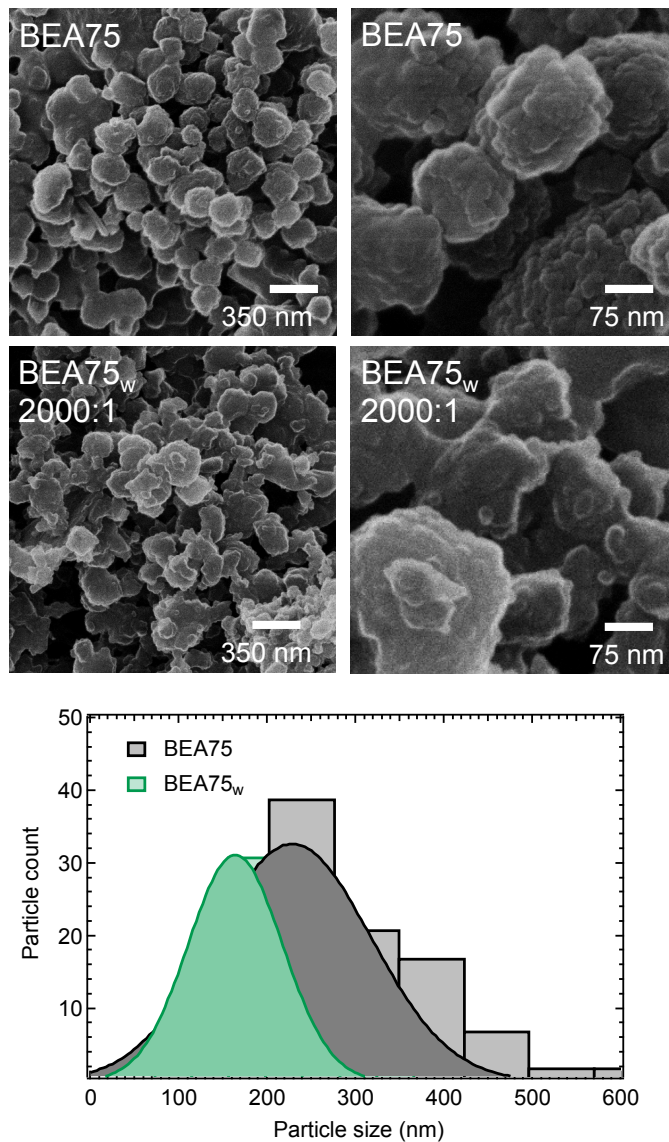


Figure A11. He ion micrographs of BEA75 before and after exposure to excessive amounts of HLW (BEA75_w). Residual zeolite presents smoothed surfaces and less round particle morphology. The particle size is also reduced.

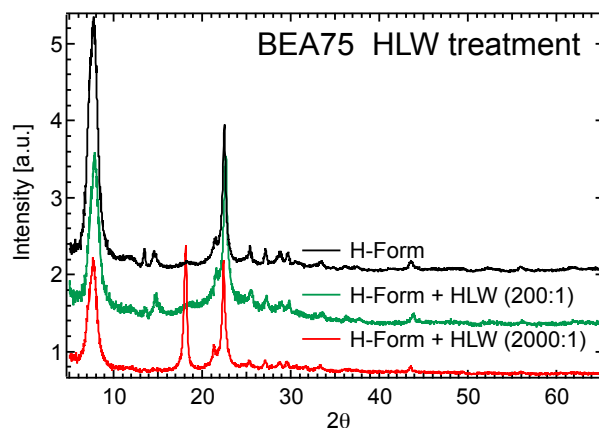


Figure A12. X-ray diffractogram for BEA75 exposed to different amounts of HLW. Conditions typically found for HLW-treatment (200:1) led to partial amorphization due to precipitated SiO₂ (see also Figure A1). Conditions during aqueous phase reactions reported in this publication (2000-2600:1), favor the complete dissolution, with the residual material showing no amorphous component. Instead a reflection at 2θ 18° is observed, tentatively attributed to clay material.

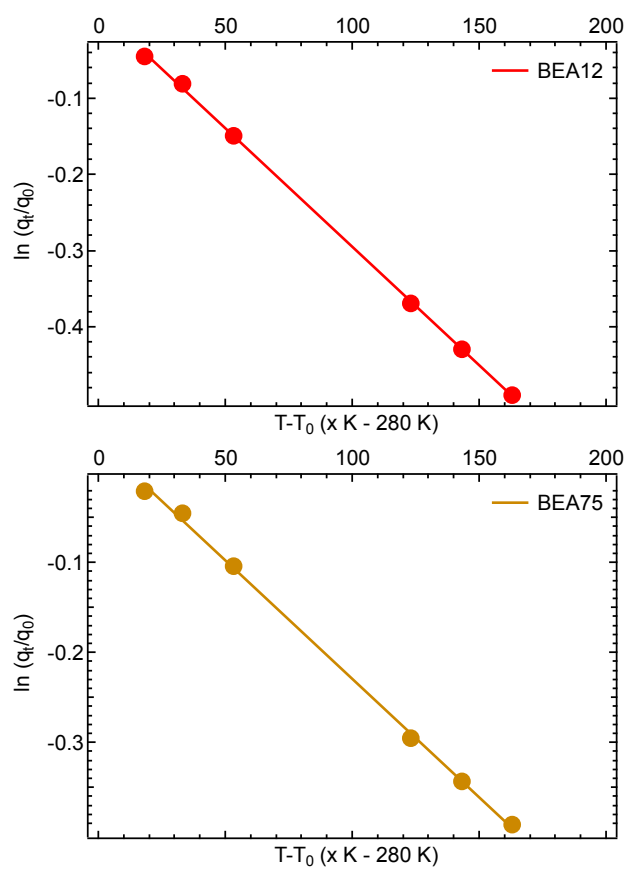
Appendix Note 2 – Liquid phase adsorption

Table A4. Cyclohexanol uptake from a 0.33 M aqueous phase and the corresponding micropore volume occupied by water as measured for room temperature and extrapolated to the reaction temperature of 170 °C. For extrapolation see Figure A13 below. Adsorption of Ar at -186 °C was used to determine the most accurate micropore volume, instead of using the values obtained with N₂ adsorption at -196 °C, shown in Table A1. For BEA15-sil, the accessible micropore volume was determined with gas-phase adsorption of cyclohexanol, which was less than the volume determined with Ar. For all other samples the maximum uptake of cyclohexanol from the gas-phase matched the micropore volume determined with Ar.

Sample	Uptake Cyclohexanol [mmol/g]	Micropore Volume [cm ³ /g]	Micropore Concentration Cyclohexanol [mmol/cm ³]	Uptake H ₂ O [mmol/g]	Micropore Concentration H ₂ O [mmol/cm ³]	BAS [mmol/g]
BEA12 - 25 °C	0.77	0.23	3.35	8.32	36.2	0.470
BEA12 - 170 °C	0.49		2.13	9.93	43.2	
BEA75 - 25 °C	1.54	0.27	5.72	6.03	22.4	0.135
BEA75 - 170 °C	1.06		3.94	8.79	32.7	
BEA15 - 25 °C	0.61	0.25	2.44	10.36	41.4	0.540
BEA15 - 170 °C	0.39		1.57	11.61	46.5	
BEA15-sil - 25 °C	0.75	0.15*	5.06	3.88	26.2	0.285
BEA15-sil - 170 °C	0.49		3.29	5.40	36.5	
Defect BEA - 25 °C	1.23	0.30	4.11	9.53	31.8	0.090
Defect-free BEA - 25 °C	2.33	0.28	8.39	1.95	7.0	0.115

* Deduced from the maximum uptake close to p/p_0 for the gas-phase adsorption of cyclohexanol.

Chapter 4 – Stability of Zeolites in Aqueous Phase Reactions



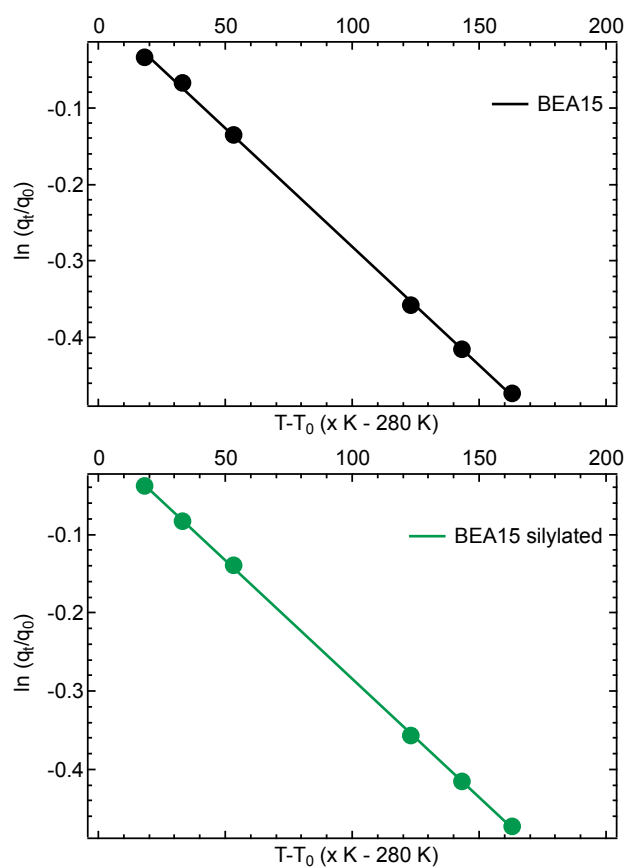


Figure A13. Linearization of the experimentally measured uptakes at low temperatures allows for the extrapolation to reaction temperatures assuming a Langmuir type adsorption process. For more details see Liu, Y.; Vjunov, A.; Shi, H.; Eckstein, S.; Camaioni, D. M.; Mei, D.; Barath, E.; Lercher, J. A. *Nat. Commun.* 2017, (8), 14113.

Appendix Note 3 – Determining the Role of Defects

While it is clearly established that increasing lifetime can be achieved by lowering the Brønsted acid site concentration, the scatter in the low-BAS region suggests that the removal of defects can have a beneficial impact on the lifetime (Figure 5). Therefore, we investigated two additional BEA zeolites. These materials were designed to show the impact of defects, by either having a lot of defects or as little defects as possible. We previously described the generation of a defect-rich model system consisting of the synthesis of a BEA zeolite in hydroxide medium, with boron incorporated. The boron takes the role of the tetrahedral framework unit typically occupied by aluminum. Mild treatment in water resulted in the removal of boron and generation of defect nests. On the other end of the spectrum we synthesized a BEA zeolite in fluoride medium, with a comparable Si/Al and BAS concentration. Fluoride anions have the benefit of compensating the negative framework charge. Therefore the generation of internal defects is avoided. Both materials are pure phase BEA as seen from the X-ray diffractograms in Figure A1. Only a negligible amount of mesopores is observed as the large particles, spanning several micrometers, as seen by He ion micrographs (Figure A4), are isolated without any intracrystalline mesopores. The micropore volume is slightly larger for the defect-BEA owing to the deboronation procedure (Table A1). Only traces of extra-framework octahedral Al are observed (Figure A6). Clearly seen in Figure A8 the defect-free BEA anticipated to have only a negligible concentration of defects shows a superior lifetime, whereas the defect BEA deactivates with time. In respect to the defect concentration, the IR spectra shown below in Figure A14 suggest that defect-free BEA has no isolated or terminal SiOH and a much lower overall intensity in the OH region. Defect-BEA on the other hand, clearly has signals in the SiOH region attributed to isolated SiOH as well as hydrogen-bonded SiOH at 3500 cm^{-1} .

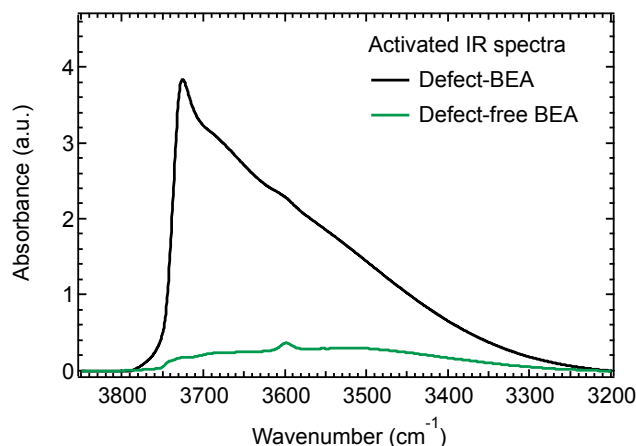


Figure A14. Infrared spectra of both the defect-BEA and defect-free BEA showing the differing degree of hydroxyl groups. The spectra are normalized to the lattice vibrations between 2090-1740 cm^{-1} (not shown).

Furthermore, owing to the small concentration of Al, we could accurately determine the defect concentration for these two materials using ^{29}Si MAS NMR. Rather than the cross-polarization enhanced spectra shown in Figure 2, this quantitative direct pulse measurement allows us to quantify the Q^3 Si. Q^3 Si can either be due to incorporated Al or due to hydroxyl groups connected to the Si, i.e. defect sites. As the particle size is significantly large, the measured SiOH concentration is solely attributed to internal SiOH. Knowing the real concentration of framework Al (e.g. from ^{27}Al MAS NMR) and thus the theoretical amount of Q^3 Si, the difference can be attributed to defects. In principle, this method for determining the defect concentration can be applied to the other investigated materials, however, the increasing concentration of framework Al and the need to deconvolute the spectra leads to a significant degree of inaccuracy. Using this methodology, it is clear that defect-free BEA has no detectable defect concentration as only fully incorporated, Q^4 Si is observed. Defect-BEA on the other hand has a significant Q^3 signal associated with defects. Quantification yielded a concentration of 1100 $\mu\text{mol/g}$ SiOH. The accuracy of this method is $\pm 10\%$. Thus it is established that these two compounds are ideal candidates for the deconvolution of the impact of defect concentration on zeolite stability in aqueous phase reactions. They are free of extra-framework Al, have no significant mesopore contribution, a well-defined BAS concentration as well as defect concentrations on two ends of the spectrum.

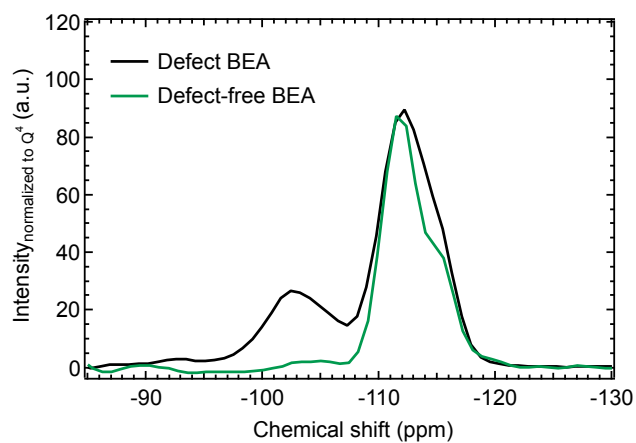


Figure A15. ^{29}Si MAS NMR spectra of the defect and defect-free BEA. The intensity of the Q^3 signal at -103 ppm is related to the defect concentration of the material. Clearly the defect-free BEA has only a strong signal in the Q^4 region, between -110 and -117 ppm. This way of determining the defect concentration holds for materials with high Si/Al ratios as Q^3 due to Al is negligible.

REFERENCES

1. Zhao, C.; Kou, Y.; Lemonidou, A. A.; Li, X.; Lercher, J. A. *Chem. Commun.* 2010, 46 (3), 412-414.
2. Zhao, C.; Camaioni, D. M.; Lercher, J. A. *J. Catal.* 2012, 288, 92-103.
3. Chheda, J. N.; Huber, G. W.; Dumesic, J. A. *Angew. Chem. Int. Ed.* 2007, 46 (38), 7164-7183.
4. Ennaert, T.; Van Aelst, J.; Dijkmans, J.; De Clercq, R.; Schutyser, W.; Dusselier, M.; Verboekend, D.; Sels, B. F. *Chem. Soc. Rev.* 2016, 45 (3), 584-611.
5. Xiong, H.; Pham, H. N.; Datye, A. K. *Green Chemistry* 2014, 16 (11), 4627-4643.
6. Ravenelle, R. M.; Schüßler, F.; D'Amico, A.; Danilina, N.; van Bokhoven, J. A.; Lercher, J. A.; Jones, C. W.; Sievers, C. *J. Phys. Chem. C* 2010, 114 (46), 19582-19595.
7. Vjunov, A.; Fulton, J. L.; Camaioni, D. M.; Hu, J. Z.; Burton, S. D.; Arslan, I.; Lercher, J. A. *Chem. Mater.* 2015, 27 (9), 3533-3545.
8. Zhang, L.; Chen, K.; Chen, B.; White, J. L.; Resasco, D. E. *J. Am. Chem. Soc.* 2015, 137 (36), 11810-11819.
9. Zapata, P. A.; Huang, Y.; Gonzalez-Borja, M. A.; Resasco, D. E. *J. Catal.* 2013, 308, 82-97.
10. Zapata, P. A.; Faria, J.; Ruiz, M. P.; Jentoft, R. E.; Resasco, D. E. *J. Am. Chem. Soc.* 2012, 134 (20), 8570-8578.
11. Ennaert, T.; Geboers, J.; Gobechiya, E.; Courtin, C. M.; Kurttepel, M.; Houthoofd, K.; Kirschhock, C. E. A.; Magusin, P. C. M. M.; Bals, S.; Jacobs, P. A.; Sels, B. F. *ACS Catal.* 2015, 5 (2), 754-768.
12. van Bekkum, H.; Kouwenhoven, H., *Zeolite Manual for the Organic Chemist*. Mijnbestseller. nl: Delft, 2012.
13. Wuyts, S.; De Temmerman, K.; De Vos, D.; Jacobs, P. *Chem. Commun.* 2003, (15), 1928-1929.
14. Wuyts, S.; De Temmerman, K.; De Vos, D. E.; Jacobs, P. A. *Chemistry – A European Journal* 2005, 11 (1), 386-397.
15. Lutz, W.; Toufar, H.; Kurzhals, R.; Suckow, M. *Adsorption* 2005, 11 (3), 405-413.
16. Proding, S.; Derewinski, M. A.; Vjunov, A.; Burton, S. D.; Arslan, I.; Lercher, J. A. *J. Am. Chem. Soc.* 2016, 138 (13), 4408-4415.

Chapter 4 – Stability of Zeolites in Aqueous Phase Reactions

- 17.Liu, Y.; Vjunov, A.; Shi, H.; Eckstein, S.; Camaioni, D. M.; Mei, D.; Barath, E.; Lercher, J. A. *Nat. Commun.* 2017, (8), 14113.
- 18.Derewinski, M.; Fajula, F. *Appl. Catal., A* 1994, 108 (1), 53-61.
- 19.Cambor, M. A.; Corma, A.; Valencia, S. *J. Mater. Chem.* 1998, 8 (9), 2137-2145.
- 20.Jentys, A.; Lercher, J. A. *Stud. Surf. Sci. Catal.* 1989, 46, 585-594.
- 21.Emeis, C. A. *J. Catal.* 1993, 141 (2), 347-354.
- 22.Baerlocher, C.; McCusker, L. B. Database of Zeolite Structures. <http://www.iza-structure.org/databases/> (accessed October).
- 23.Samoson, A.; Lippmaa, E.; Engelhardt, G.; Lohse, U.; Jerschke, H. G. *Chem. Phys. Lett.* 1987, 134 (6), 589-592.
- 24.Fyfe, C. A.; Bretherton, J. L.; Lam, L. Y. *J. Am. Chem. Soc.* 2001, 123 (22), 5285-5291.
- 25.Shi, J.; Anderson, M. W.; Carr, S. W. *Chem. Mater.* 1996, 8 (2), 369-375.
- 26.van Bokhoven, J. A.; Koningsberger, D. C.; Kunkeler, P.; van Bekkum, H.; Kentgens, A. P. M. *J. Am. Chem. Soc.* 2000, 122 (51), 12842-12847.
- 27.Beers, A. E. W.; van Bokhoven, J. A.; de Lathouder, K. M.; Kapteijn, F.; Moulijn, J. A. *J. Catal.* 2003, 218 (2), 239-248.
- 28.Parry, E. P. *J. Catal.* 1963, 2 (5), 371-379.
- 29.Hughes, T. R.; White, H. M. *J. Phys. Chem.* 1967, 71 (7), 2192-2201.
- 30.Cambor, M. A.; Corma, A.; Valencia, S. *Chem. Commun.* 1996, (20), 2365-2366.
- 31.Wright, P. A.; Zhou, W.; Pérez-Pariente, J.; Arranz, M. *J. Am. Chem. Soc.* 2005, 127 (2), 494-495.
- 32.Newsam, J. M.; Treacy, M. M. J.; Koetsier, W. T.; Gruyter, C. B. D. *Proc. R. Soc. London, Ser. A* 1988, 420 (1859), 375-405.
- 33.Sindorf, D. W.; Maciel, G. E. *J. Phys. Chem.* 1982, 86 (26), 5208-5219.
- 34.Hunger, M.; Karger, J.; Pfeifer, H.; Caro, J.; Zibrowius, B.; Bulow, M.; Mostowicz, R. *J. Chem. Soc., Faraday Trans. 1* 1987, 83 (11), 3459-3468.
- 35.Guisnet, M.; Ayrault, P.; Coutanceau, C.; Fernanda Alvarez, M.; Datka, J. *J. Chem. Soc., Faraday Trans.* 1997, 93 (8), 1661-1665.
- 36.Maier, S. M.; Jentys, A.; Lercher, J. A. *J. Phys. Chem. C* 2011, 115 (16), 8005-8013.

Chapter 4 – Stability of Zeolites in Aqueous Phase Reactions

37. Woolery, G. L.; Alemany, L. B.; Dessau, R. M.; Chester, A. W. *Zeolites* 1986, 6 (1), 14-16.
38. Takei, T.; Kato, K.; Meguro, A.; Chikazawa, M. *Colloids Surf., A* 1999, 150 (1-3), 77-84.
39. Krijnen, S.; Harmsen, R. J.; Abbenhuis, H. C. L.; Van Hooff, J. H. C.; Van Santen, R. A. *Chem. Commun.* 1999, (6), 501-502.
40. Holm, M. S.; Svelle, S.; Joensen, F.; Beato, P.; Christensen, C. H.; Bordiga, S.; Bjørgen, M. *Appl. Catal., A* 2009, 356 (1), 23-30.
41. Kraushaar, B.; Van De Ven, L. J. M.; De Haan, J. W.; Van Hooff, J. H. C. *Stud. Surf. Sci. Catal.* 1988, 37, 167-174.
42. Huang, M.; Adnot, A.; Kaliaguine, S. *J. Chem. Soc., Faraday Trans.* 1993, 89 (23), 4231-4237.
43. Mirth, G.; Lercher, J. A.; Anderson, M. W.; Klinowski, J. *J. Chem. Soc., Faraday Trans.* 1990, 86 (17), 3039-3044.
44. Alexander, G. B.; Heston, W. M.; Iler, R. K. *J. Phys. Chem.* 1954, 58 (6), 453-455.
45. Derewinski, M.; Renzo, F. D.; Espiau, P.; Fajula, F.; Nicolle, M.-A. *Stud. Surf. Sci. Catal.* 1991, 69, 127-134.
46. Müller, M.; Harvey, G.; Prins, R. *Microporous Mesoporous Mater.* 2000, 34 (3), 281-290.
47. Müller, M.; Harvey, G.; Prins, R. *Microporous Mesoporous Mater.* 2000, 34 (2), 135-147.

Chapter 5

Summary and Conclusion

At the onset of this work several questions remained unanswered.

- i) Can new insights on the formation zeolites be gained from the use of *in situ* characterization techniques
- ii) What is the reason why certain zeolite frameworks suffer from extensive degradation in the presence of hot liquid water?
- iii) Combining this knowledge, is it possible to design a robust zeolite suitable for the conversion of long-chain molecules in the aqueous phase

It is now attempted to summarize the findings reported in this thesis in order to answer these questions.

The presented work shows that the combination of several *in situ* techniques allows the accurate observation of the crystallization process in the FAU structure. This structure has been shown previously to be susceptible to the attack by hot liquid water leading to rapid amorphization when a high Si/Al material is used. In a first step, the aged gel undergoes a reorganization as it is heated to an adequate the synthesis temperature. During this induction period it was observed that the structural order, as assessed by ^{27}Al MAS NMR, relates to amorphous aluminosilicates. This amorphous gel, however, experiences a distortion of the Al-O bond during the induction period, seen by Al-XANES, inferring the continuous precipitation and dissolution of germ-nuclei prior to crystallization. After reaching a critical size of these nuclei, crystallization occurs which can be neatly followed by the decreasing line-width of the tetrahedral Al, in line with the increasing crystallinity as assessed *ex situ* by XRD. Investigating the Na environment in the forming zeolite framework with *in situ* ^{23}Na MAS NMR enabled us to differentiate between species present in the zeolite framework. Elucidating the formation rate from the spectra, we assigned the species to the forming sodalite-like structures and supercage structures. The slower formation rate of the latter, is in line with a previously proposed mechanism suggesting the necessary building of sodalite sub-units before obtaining the FAU structure. The combinatorial use of different *in situ* techniques allowed us to observe the speciation of the Na environment as it directs the zeolite growth that we followed closely. While we did not obtain any information on the apparent structural weakness of this framework in liquid phase, we can likely attribute it to the various ‘stabilization’ protocols employed to obtain high-silica FAU, such as steaming and acid leaching. This can generate a significant concentration of defects. As was hypothesized previously, the presence of Al is believed to protect the

surrounding Si tetrahedrons against hydrolysis in aqueous phase. These conclusions prompted us to investigate how the role of defects and later the role of Al and more precisely the Brønsted acid site/Hydronium ion influence the zeolite stability.

Therefore, a model system was designed containing a defect enriched environment, largely devoid of Al and Brønsted acid sites. This was achieved via the selective leaching of B from a synthesized BEA framework where it, prior to leaching, occupied tetrahedral sites instead of the classically used Al. The BEA similarly to the FAU structure experiences significant amorphization when exposed to hot liquid water and is a more promising candidate for the low temperature (< 200 °C) conversion of lignocellulosic derived feedstocks in the presence of water. The defect-rich BEA model system was then selectively titrated with a chloroalkylsilane which reinserts a Si atom into the vacant lattice sites. Testing the hydrothermal stability of these materials prior and after stabilization, unequivocally, establishes that defects have a detrimental effect and subsequent curing of defects allows for the almost quantitative retention of crystallinity and microporosity.

This was once more established for catalytically relevant BEA systems. These BEA zeolites had a range of Si/Al allowing us thus to investigate the hypothesized stabilizing effect of Al. They exhibited stronger retention of crystallinity and microporosity when the defect concentration was low, either via synthesis design (defect concentration increased with Si/Al) or via the post-synthetic modification described above. When tested under catalytic conditions in the presence of cyclohexanol (for cyclohexanol dehydration), however, these material presented an unexpected result. While in pure hot liquid water, the defect concentration determined the stability of the framework, the presence of alcohol appeared to counterintuitively suppress the defects influence with more defective but more siliceous samples exhibiting a longer lifetime and higher turnover number than their defect-poor Al-rich counterparts. This striking result was then found to correlate strongly with the concentration of intraporous water. It was shown that the Brønsted acid site binds significantly more water molecules than an internal defect site explaining the paradoxical results obtained; As the affinity for the non-polar alcohol increased with higher Si/Al ratio the concentration of water was reduced, resulting in a retardation of framework hydrolysis and subsequent lifetime enhancement. Under these circumstances, in the presence of a co-solvent, defects play only a marginal role becoming significant only when the Brønsted acid site

concentration is low. When the number of Brønsted sites is low, the contribution of intraporous water is primarily attributed to defect sites with the large concentration of defects facilitating framework hydrolysis. Here it is shown that synthesizing a low-defect material through fluoride anion synthesis route can yield an extremely robust microporous zeolite material.

These summarized findings now allow us to propose an overarching conclusion and pathway towards designing a robust zeolite capable of withstanding the harsh hydrothermal conditions present at the low-temperature conversion of oxygenates in the presence of liquid water.

Catalyst design

- i) Reducing the concentration of intraporous water – Synthesis of a low-defect materials with a reduced number of Brønsted acid sites
 - a. Alternatively, use of a co-solvent with a higher affinity for the zeolite framework of chosen composition
- ii) Reducing the concentration of defects – Generation of a low-defect material either via post-synthetic modification or by employing the fluoride synthesis route
 - a. Alternatively, use a denser zeolite framework such as MFI which at catalytically relevant Al concentrations is largely free of defects

Reaction engineering

- iii) Dissolution is largely affected by the solubility of SiO_2 in water – addition of non-catalytic silica additives to reduce the dissolution of the zeolite

CURRICULUM VITAE

Sebastian Prodingler was born on April 4th, 1989 in Starnberg, Germany. Growing up in Villach, Austria he later attended the International School of Penang (Uplands) in Penang, Malaysia completing his high-school education obtaining the International Baccalaureate before enrolling at the Technische Universität München as a Chemistry major in 2008. He obtained his B. Sc. In 2011 by completing his thesis work titled ‘*Synthesis of Methyl Mercaptan on Ni₂P and Co-K-Mo Catalysts Supported on SBA-15*’ advised by Prof. Dr. Johannes A. Lercher under supervision of Dr. Oliver Gutierrez at the Department of Chemistry, Technische Chemie II. In 2013 Sebastian completed his Master’s thesis, titled ‘*Synthesis of Novel CO₂ Adsorbents and Investigation of Borate Additives for the Removal of CO₂ from Flue gases*’ under supervision of Prof. Dr. Bernhard Rieger at the Department of Chemistry, Wacker Lehrstuhl für Makromolekulare Chemie. Starting from May 2014, Sebastian was enrolled as a Ph.D. student in the group of Prof. Dr. Johannes A. Lercher at the Technische Universität München and employed at the Pacific Northwest National Laboratory performing the experimental work for this Ph.D. thesis. During his time at the Pacific Northwest National Laboratory, where he was mentored by Prof. Dr. Mirosław A. Derewinski his research interest has encompassed a variety of fields from CO₂ adsorption on microporous materials to novel catalysts for exhaust gas treatments and the work on zeolite formation mechanisms and their degradation behavior presented in the submitted thesis. This broad interest is also reflected by his publication record and number of presentations at several national and international meetings.

PUBLICATIONS

- 1) **Prodinge**, S., Derewinski, M. A., Vjunov, A., Burton, S. D., Arslan, I., & Lercher, J. A. (2016). Improving Stability of Zeolites in Aqueous Phase via Selective Removal of Structural Defects. *Journal of the American Chemical Society*, 138(13), 4408-4415.
- 2) **Prodinge**, S., Vemuri, R. S., Varga, T., McGrail, B. P., Motkuri, R. K., & Derewinski, M. A. (2016). Impact of chabazite SSZ-13 textural properties and chemical composition on CO₂ adsorption applications. *New Journal of Chemistry*, 40(5), 4375-4385.
- 3) Devaraj, A., Murugesan, V., Bao, J., Guo, M., Derewinski, A. M., Xu, Z., Gray, M., **Prodinge**, S., & Ramasamy, K. (2016). Discerning the Location and Nature of Coke Deposition from Surface to Bulk of Spent Zeolite Catalysts. *Scientific Reports*, 6, 37586.
- 4) **Prodinge**, S., Derewinski, M. A., Wang, Y., Washton, N. M., Walter, E. D., Szanyi, J., Gao, F., Wang, Y., & Peden, C. H. F. (2017). Sub-micron Cu/SSZ-13: synthesis and application as selective catalytic reduction (SCR) catalysts. *Applied Catalysis B: Environmental* 201, 461-469.
- 5) **Prodinge**, S., Vjunov, A., Fulton, J. L., Hu, J. Z., Camaioni, D. M., Derewinski, M. A., & Lercher, J. A. (2017). Formation of Faujasite Followed by in situ Spectroscopy. *Ready for submission*
- 6) **Prodinge**, S., Shi, H., Eckstein, S., Hu, J. Z., Camaioni, D. M., Olarte M. V. Derewinski, M. A., & Lercher, J. A. (2017). Stability of Zeolites in Aqueous Phase Reactions, *Chem. Mater.*, *submitted*.
- 7) Egbert, J. D., **Prodinge** S. & Weber R. S. (2017). Counting Surface Redox Sites in Carbon-supported Electrocatalyst by Cathodic Stripping of O deposited by N₂O, *in preparation*.

CONFERENCE PRESENTATIONS

- 1) ***Towards Understanding and Improving the Stability of Zeolites in Aqueous Phase Reactions*** abstract & poster, Nanoporous Materials & Their Applications, Gordon Research Conference & Seminar, August **2017**, Andover, NH
- 2) ***Principles of Designing Robust Zeolites for Condensed Phase Reactions*** abstract & oral presentation, 25th North American Catalysis Society Meeting, June **2017**, Denver, CO
- 3) ***Microporous Materials for the Effective Adsorption and Separation of CO₂ from Flue gases*** abstract & oral presentation, 253rd American Chemical Society National Meeting, April **2017**, San Francisco, CA
- 4) ***“Robust zeolites for application in ligno-cellulosic conversion reaction“*** abstract & oral presentation, 18th IZC meeting, June **2016**, Rio de Janeiro, Brazil
- 5) ***Improving the CO₂ Adsorption Behavior of SSZ-13 Zeolite by Modifying Chemical Composition and Particle Size*** abstract & poster, 18th IZC meeting, June **2016**, Rio de Janeiro, Brazil
- 6) ***Crystallization of FAU zeolite monitored with in-situ techniques (MAS-NMR and XAFS)*** abstract & poster, 18th IZC meeting, June **2016**, Rio de Janeiro, Brazil
- 7) ***Improving stability of zeolites in aqueous phase via selective structural defect removal*** abstract & oral presentation, 251st American Chemical Society National Meeting, March **2016**, San Diego, CA
- 8) ***Improving stability of zeolites in aqueous phase via selective structural defect removal*** talk, part of the physical science division seminar series, December **2015**, Richland, WA
- 9) ***Improving stability of zeolites in aqueous phase via selective structural defect removal*** abstract & poster, Pacific Northwest Chapter annual meeting of the American Vacuum Society, November **2015**, Mt. Hood, OR
- 10) ***Improving stability of zeolites in aqueous phase via selective structural defect removal*** abstract & poster, Pacific Coast Catalysis Society annual meeting, September **2015**, Richland, WA
- 11) ***Improving stability of zeolites in aqueous phase via selective structural defect removal*** abstract & poster, Suncat Summer Institute, August **2015**, Palo Alto, CA